AN ANALYSIS OF ARCTIC SEA ICE-ATMOSPHERE INTERACTION

by

Jessica M. Liptak

A dissertation submitted to the faculty of
The University of Utah
in partial fulfillment of the requirements for the degree of

Doctor of Philosophy

Department of Atmospheric Sciences

The University of Utah

August 2014

Copyright © Jessica M. Liptak 2014

All Rights Reserved

The University of Utah Graduate School

STATEMENT OF DISSERTATION APPROVAL

The dissertation of **Jessica M. Liptak**

has been approved by the following supervisory committee members:

Courtenay Strong	, Chair	**4/28/2014** Date Approved
Kenneth Golden	, Member	**4/28/2014** Date Approved
John Horel	, Member	**4/28/2014** Date Approved
Zhaoxia Pu	, Member	**4/28/2014** Date Approved
Thomas Reichler	, Member	**4/28/2014** Date Approved

and by **Kevin Perry** , Chair/Dean of

the Department/College/School of **Atmospheric Sciences**

and by David B. Kieda, Dean of The Graduate School.

ABSTRACT

Arctic sea ice is a key component of the climate system, acting as a reflective barrier between the ocean and the atmosphere. The decrease in sea ice over the observational record is associated with several feedback processes, such as the ice-albedo feedback. Here, general sea ice-atmosphere feedback (SAF) is defined in which a sea ice anomaly causes surface and atmospheric responses that either enhance the initial anomaly (positive feedback) or oppose the initial anomaly (negative feedback).

Chapters 2 and 3 examine the local SAF over the Barents Sea in an uncoupled modeling framework. Results indicate that the SAF is positive and dominated by the thermodynamic component of the feedback, where anomalously high sea ice cover over the Barents sea favors additional ice growth because it decreases upward surface turbulent heat fluxes, leading to atmospheric cooling and reduced downwelling longwave radiation flux at the surface, while the opposite scenario occurs for anomalously low sea ice cover.

Chapter 4 studies the effect of suppressing the SAF in a coupled model by exposing the atmosphere over the Barents Sea to surface turbulent heat fluxes, longwave heat fluxes, and surface temperatures weighted by climatological sea ice cover. Variability in sea ice, atmospheric temperature, and sea surface temperature

decrease in response to SAF suppression, indicating that the coupled feedback over the Barents Sea is positive.

While thermodynamic processes play a large role in regional sea ice-atmosphere interactions, wind-driven sea ice transport controls the overall Arctic ice mass on annual-and-shorter time scales. Most sea ice is exported from the Arctic through the Fram Strait, and changes in sea ice export are linked to hemispheric-scale atmospheric variability. In Chapter 5, the leading propagating patterns of variability associated with Fram Strait sea ice flux (F) are determined by applying Hilbert empirical orthogonal function analysis to reanalysis data. The leading two surface wind patterns are correlated with F when cyclonic and anticyclonic circulation features are positioned downstream and upstream of the Fram Strait, enhancing the northerly component of the flow through the Strait.

TABLE OF CONTENTS

CHAPTER 1

INTRODUCTION

1.1 Motivation

Arctic sea ice plays a key role in Earth's energy balance because it reflects a large portion of incoming solar radiation and affects the heat exchange between the ocean and the atmosphere. Satellite observations have shown decreasing trends in Arctic sea ice extent (Parkinson and Cavalieri 2008; Stroeve et al. 2012) and thickness (Lindsay and Zhang 2005; Kwok et al. 2009). The age of the remaining ice pack has also declined, and the oldest ice cover is limited to the region north of Greenland and the Canadian Archipelago (Maslanik et al. 2007).

Sea ice loss has been attributed to many feedback mechanisms (Serreze et al. 2007), including the oft-cited ice-albedo feedback (e.g., Curry et al. 1995; Winton 2006; Perovich et al. 2007), where reduced summer sea ice cover leads to increased solar radiation, ocean warming, and less ice cover the following winter. Changing ice cover also affects the regional atmospheric variability (Maslanik et al. 2007) and hemispheric-scale teleconnections such as the North Atlantic Oscillation (NAO) (e.g., Deser et al. 2000; Ukita et al. 2007; Parkinson and Cavalieri 2008) that feed back

dynamically on the sea ice through surface wind stress anomalies. Enhanced cyclonic circulation (Rigor et al. 2002) and increased flow through the Fram Strait (e.g., Vinje 2001; Smedsrud et al. 2011) have further contributed to reduced Arctic ice volume.

Figure 1.1 summarizes the interactions among sea ice anomalies (S), surface turbulent heat and longwave fluxes (Q), surface wind stress forcing (τ), and air temperature (T) that comprise a general sea-ice atmosphere feedback. S alters the exchanges of sensible, latent, and longwave heat between the surface and atmosphere (S $\rightarrow$ Q). When sea ice is removed, upward latent and sensible heat fluxes from the exposed ocean surface warm the overlying atmosphere and cause a localized decrease in surface pressure, leading to convergence, while an increase in sea ice cover causes a localized surface pressure increase and divergence as downward fluxes of sensible and latent heat and longwave radiation cool the lower atmosphere (Q $\rightarrow$ T,τ). The atmosphere, in turn, feeds back onto the sea ice via air temperature anomalies that impact thermodynamic ice growth and wind stress anomalies that further enhance or reduce ice convergence (T,τ $\rightarrow$ S).

This dissertation consists of three published papers and one manuscript that will be submitted for publication that answer the following questions regarding the dynamic and thermodynamic forcing of the Arctic sea ice-atmosphere feedback:

1. How does the atmosphere respond to positive and negative sea ice concentration anomalies over the Barents Sea?

   Chapter 2 (Liptak and Strong 2014b) examines the atmospheric responses to daily winter sea ice concentration anomalies over the Barents Sea by boundary forcing the standalone Community Atmosphere Model (CAM) with anomalies that are exclusively positive or negative, follow observed magnitudes, and decay realistically over time.

2. How do the atmospheric conditions produced by positive and negative SIC anomalies feed back onto the sea ice over the Barents Sea?

   Chapter 3 (Liptak and Strong 2014a) determines the feedback of the atmosphere onto the sea ice over Barents Sea using output from the CAM experiments in Chapter 2 to boundary force the atmosphere in the standalone Community Ice CoDE (CICE) model.

3. What is the behavior of the sea ice-atmosphere feedback in a coupled modeling framework, and how does suppressing this feedback affect sea ice variability over the Barents Sea?

   Chapter 4 studies the effects of shutting off the sea ice-atmosphere feedback in a coupled modeling framework by calculating values of the surface turbulent heat and longwave fluxes and temperature that assume an anomaly-free distribution of sea ice (i.e., Q $\rightarrow$ T,τ in Fig. 1.1 is effectively eliminated). This chapter is a manuscript in preparation for peer review.

4. What are the leading propagating patterns of variability in the surface wind over the Arctic, and how do they impact Fram Strait sea ice flux?

   Chapter 5 (Liptak and Strong 2013) identifies the leading propagating patterns of variability in the surface wind field over the Arctic using phase-shifted complex Hilbert empirical orthogonal functions (HEOFs) and examines the relationship between each pattern and Fram Strait sea ice flux.

1.2 Model Description

The experiments in Chapters 2–4 are run using version 4 of the CAM and CICE model, which are the atmosphere and sea ice components of the NCAR Community Earth System Model [CESM, previously called the Community Climate System Model (CCSM)].

1.2.1 CAM

The CAM has 26 vertical levels and solves 3-dimensional fundamental dynamics equations using finite-volume discretization. Following Neale et al. (2010), the atmosphere assumes hydrostatic balance

$$\frac{\partial p}{\partial z} = -\rho g, \tag{1.1}$$

where p is atmospheric pressure, z is height, ρ is density, and g is the gravitational constant. Air, moisture, and other tracers are conserved according to

$$\frac{\partial(X)}{\partial t} = -\nabla \cdot (\mathbf{V}X), \tag{1.2}$$

where X is the mass quantity of a variable, $\mathbf{V}$ is the vector $(u, v, \frac{d\varsigma}{dt})$, t is time, and ς denotes a general vertical coordinate.

Substituting potential temperature θ and the density parameter $\gamma = \frac{\partial p}{\partial \varsigma}$ for X in Eq. 1.2 yields

$$\frac{\partial(\gamma\theta)}{\partial t} = -\nabla \cdot (\mathbf{V}\gamma\theta), \tag{1.3}$$

or conservation of energy.

Additional details on atmospheric dynamics and the parametrization of moist precipitation processes, clouds, radiation, surface turbulent fluxes are provided by Neale et al. (2010).

1.2.2 CICE

The fundamental equations that drive the CICE model are described by Hunke and Lipscomb (2008) and are summarized as follows. The net change in sea ice thickness is described by

$$\frac{\partial g}{\partial t} = -\nabla \cdot (g\mathbf{u}) - \frac{\partial}{\partial h}(fg) + \psi, \tag{1.4}$$

where h is the ice thickness, g is the ice thickness distribution function $g(\mathbf{x}, h, t)dh$ for the thickness range $(h, h + dh)$, $\mathbf{u}$ is the horizontal ice velocity, and f is the thermodynamic ice growth rate. The first term on the right-hand side of Eq. 1.4 is the dynamical change in sea ice due to horizontal transport, the second term indicates the change in sea ice from processes that contribute to melting and freezing, and the final term ψ is the ridging distribution function.

Transport of ice and snow energy, volume, ice area, and other tracers behaves according to the continuity equation

$$\frac{\partial(X)}{\partial t} = -\nabla \cdot (X\mathbf{u}), \tag{1.5}$$

where X is a conserved quantity.

The change in sea ice due to melting and freezing is determined by setting the first and last terms on the right-hand side of Eq. 1.4 to 0 so that

$$\frac{\partial g}{\partial t} = -\frac{\partial}{\partial h}(fg). \tag{1.6}$$

CICE is run with 5 discrete ice thickness categories. Defining a_n^t as the sea ice area and h_n^t as the sea ice thickness for thickness category n at time t, the thermodynamic growth rate for a given ice thickness category over $\Delta t = [t, t+1]$ is

$$f_n = -\frac{h_n^{t+1} - h_n^t}{\Delta t}. \tag{1.7}$$

$g(h)$ encompasses the total ice area a_n at time $t+1$ defined as

$$a_n = -\int_{H_L}^{H_R} g dh, \tag{1.8}$$

and total ice volume v_n

$$v_n = -\int_{H_L}^{H_R} hg dh, \tag{1.9}$$

where H_L and H_R are the lower and upper boundaries of an ice category.

ψ in Eq. 1.4 represents mechanical changes in ice thickness distribution due to convergence and divergence. The thickness distribution is defined as

$$a_P(h) = b(h)g(h). \tag{1.10}$$

$b(h)$ is a weighting function:

$$b(h) = \frac{exp[-G(h)/a^*]}{a * [1 - exp(-1/a^*)]}, \tag{1.11}$$

where $G(h)$ is the fraction of the ice area with ice thinner than h, and a^* is the average value of G.

CICE uses elastic-viscous-plastic sea ice dynamics described in Hunke and Dukowicz (1997). The 2-dimensional momentum equation provides the force balance for the mass of ice and snow (m) per unit area:

$$m\frac{\partial \mathbf{u}}{\partial t} = \nabla \cdot \sigma + \overrightarrow{\tau_a} + \overrightarrow{\tau_w} - \hat{k} \times mf\mathbf{u} - mg\nabla H_\circ, \tag{1.12}$$

where $\nabla \cdot \sigma$ is the force from internal ice stress, $\overrightarrow{\tau_a}$ is the wind stress force, $\overrightarrow{\tau_w}$ is the ocean stress force, $\hat{k} \times mf\mathbf{u}$ is the Coriolis force, and $mg\nabla H_\circ$ is the force due to the sea surface slope.

Thermodynamic growth/melt at the top of the sea ice is driven by the net radiation flux (F_0) between the sea ice surface and the atmosphere:

$$F_0 = F_{sens} + F_{lat} + F_{LWnet} + (1 - \alpha)(1 - i_0)F_{SW\downarrow}, \tag{1.13}$$

where F_{sens} is the sensible heat flux, F_{lat} is the latent heat flux, F_{LWnet} is the net longwave radiation flux (incoming − outgoing), $F_{SW\downarrow}$ is the downwelling shortwave

radiation flux, α is the sea ice albedo, and i_0 is the fraction of the absorbed shortwave flux that penetrates the ice.

The difference between F_0 and the conductive flux between the top and interior of the ice (F_{ct}) determines the enthalpy (q), or the change in heat at constant pressure, and thus melting/freezing at the top of the ice, which may be covered with snow, over time interval Δt according to

$$q\delta h = \begin{cases} (F_0 - F_{ct})\Delta t, & F_0 > F_{ct} \\ 0, & F_0 \leq F_{ct} \end{cases}, \tag{1.14}$$

where δh is the change in ice thickness, and T_{sf} is the surface temperature, which must be $\leq 0°$C.

For fresh snow or ice, q is defined as

$$q_s(T) = -\rho_s(-c_0 T + L_0), \tag{1.15}$$

where T is the ice/snow temperature, ρ_s is the ice/snow density, and c_0 and L_0 are the specific heat and latent heat of fusion of fresh ice/snow at 0°C, respectively. The specific heat of sea ice includes the effects of brine pockets:

$$c_i(T, S) = c_0 + \frac{L_0 \mu S}{T^2}, \tag{1.16}$$

where S is salinity and μ is the ratio of freezing temperature to salinity. Integrating

Eq. 1.16 and multiplying by ρ_i yields sea ice enthalpy in J/m^3:

$$q_i(T, S) = -\rho_i[-c_0(T_m - T) + L_0(1 - \frac{T_m}{T} - c_w T_m], \tag{1.17}$$

where T_m is the temperature of complete ice melt, and c_w is the specific heat of ocean water.

The net energy exchange between the bottom of the sea ice and the ocean surface is

$$F_{bot} = -\rho_w c_w c_h u_* (T_w - T_f), \tag{1.18}$$

where ρ_w is the density of seawater, c_h is a heat transfer coefficient, u_* is the friction velocity, T_w is the sea surface temperature, and T_f is the new ice temperature at time $t + 1$. Similarly to Eq. 1.14, the difference between the conductive flux at the bottom of the sea ice (F_{cb}) and F_{bot} determines the bottom melt/growth:

$$q\delta h = (F_0 - F_{cb})\Delta t. \tag{1.19}$$

Each ice thickness category has 4 ice/snow layers (k). Changes in the temperature of layer (T_k) are calculated as follows:

$$\rho_k c_k \frac{(T_k^{t+1} - T_k^t)}{\Delta t} = \frac{1}{\Delta h_k}[K_k^*(T_{k-1}^{t+1} - T_k^{t+1}) - K_{k+1}(T_k^{t+1} - T_{k+1}^{t+1})], \tag{1.20}$$

where the subscript of T indicates the layer, the superscript of T indicates the time step, ρ_k and c_k are the density and specific heat of the layer, respectively, K_k^* is the effective conductivity between layers $k+1$ and k, Δh is the layer thickness, and K_{k+1} is the effective conductivity at the top of layer $k+1$.

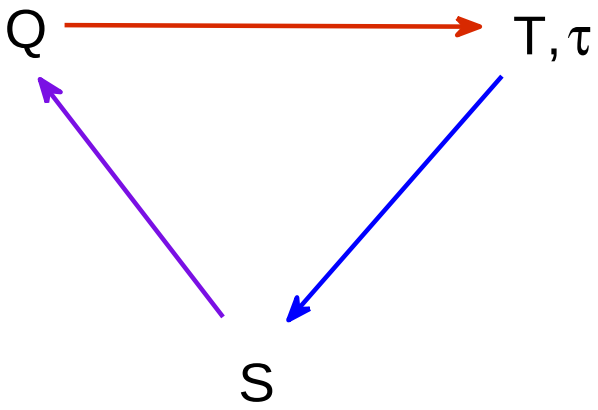

Fig. 1.1. Conceptual model of a sea ice-atmosphere feedback in which a sea ice anomaly (S) leads to vertical sensible, latent, and longwave heat fluxes (Q), resulting in near-surface air temperature (T) and wind stress (τ) anomalies. T and τ feed back onto S, producing a new sea ice configuration.

1.3 References

Curry, J. A., J. L. Schramm, and E. E. Ebert, 1995: Sea ice-albedo climate feedback mechanism. *J. Climate*, **8**, 240–247.

Deser, C., J. E. Walsh, and M. S. Timlin, 2000: Arctic sea ice variability in the context of recent atmospheric circulation trends. *J. Climate*, **13**, 617–633.

Hunke, E. C., and J. K. Dukowicz, 1997: An elastic-viscous-plastic model for sea ice dynamics. *J. Phys. Oceanogr.*, **27** (9), 1849–1867.

Hunke, E. C., and W. H. Lipscomb, 2008: CICE: The Los Alamos sea ice model user's manual, version 4. Tech. Rep. LA-CC-06-012, Los Alamos National Laboratory.

Kwok, R., G. F. Cunningham, M. Wensnahan, I. Rigor, H. J. Zwally, and D. Yi, 2009: Thinning and volume loss of the Arctic Ocean sea ice cover. *J. Geophys. Res*, **114**, doi:10.1029/2009JC005312.

Lindsay, R. W., and J. Zhang, 2005: The thinning of Arctic sea ice, 1988–2003: Have we passed a tipping point? *J. Climate*, **18**, 4879–4894, doi:10.1175/JCLI3587.1.

Liptak, J., and C. Strong, 2013: Propagating atmospheric patterns associated with sea ice motion through the Fram Strait. *J. Climate*, **26**, 2992–2997, doi:10.1175/JCLI-D-12-00599.1.

Liptak, J., and C. Strong, 2014a: A model-based decomposition of the sea ice-atmosphere feedback over the Barents Sea during winter. *J. Climate*, **27**, 2533–2544, doi:10.1175/JCLI-D-13-00371.1.

Liptak, J., and C. Strong, 2014b: The winter atmospheric response to sea ice anomalies in the Barents Sea. *J. Climate*, **27**, 914–924, doi:10.1175/JCLI-D-13-00186.1.

Maslanik, J., S. Drobot, C. Fowler, W. Emery, and R. Barry, 2007: A younger, thinner Arctic ice cover: Increased potential for rapid, extensive sea-ice loss. *Geophys. Res. Lett.*, **34**, doi:10.1029/2007GL032043.

Neale, R. B. et al., 2010: Description of the NCAR Community Atmosphere Model (CAM 4.0). Tech. Rep. NCAR/TN-485+STR, National Center For Atmospheric Research, Boulder, CO, USA.

Parkinson, C. L., and D. J. Cavalieri, 2008: Arctic sea ice variability and trends, 1979–2006. *J. Geophys. Res.*, **113**, C07 003, doi:10.1029/2007JC004558.

Perovich, D. K., B. Light, H. Eicken, K. F. Jones, K. Runciman, and S. V. Nghiem, 2007: Increasing solar heating of the Arctic Ocean and adjacent seas, 1979–2005:

Attribution and role in the ice-albedo feedback. *Geophys, Res. Lett.*, **34** (19), doi: 10.1029/2007GL031480.

Rigor, I. G., J. M. Wallace, and R. L. Colony, 2002: Response of sea ice to the Arctic Oscillation. *J. Climate*, **15**, 2648–2663, doi:10.1175/1520-0442(2002)015⟨2648: ROSITT⟩2.0.CO;2.

Serreze, M. C., M. M. Holland, and J. Stroeve, 2007: Perspectives on the Arctic's shrinking sea-ice cover. *Science*, **315**, 1533–1536.

Smedsrud, L. H., A. Sirevaag, K. Kloster, A. Sorteberg, and S. Sandven, 2011: Recent wind driven high sea ice export in the Fram Strait contributes to Arctic sea ice decline. *The Cryosphere Discuss.*, **5**, 1311–1334.

Stroeve, J. C., M. C. Serreze, M. M. Holland, J. E. Kay, J. Malanik, and A. P. Barrett, 2012: The Arctic's rapidly shrinking sea ice cover: A research synthesis. *Climatic Change*, **110** (3-4), 1005–1027, doi:10.1007/s10584-011-0101-1.

Ukita, J., M. Honda, H. Nakamura, Y. Tachibana, D. J. Cavlieri, C. L. Parkinson, H. Koide, and K. Yamamoto, 2007: Northern Hemisphere sea ice variability: Lag structure and its implications. *Tellus, Ser. A*, **59**, 261–272, doi:10.111/j.1600-0870. 2006.0223.x.

Vinje, T., 2001: Anomalies and trends in sea-ice extent and atmospheric circulation in the Nordic Seas during the period 1864–1998. *J. Climate*, **14**, 3503–3517.

Winton, M., 2006: Amplified Arctic climate change: What does surface albedo feedback have to do with it? *Geophys. Res. Lett.*, **33**, L03 701, doi:10.1029/ 2005GL025244.

CHAPTER 2

THE WINTER ATMOSPHERIC RESPONSE TO SEA ICE ANOMALIES IN THE BARENTS SEA[1]

2.1 Abstract

The atmospheric response to sea ice anomalies over the Barents Sea during winter was determined by boundary forcing the Community Atmosphere Model (CAM) with daily varying high and low sea ice concentration (SIC) anomalies that decreased realistically from December to February. The high- and low-SIC anomalies produced localized opposite-signed responses of surface turbulent heat flux and wind stress that decreased in magnitude and extent as winter progressed. Responses of sea level pressure (SLP) and 500-mb height evolved from localized, opposite-signed features into remarkably similar large-scale patterns resembling the negative phase of the North Atlantic Oscillation (NAO). Hilbert Empirical Orthogonal Functions (HEOF) analysis of the composite high-SIC and low-SIC SLP responses uncovered how they differed. The hemispheric pattern in the leading HEOF was similar for the high-

[1]Liptak, Jessica, Courtenay Strong, 2014: The Winter Atmospheric Response to Sea Ice Anomalies in the Barents Sea, *J. Climate*, **27**, 914–924, 10.1175/JCLI-D-13-00186.1.
©American Meteorological Society. Used with permission.

SIC and low-SIC responses, but the high-SIC response cycled through the pattern once per winter, whereas the low-SIC response cycled through the pattern twice per winter. The second HEOF differed markedly between the responses, with the high-SIC response featuring zonally oriented Atlantic and Pacific wave features, and the low-SIC response featuring a meridionally oriented Atlantic dipole pattern.

2.2 Introduction

Arctic sea ice cover impacts and responds to the local atmospheric features and large-scale variability associated with the Arctic Oscillation (AO; Thompson and Wallace 1998) and North Atlantic Oscillation (NAO; e.g., Hurrell et al. 2003). Changes in surface turbulent heat fluxes and wind stress forcing resulting from sea ice-atmosphere interaction produce immediate and long-term effects on the Arctic climate system that extend into subsequent seasons. Wu and Zhang (2010) showed that variability in the 500-mb height field over the Arctic was correlated with sea ice concentration at 0-to-2-month lags (atmosphere leads ice) during all seasons except winter, when atmospheric patterns were correlated with sea ice concentration at lags between -1 and -4 months (ice leads atmosphere). The leading winter maximum covariance analysis modes of 500-mb height and SIC depicted ice loss in the marginal seas and a pattern resembling the negative phase of the AO, with positive height anomalies over the North Pole and negative height anomalies over the ocean basins. In a modeling framework, sea ice extent and concentration anomalies derived from observed winters with anomalously high and low ice over the Arctic

produced atmospheric responses that resemble the NAO, though their magnitudes were weak relative to internal atmospheric variability (Alexander et al. 2004). The winter AO index is related to both winter sea ice motion and summer sea ice concentration (Rigor et al. 2002), where increased sea ice divergence and decreased ridging during the positive phase of wintertime AO contributes to thinning of Arctic sea ice during the following summer as a result of atmospheric warming from upward latent heat fluxes. In turn, increased upward latent heat fluxes resulting from anomalously low sea ice concentration over the Arctic in August and September decrease static stability, generating a barotropic atmospheric response and negative NAO-like pattern in winter (Jaiser et al. 2012). Reduced Arctic sea ice cover is also associated with decreased winter extratropical storm activity (Seierstad and Bader 2009), winter cold air outbreaks over the northern continents (Honda et al. 2009; Petoukhov and Semenov 2010; Yang and Christensen 2012), and enhanced snowfall over Europe, Eurasia and portions of the United States (Liu et al. 2012).

The remote influence of sea ice on atmospheric variability may be attributed to stationary Rossby waves generated by surface turbulent heat flux anomalies (Honda et al. 1999). Yamamoto et al. (2006) proposed that Rossby waves originating from the Nordic Seas and Sea of Okhotsk could serve as a dampening mechanism for the NAO that is manifested in a lagged relationship between the positive phase of the NAO and the "seesaw" pattern of anomalously low sea ice concentration over the Nordic Seas and Sea of Okhotsk and anomalously high sea ice concentration over the Labrador and Bering Seas throughout the winter. Ice removal over the Barents

Sea may induce stationary Rossby waves that strengthen the Siberian High, leading to cold air outbreaks over Europe and Eurasia during winter (Honda et al. 2009; Petoukhov and Semenov 2010).

Sea ice-atmosphere interaction is particularly strong in the Atlantic basin during the cold season due to the enhanced variability of the NAO and storm track. The leading pattern of variability in winter Arctic SIC depicts positive and negative ice concentration anomalies east and west of Greenland, respectively, in association with the negative phase of the NAO (Deser et al. 2000). Similarly, Vinje (2001) showed that the December–March NAO index was negatively correlated with April sea ice extent east of Greenland and positively correlated with April ice extent in the Labrador Sea. The relationship between the sea ice dipole pattern and the NAO suggests a negative feedback (Magnusdottir et al. 2004; Strong et al. 2009; Strong and Magnusdottir 2010) that is primarily driven by sea ice anomalies over the Barents Sea (Magnusdottir et al. 2004): anomalously low Barents Sea ice cover is characteristic of the positive NAO, but induces the negative phase of the NAO toward the end of winter. Deser et al. (2004) decomposed the total modeled winter atmospheric response to negative ice extent anomalies over the Barents Sea and positive anomalies over the Labrador Sea into a direct baroclinic response driven by diabatic heating and an indirect response defined by the projection onto the leading mode of variability in the control atmosphere resembling the AO/NAO. Results from a coupled modeling study by Koenigk et al. (2009) showed that anomalously high and low Barents Sea ice volume produced localized opposite-signed SLP and surface

turbulent heat flux responses corresponding to a direct response. In addition, high Barents Sea ice volume in spring and winter generated large-scale negative NAO-like features consistent with an indirect response.

It is clear from observations and model results that sea ice in the Barents Sea region drives a substantial portion of the atmospheric variability on local and hemispheric scales. However, many of the aforementioned modeling studies have implemented sea ice anomalies that are unrealistically large, remain constant over time, or have opposite signs in the same experiment. Alexander et al. (2004) showed that more realistic sea ice boundary forcing did not generate a significant atmospheric response, but their ice forcing patterns had regionally-varying signs. For example, at least 1 month in the high-SIC case contained negative ice anomalies over Barents Sea region (their Fig. 1).

Here, we investigate the atmospheric response to sea ice anomalies over the Barents Sea during winter that are 1) exclusively positive or negative, 2) follow observed magnitudes, and 3) decay realistically over time. Daily, rather than monthly, ice boundary forcing is used to include the effects of synoptic-scale variations in sea ice (Dammann et al. 2012). In addition, we use a statistical analysis method involving phase-shifted complex Hilbert empirical orthogonal functions (Strong and Liptak 2012) to detect propagating features in the response patterns.

2.3 Data and Methods

2.3.1 Model Description

The standalone Community Atmosphere Model (CAM; Neale et al. 2010) and the Community Ice CodE (CICE) with a slab ocean (Hunke and Lipscomb 2008) were used to produce continuous control runs and winter (December–February) experimental runs. The CAM and CICE are the atmosphere component and sea ice components of the Community Climate System Model/Community Earth System Model (CCSM/CESM; Gent et al. 2011). Version 4 of the CAM has 26 vertical levels and was run on a $1.9^\circ \times 2.5^\circ$ grid with a finite volume core (Lin 2004). Version 4 of CICE was run with 5 discrete ice thickness categories on a 1° displaced-pole grid with the pole centered over Greenland.

2.3.2 Experimental Design

Default monthly climatological sea ice and SSTs from the merged Hadley Centre sea ice and SST (HadISST1) dataset and version 2 of the NOAA weekly optimum interpolation (OI) SST data (Hurrell et al. 2008) were used to force a 100-year continuous CAM control run (A_{100}) initialized on 01 November. Output from A_{100} was used to produce a 100-year continuous CICE control run (I_{100}).

An index of daily area-weighted sea ice concentration (SIC) anomalies over the Barents Sea was derived from I_{100} output during winter (December–February) using the region spanning 70°–82°N and 20°–65°E (black box in Fig. 2.1). The index was defined as the area-weighted daily SIC anomalies relative to the climatological

winter SIC computed from the I_{100} ensemble mean. The winter containing the most days with index values more than 1 standard deviation (1σ) above the climatological winter mean was selected as sea ice boundary forcing for the high-SIC CAM experiment ($A_{\text{HIGH-SIC}}$, 55 days $> 1\sigma$). Likewise, the winter containing the most days with index values more than 1 standard deviation below the climatological winter mean was used to define the SIC boundary forcing for the low-SIC experiment ($A_{\text{LOW-SIC}}$, 50 days $< -1\sigma$). The SIC anomalies over the Barents Sea were then superimposed on the winter daily climatological SIC computed from the daily I_{100} ensemble mean, and these boundary forcing data sets were used to create $A_{\text{HIGH-SIC}}$ and $A_{\text{LOW-SIC}}$. The control run (A_{CLIM}) was forced with the daily winter climatological SIC so that the sea ice boundary forcing was identical at all grid points in $A_{\text{HIGH-SIC}}$, $A_{\text{LOW-SIC}}$, and A_{CLIM} except over the Barents Sea. Figure 2.1 shows the monthly mean values of the daily SIC anomalies for the $A_{\text{HIGH-SIC}}$ and $A_{\text{LOW-SIC}}$ experiments.

The $A_{\text{HIGH-SIC}}$, $A_{\text{LOW-SIC}}$, and A_{CLIM} sea ice boundary conditions were regridded to the $1.9^\circ \times 2.5^\circ$ CAM grid, and CAM was run for 100 winters initialized with 1 December conditions taken from each year of A_{100}. It should be noted that the atmosphere was not in equilibrium with the sea ice at the time of initialization. We averaged $A_{\text{HIGH-SIC}}$, $A_{\text{LOW-SIC}}$, and A_{CLIM} output across their respective ensemble members for each 6-hourly snapshot during winter and then defined the positive response by subtracting the A_{CLIM} ensemble mean from the $A_{\text{HIGH-SIC}}$ ensemble mean (denoted $A_{\text{HIGH-SIC}} - A_{\text{CLIM}}$ and referred to as the "high-SIC response") and likewise for the low-SIC response (denoted $A_{\text{LOW-SIC}} - A_{\text{CLIM}}$). The 6-hourly high-SIC

and low-SIC response patterns were reduced to daily means and monthly means for different analyses. Statistical significance at the 95% confidence level was determined by bootstrapping the distributions of each anomaly 1000 times using resampling with replacement (e.g., Efron 1979).

Our sea ice boundary forcing datasets contain energy at daily timescales absent in prior studies using monthly mean forcing, but may still underestimate the observed variability in SIC for the following reasons: the monthly mean SSTs and SIC prescribed in A_{100} may produce atmospheric boundary conditions that dampen SIC variability in I_{100}, and the SIC in I_{100} lacks the strong trends present in observations.

2.3.3 HEOF Analysis

To determine the propagating patterns that accounted for the most variability in the SLP responses, the leading two Hilbert empirical orthogonal functions (HEOFs; e.g., Hannachi et al. 2007) were calculated from the covariance matrix of the December–February daily ensemble mean fields of SLP weighted by the square root of the cosine of the latitude over the Northern Hemisphere from 20°N to 90°N for $A_{\text{HIGH-SIC}} - A_{\text{CLIM}}$ and $A_{\text{LOW-SIC}} - A_{\text{CLIM}}$. Briefly, the computation of HEOFs follows the procedure used for standard EOFs, with the additional step of applying a Hilbert transform to the covariance matrix to "complexify" the data prior to performing a singular value decomposition. The resultant HEOFs and corresponding principal component time series are complex with associated phase angles. HEOF1 and HEOF2 denote the first and second HEOF spatial patterns, and the associated

principal component time series were obtained by projecting the SLP data onto the HEOF coefficients. To clarify the relationship between the HEOFs and their temporal evolution in the two experiments, the phases of the HEOFs were shifted to maximize the correlation between the real parts of the HEOF time series of $A_{\text{HIGH-SIC}} - A_{\text{CLIM}}$ and $A_{\text{LOW-SIC}} - A_{\text{CLIM}}$. Since the phase angle is arbitrary, shifting the phase does not impact the fundamental pattern or explained variance of the HEOF. A detailed explanation of the computation and application of the HEOF phase shift may be found in Strong and Liptak (2012).

2.4 Results

2.4.1 Low-SIC Experiment

The low-SIC SLP response depicts a statistically significant localized negative anomaly over the Barents Sea during December (Fig. 2.2a). The response grows and switches sign, becoming a positive SLP anomaly over the pole in January (Fig. 2.2b), then evolves into large-scale features resembling the negative phase of the NAO in February (Fig. 2.2c) with positive anomalies over the Greenland and Barents Seas and negative SLP anomalies over the north Atlantic region. The positive 500-mb geopotential height anomaly over the Barents Sea in December (Fig. 2.2d) indicates that the response is initially baroclinic. In January and February, significant 500-mb height anomalies are generally collocated with SLP anomalies of the same sign away from the localized sea ice forcing (Fig. 2.2e, f). Statistically significant positive (upward) surface turbulent heat flux anomalies (Fig. 2.3a–c) and anomalous wind

stress convergence (Fig. 2.3d–f) are present over the Barents Sea in the vicinity of the ice anomaly (Fig. 2.1d–f), decreasing in magnitude and extent as the sea ice forcing weakens throughout the winter.

2.4.2 High-SIC Experiment

In December, the high-SIC SLP response shows localized positive anomalies over the Barents Sea (Fig. 2.4a). The response evolves into a dipole feature with a positive anomaly centered over northern Eurasia and a negative anomaly over the north Atlantic basin in January (Fig. 2.4b). In February, the negative NAO-like pattern is similar to the low-SIC response, but with the centers of action offset to the west (Fig. 2.4c). The 500-mb height response over the Barents Sea is not statistically significant in December (Fig. 2.4d), while the January response depicts a hemispheric wave-2-to-wave-3 pattern (Fig. 2.4e), and the February response resembles the negative phase of the NAO (Fig. 2.4f). Negative (downward) surface turbulent heat flux anomalies are present in all months (Fig. 2.5a–c) over the sea ice anomalies (Fig. 2.1a–c). The local wind stress response is strong in December (Fig. 2.5d) with divergence over the Barents Sea, then becomes dominated by broad larger scale circulation features in January and February (Fig. 2.5e, f).

2.4.3 Propagating Variability Associated with the SLP Responses

The large-scale indirect responses of the atmosphere to high-SIC and low-SIC forcing appear remarkably similar and negative NAO-like in February, and HEOF

analysis helps illuminate how they differ. HEOF1 of the high-SIC SLP response explains 43% of the variance, and its real part (Fig. 2.6a) shows a broad positive anomaly spanning the pole with centers over Scandinavia and the north coast of Eurasia and negative anomalies over the midlatitudes. By definition, the imaginary part of HEOF1 (Fig. 2.6e) depicts the pattern in the real part phase-shifted by $\pi/2$ and shows positive anomalies over Eurasia and southeast of Greenland and a strong negative anomaly over the Pacific basin. HEOF1 of the low-SIC response (Fig. 2.6b, f) explains 29% of the variance and is similar to the high-SIC response (Fig. 2.6a, e) with the centers of action displaced slightly equatorward. Incrementing the phases of the HEOFs (not shown) reveals a pattern resembling AO-like behavior in both responses (e.g., Fig. 2.6a, b) in which the signs and positions of the SLP anomalies oscillate between the polar and midlatitude regions.

During the first two weeks in December, the magnitudes, or moduli, of both HEOF1 time series (Fig. 2.7a) are small, reflecting the weakness of the early-winter response at the spatial scale of HEOF1. The moduli of the high-SIC (Fig. 2.7a, red line) and low-SIC (Fig. 2.7a, blue line) responses increase between late December and mid-February. The similar phase angles of HEOF1 of the high-SIC (Fig. 2.7c, red circles) and low-SIC (Fig. 2.7c, blue circles) responses in December and February indicate that the anomaly patterns that project onto the leading HEOFs (Fig. 2.6a, b, e, f) are nearly collocated, while divergence in the phase angles during January indicates that the anomaly patterns are offset from one another. Additionally, the phase of HEOF1 of the high-SIC response completes approximately one cycle (i.e.,

shifts from its initial phase by 2π over the course of the winter), while the phase of the low-SIC response completes two cycles.

The second HEOF (HEOF2) of the high-SIC SLP response accounts for 20% of the variance and depicts zonally oriented wave-2 and wave-3 patterns centered over the northern ocean basins (Fig. 2.6c, g). HEOF2 of the low-SIC SLP response (Fig. 2.6d,h) explains 13% of the variance and shows an NAO-like pattern over the north Atlantic basin and a zonal wave train over the Pacific basin. In both cases, the HEOFS are strongest over the area south of approximately 70°N, indicating that the orthogonality constraint may limit the ability of the second HEOFs to fully capture physically realistic wave features.

The differences in the moduli (Fig. 2.7b) and phases (Fig. 2.7d) of HEOF2 in January and early February indicate contrast in the temporal evolution of the associated high-SIC and low-SIC anomaly patterns. As in HEOF1, the sign of the SIC anomaly affects the rate of phase change. The phase of HEOF2 of the high-SIC response (Fig. 2.7d, red circles) completes approximately three cycles per winter, while the phase of HEOF2 of the low-SIC response completes two cycles (Fig. 2.7d, blue circles).

2.5 Summary and Conclusions

CAM was used to study the atmospheric response to daily high ($A_{\text{HIGH-SIC}}$) and low ($A_{\text{LOW-SIC}}$) sea ice concentration anomalies over the Barents Sea, and complex Hilbert empirical orthogonal function (HEOF) analysis was used to determine the

propagating patterns that accounted for the most variability in the SLP responses. In December and January, low-SIC conditions over the Barents Sea locally generated upward turbulent heat flux anomalies that lowered SLP and induced wind stress convergence, while the opposite scenario occurred for the high-SIC conditions. The signs and magnitudes of the local SLP and surface heat flux responses were consistent with the winter responses to high and low Barents Sea ice volume in Koenigk et al. (2009). The surface heat flux and wind stress responses in February were weaker due to the small extent and magnitude of the ice forcing. During February, the large-scale low-SIC SLP and 500-mb height responses resembled the negative phase of the NAO in agreement with the large-scale atmospheric responses to negative Barents Sea ice anomalies in Magnusdottir et al. (2004), Deser et al. (2007), Strong and Magnusdottir (2010), and Seierstad and Bader (2009). Notably, the high-SIC SLP responses in February were remarkably similar to the corresponding low-SIC responses.

The development of the SLP and 500-mb height responses throughout the winter followed that of the atmospheric responses to winter (December–April) monthly varying negative sea ice extent anomalies over the Barents Sea and positive extent anomalies over the Labrador Sea in Deser et al. (2007), beginning in December as localized baroclinic responses centered over the ice anomalies and transitioning into hemispheric patterns resembling the negative AO/NAO by February. The December responses were similar to what Deser et al. (2004) referred to as the direct response of the atmosphere to diabatic forcing, while the February responses were similar to the

indirect response (i.e., the AO/NAO). In our study, the generation of opposite-signed SLP responses by the high-SIC and low-SIC boundary forcing during December was consistent with the opposite-signed low-level direct responses to warm and cold SST anomalies southeast of Greenland in Deser et al. (2004). The high-SIC and low-SIC responses in February resembled the negative AO/NAO pattern present in the indirect response to negative SST and sea ice extent anomalies in Deser et al. (2004) and Deser et al. (2007).

HEOFs of ensemble mean high-SIC and low-SIC SLP responses indicated that the sign of the ice boundary forcing affected the spatiotemporal phase of propagating wave features, which is reflected in the displacement between the centers of action in the February high-SIC and low-SIC SLP and 500-mb height responses. The leading HEOF (HEOF1) of the SLP responses depicted variability associated with hemispheric waves resembling the AO. Transitions in the phases of the HEOF1 time series indicated shifts in the positions and signs of SLP anomalies over the pole and midlatitudes in both responses. HEOF1 of the high-SIC response completed one cycle during the winter, while HEOF1 of the low-SIC response completed two cycles. Determination of mechanisms by which changes in Barents Sea ice cover affect the phase of the large-scale circulation features is beyond the scope of this study. However, one possible explanation is that Barents Sea ice anomalies induce synoptic-scale wave energy flux anomalies that alter the progression and location of large-scale waves through shifts in the zonal wind as indicated by Sokolova et al. (2007). The overall similarity of the responses to opposite surface forcing motivates

more detailed study of the underlying nonlinear atmospheric dynamics as in Deser et al. (2007) and Strong and Magnusdottir (2010).

HEOF2 showed wave-2 and wave-3 patterns over the Atlantic and Pacific basins that propagated east-west in the high-SIC response and north-south in the low-SIC response. HEOF2 of the high-SIC response completed three cycles per winter and the phase of the low-SIC response completed two cycles; hence, the SLP anomaly pattern associated with HEOF2 cycled more quickly when ice was added to the Barents Sea than when ice was removed. However, possible effects of the orthogonality constraint on the physical interpretation of HEOF2 were noted.

The results here focus on the modification of the atmosphere by anomalous Barents Sea ice cover through changes in the surface turbulent heat fluxes. The atmosphere, in turn, influences the growth and retreat of sea ice via surface wind stress forcing and thermodynamic effects stemming in part from temperature advection. Research is underway to determine how the atmospheric responses to the Barents Sea ice anomalies feed back onto the sea ice by forcing the CICE model with atmospheric data and initial conditions derived from the high-SIC and low-SIC experiments analyzed here.

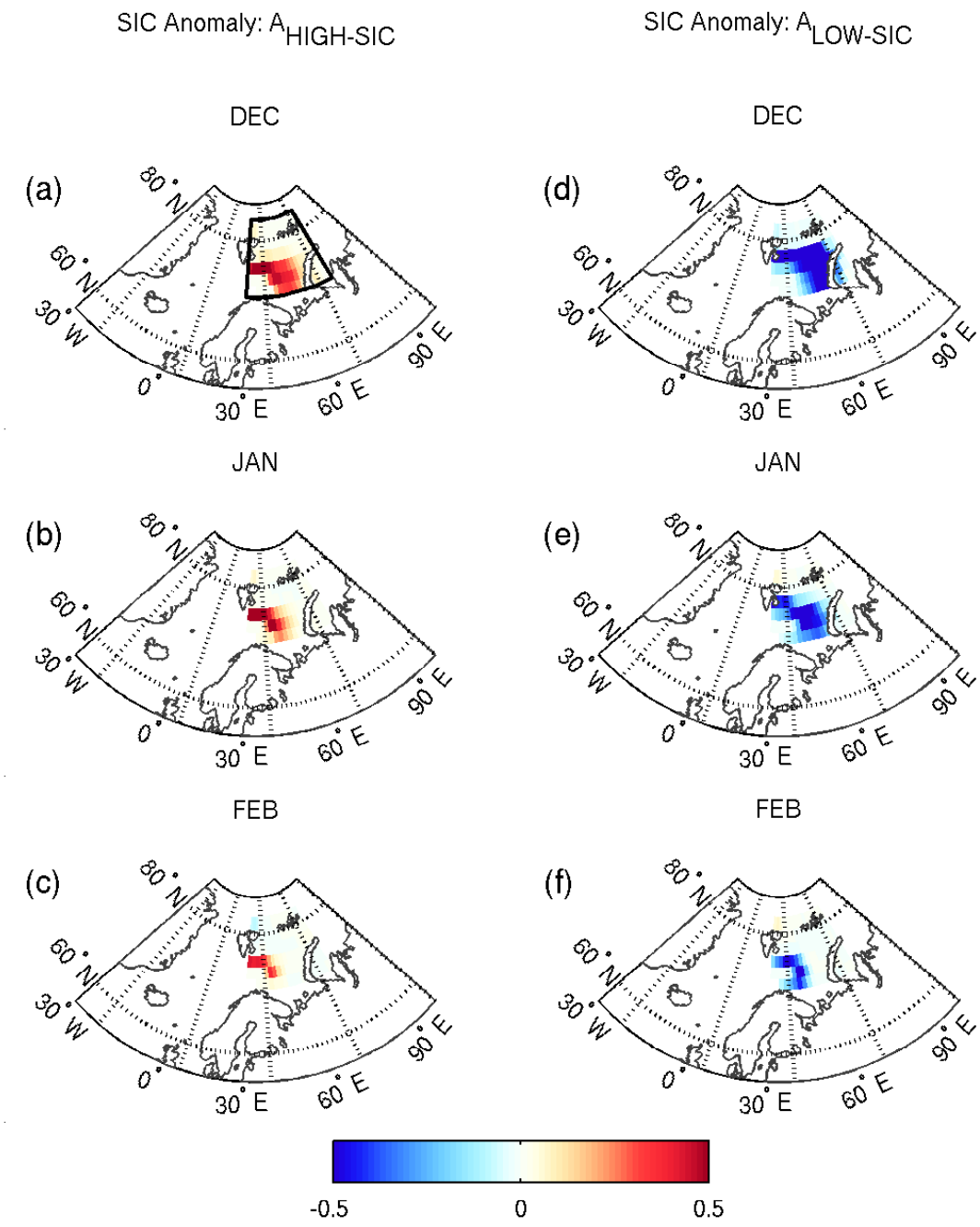

Fig. 2.1. Monthly means (December, January, and February) of the daily SIC anomalies used to force CAM in the (a)–(c) high-SIC and (d)–(f) low-SIC experiments. The black box in (a) outlines the area used to define the Barents Sea SIC index.

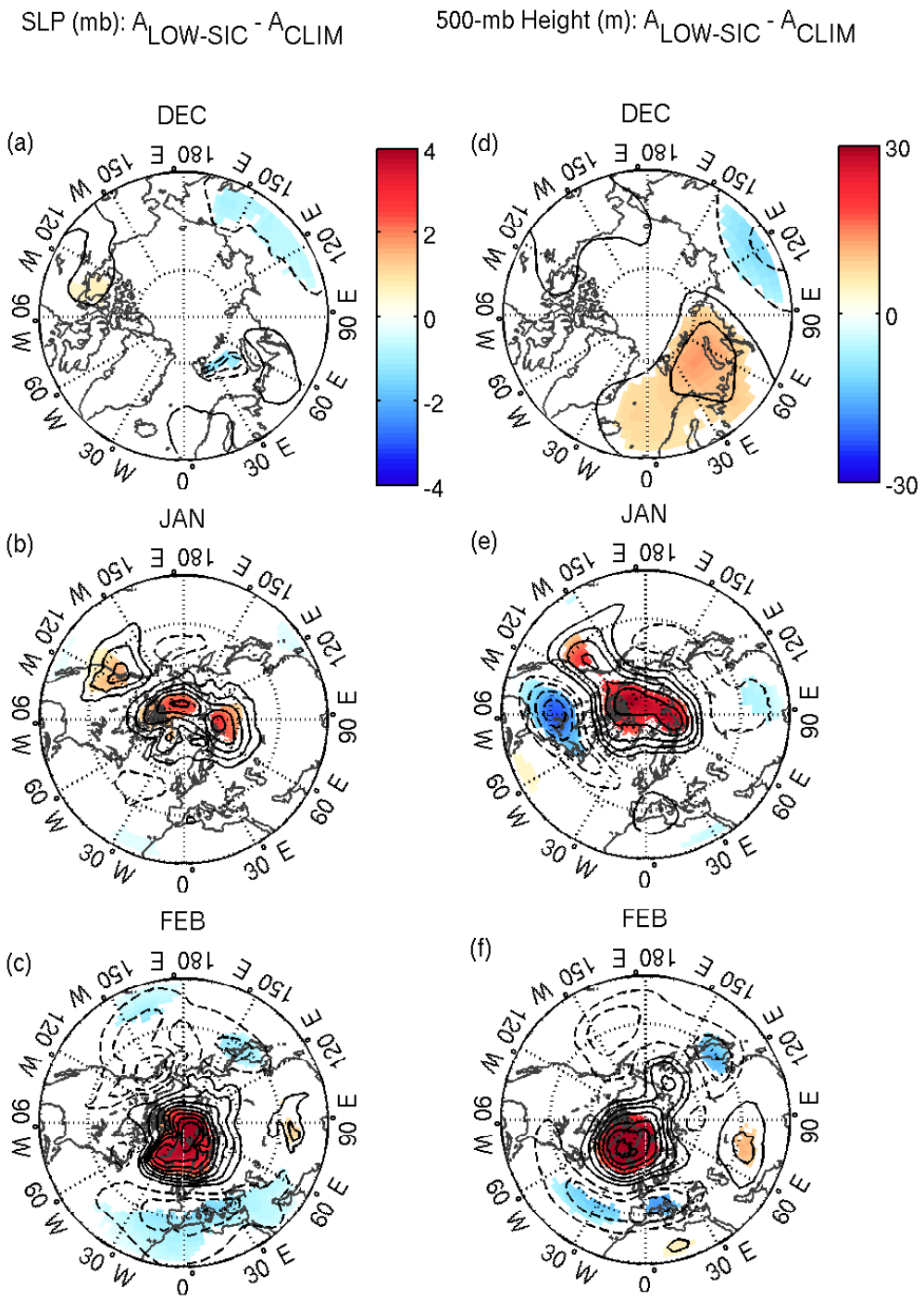

Fig. 2.2. December, January, and February monthly mean responses of (a)–(c) SLP (mb) and (d)–(f) 500-mb geopotential height (m) for the low-SIC experiment. Solid curves denote positive values and dashed curves denote negative values. The contour intervals are 0.5 mb for SLP and 5 m for 500-mb height and the zero contours are excluded. Positive and negative anomalies that are significant at the 95% confidence level are shaded.

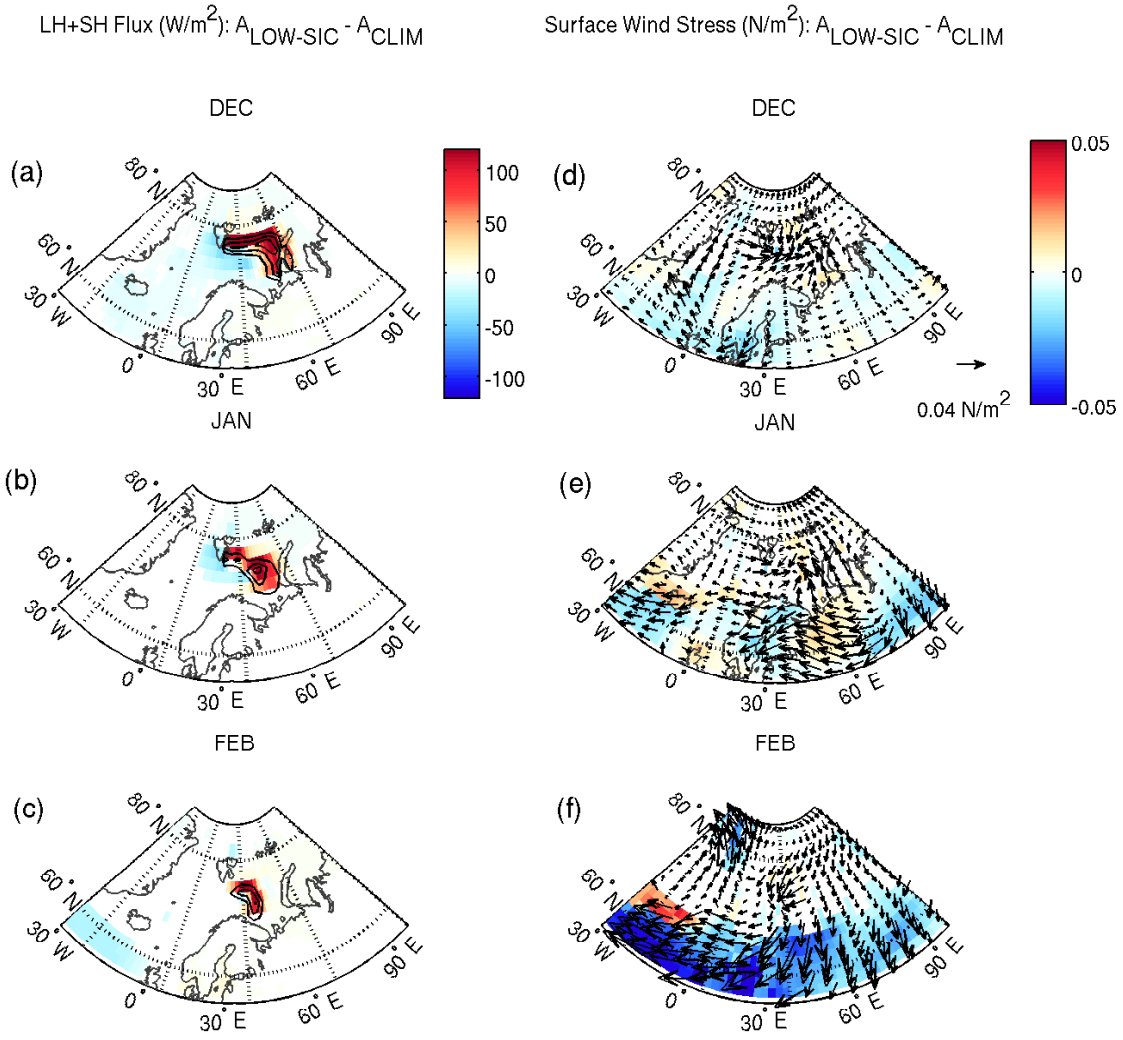

Fig. 2.3. December, January, and February monthly mean responses of (a)–(c) surface sensible and latent heat flux (W/m^2; positive upward) and (d)–(f) surface wind stress (N/m^2) for the low-SIC experiment. Solid curves denote positive values, and dashed curves denote negative values. The contour interval for the surface flux is 50 W/m^2, and the zero contour is excluded. Shading in (a)–(c) indicates total heat flux anomalies that are significant at the 95% confidence level, and shading in (d)–(f) indicates the magnitude of the wind stress anomaly where at least one of its components is significant at the 95% confidence level.

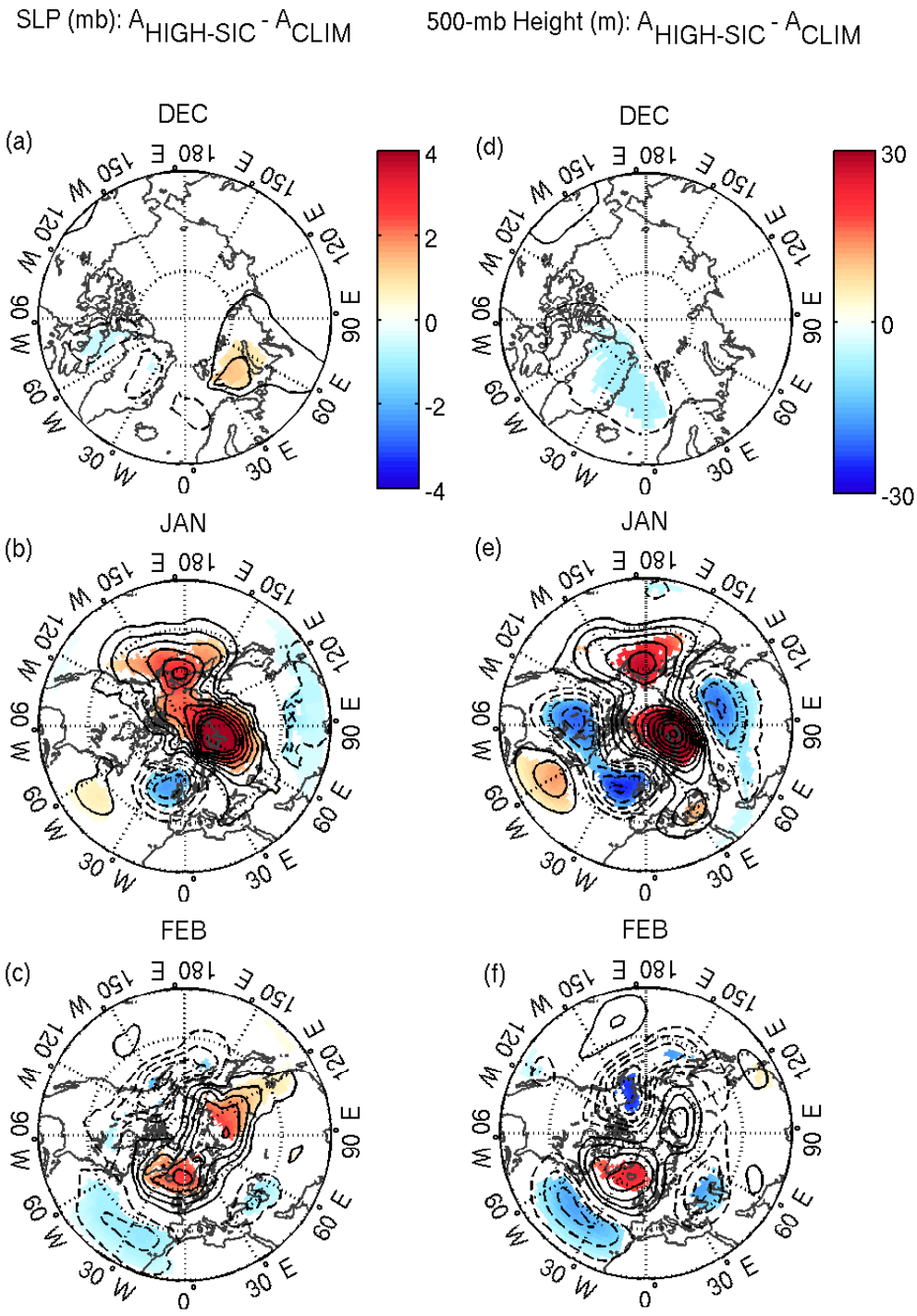

Fig. 2.4. As in Fig. 2.2 but for the high-SIC experiment.

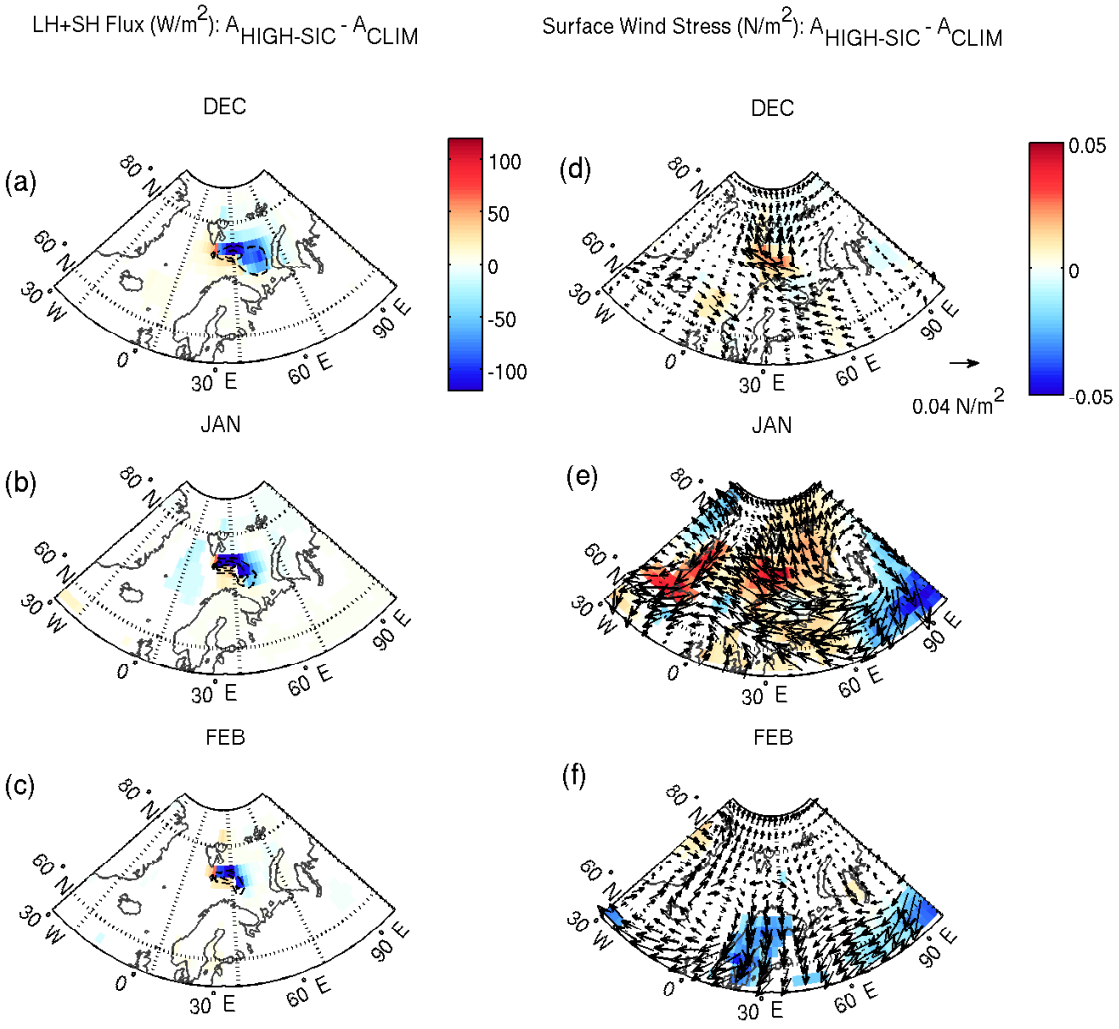

Fig. 2.5. As in Fig. 2.3 but for the high-SIC experiment.

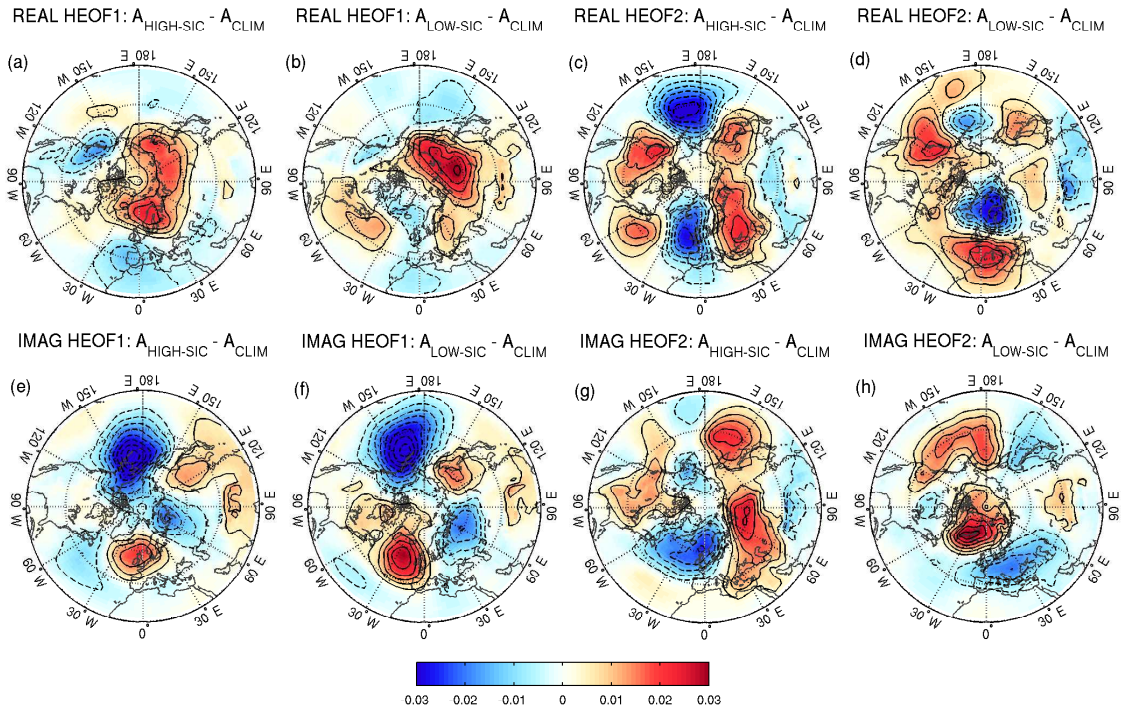

Fig. 2.6. The real part of HEOF1 of SLP for (a) $A_{\text{HIGH-SIC}} - A_{\text{CLIM}}$ and (b) $A_{\text{LOW-SIC}} - A_{\text{CLIM}}$. The real part of HEOF2 of SLP for (c) $A_{\text{HIGH-SIC}} - A_{\text{CLIM}}$ and (d) $A_{\text{LOW-SIC}} - A_{\text{CLIM}}$. The imaginary part of HEOF1 of SLP for (e) $A_{\text{HIGH-SIC}} - A_{\text{CLIM}}$ and (f) $A_{\text{LOW-SIC}} - A_{\text{CLIM}}$. The imaginary part of HEOF2 of SLP for (g) $A_{\text{HIGH-SIC}} - A_{\text{CLIM}}$ and (h) $A_{\text{LOW-SIC}} - A_{\text{CLIM}}$. Solid curves denote positive values, and dashed curves denote negative values. The contour interval is arbitrary, and the zero contour is excluded.

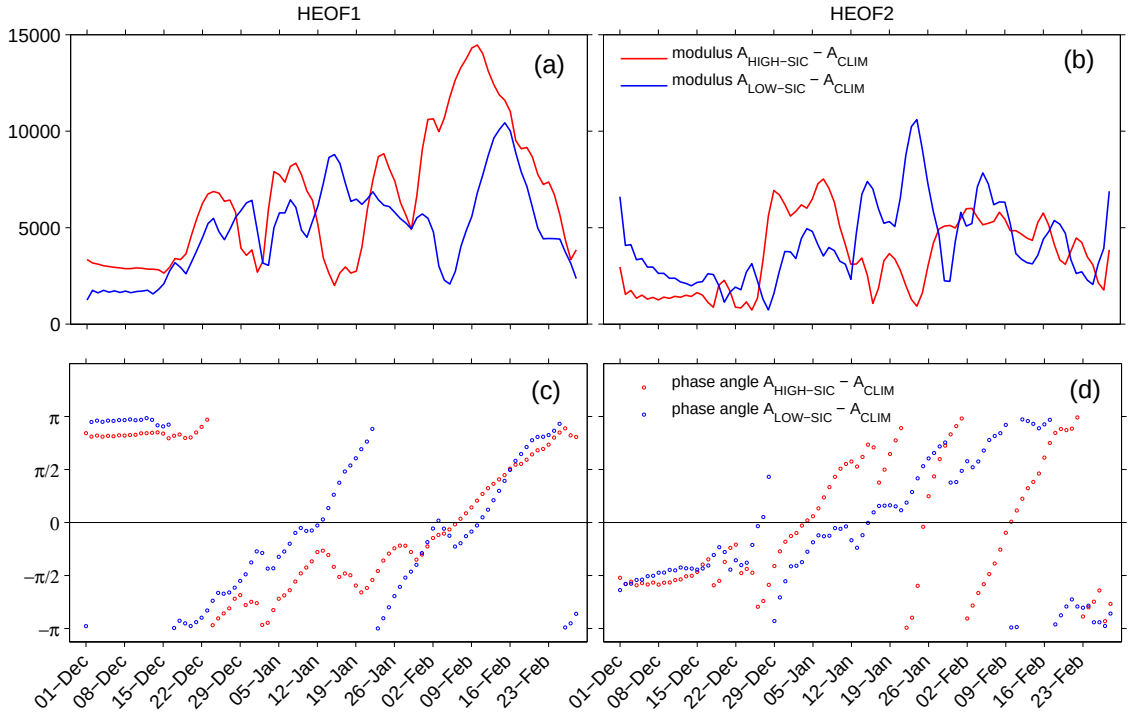

Fig. 2.7. The moduli and phases angles of the leading two principal component time series. Panels (a) and (b) show the moduli of $A_{\text{HIGH-SIC}} - A_{\text{CLIM}}$ (red lines) and $A_{\text{LOW-SIC}} - A_{\text{CLIM}}$ (blue lines) for HEOF1 and HEOF2, respectively. Panels (c) and (d) show the phase angles of $A_{\text{HIGH-SIC}} - A_{\text{CLIM}}$ (red circles) and $A_{\text{LOW-SIC}} - A_{\text{CLIM}}$ (blue circles) for HEOF1 and HEOF2.

2.6 References

Alexander, M. A., U. S. Bhatt, J. E. Walsh, M. S. Timlin, J. S. Miller, and J. D. Scott, 2004: The atmospheric response to realistic Arctic sea ice anomalies in an AGCM during winter. *J. Climate*, **17**, 890–905.

Dammann, D. O., U. S. Bhatt, P. L. Langen, J. R. Krieger, and X. Zhang, 2012: Impact of daily Arctic sea ice variability in CAM3.0 during fall and winter. *J. Climate*, doi:10.1175/JCLI-D-11-00710.1.

Deser, C., G. Magnusdottir, R. Saravanan, and A. S. Phillips, 2004: The effects of North Atlantic SST and sea-ice anomalies on the winter circulation in CCM3. Part II: Direct and indirect components of the response. *J. Climate*, **17**, 877–889, doi:10.1175/1520-0442(2004)017$⟨$0877:TEONAS$⟩$2.0.CO;2.

Deser, C., R. A. Tomas, and S. Peng, 2007: The transient atmospheric circulation response to North Atlantic SST and sea ice anomalies. *J. Climate*, **20**, 4751–4767.

Deser, C., J. E. Walsh, and M. S. Timlin, 2000: Arctic sea ice variability in the context of recent atmospheric circulation trends. *J. Climate*, **13**, 617–633.

Efron, B., 1979: Bootstrap methods: Another look at the jackknife. *Ann. Stat.*, **7**, 1–26.

Gent, P. R. et al., 2011: The Community Climate System Model version 4. *J. Climate*, **24**, 4973–4991, doi:10.1175/2011JCLI4083.1.

Hannachi, A., I. T. Jolliffe, and D. B. Stephenson, 2007: Empirical orthogonal functions and related techniques in atmospheric science: A review. *Int. J. Climatol.*, **27**, doi:10.1002/joc.1499.

Honda, M., J. Inoue, and S. Yamane, 2009: Influence of low arctic sea-ice minima on anomalously cold eurasian winters. *Geophys. Res. Lett.*, **36**, L08 707, doi:10.1029/2008GL037079.

Honda, M., K. Yamazaki, H. Nakamura, and K. Takeuchi, 1999: Dynamic and thermodynamic characteristics of atmospheric response to anomalous sea-ice extent in the Sea of Okhotsk. *J. Climate*, **12** (12), 3347–3358, doi:10.1175/1520-0442(1999)012$⟨$3347:DATCOA$⟩$2.0.CO;2.

Hunke, E. C., and W. H. Lipscomb, 2008: CICE: The Los Alamos sea ice model user's manual, version 4. Tech. Rep. LA-CC-06-012, Los Alamos National Laboratory.

Hurrell, J. W., J. J. Hack, D. Shea, J. M. Caron, and J. Rosinski, 2008: A new sea surface temperature and sea ice boundary dataset for the Community Atmosphere Model. *J. Climate*, **21** (19), 5145–5153, doi:10.1175/2008JCLI2292.1.

Hurrell, J. W., Y. Kushnir, G. Ottersen, and M. Visbeck, 2003: *The North Atlantic Oscillation: Climate Significance and Environmental Impact*. Amer. Geophys. Union, 27 pp.

Jaiser, R., K. Dethloff, D. Handorf, A. Rinke, and J. Cohen, 2012: Impact of sea ice cover changes on the Northern Hemisphere atmospheric winter circulation. *Tellus A*, **64**, doi:10.3402/tellusa.v64i0.11595.

Koenigk, T., U. Mikolajewicz, J. H. Jungclaus, and A. Kroll, 2009: Sea ice in the Barents Sea: Seasonal to interannual variability and climate feedbacks in a global coupled model. *Climate Dyn.*, **32**, 1119–1138.

Lin, S.-J., 2004: A "vertically Lagrangian" finite-volume dynamical core for global models. *Mon. Wea. Rev.*, **132**, 2293–2307, doi:10.1175/1520-0493(2004)132$⟨$2293:AVLFDC$⟩$2.0.CO;2.

Liu, J., J. A. Curry, H. Wang, M. Song, and R. M. Horton, 2012: Impact of declining Arctic sea ice on winter snowfall. *Proceedings of the National Academy of Sciences*, doi:10.1073/pnas.1114910109.

Magnusdottir, G., C. Deser, and R. Saravanan, 2004: The effects of North Atlantic SST and sea ice anomalies on the winter circulation in CCM3. Part I: Main features and storm track characteristics of the response. *J. Climate*, **17**, 857–876, doi:10.1175/1520-0442(2004)017$⟨$0857:TEONAS$⟩$2.0.CO;2.

Neale, R. B. et al., 2010: Description of the NCAR Community Atmosphere Model (CAM 4.0). Tech. Rep. NCAR/TN-485+STR, National Center For Atmospheric Research, Boulder, CO, USA.

Petoukhov, V., and V. A. Semenov, 2010: A link between reduced Barents-Kara sea ice and cold winter extremes over northern continents. *J. Geophys. Res.*, **115** (D21), D21 111, doi:10.1029/2009JD013568.

Rigor, I. G., J. M. Wallace, and R. L. Colony, 2002: Response of sea ice to the Arctic Oscillation. *J. Climate*, **15**, 2648–2663, doi:10.1175/1520-0442(2002)015⟨2648:ROSITT⟩2.0.CO;2.

Seierstad, I., and J. Bader, 2009: Impact of a projected future Arctic sea ice reduction on extratropical storminess and the NAO. *Climate Dyn.*, **33** (7), 937–943, doi:10.1007/s00382-008-0463-x.

Sokolova, E., K. Dethloff, A. Rinke, and A. Benkel, 2007: Planetary and synoptic scale adjustment of the Arctic atmosphere to sea ice cover changes. *Geophys. Res. Lett.*, **34** (17), L17 816, doi:10.1029/2007GL030218.

Strong, C., and J. Liptak, 2012: Propagating atmospheric patterns associated with winter Midwest precipitation. *J. Hydrometeorol.*, **13**, 1371–1382, doi:10.1175/JHM-D-11-0111.1.

Strong, C., and G. Magnusdottir, 2010: Dependence of NAO variability on coupling with sea ice. *Climate Dyn.*, **36**, 1681–1689, doi:10.1007/s00382-010-0752-z.

Strong, C., G. Magnusdottir, and H. Stern, 2009: Observed feedback between winter sea ice and the North Atlantic Oscillation. *J. Climate*, **22**, 6021–6032.

Thompson, D. W. J., and J. M. Wallace, 1998: The Arctic Oscillation signature in the wintertime geopotential height and temperature fields. *Geophys. Res. Lett.*, **25** (9), 1297–1300, doi:10.1029/98GL00950.

Vinje, T., 2001: Anomalies and trends in sea-ice extent and atmospheric circulation in the Nordic Seas during the period 1864–1998. *J. Climate*, **14**, 3503–3517.

Wu, Q., and X. Zhang, 2010: Observed forcing-feedback processes between Northern Hemisphere atmospheric circulation and Arctic sea ice coverage. *J. Geophys. Res.*, **115** (D14), D14 119.

Yamamoto, K., Y. Tachibana, M. Honda, and J. Ukita, 2006: Intra-seasonal relationship between the Northern Hemisphere sea ice variability and the North Atlantic Oscillation. *Geophys. Res. Lett.*, **33**, L14 711, doi:10.1029/2006GL026286.

Yang, S., and J. H. Christensen, 2012: Arctic sea ice reduction and European cold winters in CMIP5 climate change experiments. *Geophys. Res. Lett.*, **39** (20), doi:10.1029/2012GL053338.

CHAPTER 3

A MODEL-BASED DECOMPOSITION OF THE SEA ICE-ATMOSPHERE FEEDBACK OVER THE BARENTS SEA DURING WINTER[1]

3.1 Abstract

The feedback between Barents Sea ice and the winter atmosphere was studied in a modeling framework by decomposing it into two sequential boundary forcing experiments. The Community Ice CodE (CICE) model was initialized with anomalously high sea ice concentration (SIC) over the Barents Sea and forced with an atmosphere produced by positive SIC anomalies, and CICE was initialized with low Barents Sea SIC and forced with an atmosphere produced by negative SIC anomalies. Corresponding control runs were produced by exposing the same SIC initial conditions to climatological atmospheres, and the monthly mean sea ice response showed a positive feedback over the Barents Sea for both experiments: the atmosphere produced by positive SIC anomalies increased SIC over the Barents Sea during the winter, and

[1]Liptak, Jessica, Courtenay Strong, 2014: A Model-Based Decomposition of the Sea Ice-Atmosphere Feedback over the Barents Sea during Winter, *J. Climate*, **27**, 2533–2544, 10.1175/JCLI-D-13-00371.1. ©American Meteorological Society. Used with permission.

the atmosphere produced by negative SIC anomalies decreased SIC. These positive feedbacks were driven primarily by thermodynamic forcing from surface longwave flux anomalies and were weakened somewhat by atmospheric temperature advection. Dynamical effects also opposed the positive feedback, with enhanced surface wind stress divergence over the Barents Sea in the high-SIC case, and enhanced convergence in the low-SIC case.

3.2 Introduction

The interaction between Arctic sea ice and the atmosphere plays a large role in shaping local and hemispheric climate variability through changes in surface wind stress and turbulent heat fluxes. Physical reasoning suggests that negative sea ice anomalies locally induce upward sensible and latent heat flux anomalies, leading to decreased sea level pressure (SLP), cyclonic circulation, and surface convergence, while the opposite scenario occurs for positive sea ice anomalies. Sea ice, in turn, may respond to atmospheric variability associated with local flow regimes and large-scale teleconnection patterns.

On time scales shorter than one year, sea ice motion is primarily driven by surface wind stress (Thorndike and Colony 1982), where the direction of ice drift is approximately 30° to the right of the wind (Nansen 1902; Zubov 1943) and, as a general rule, parallel to surface isobars. Recent low September sea ice extent is associated with anticyclonic surface wind anomalies during the preceding summer (Ogi and Wallace 2007) that lead to enhanced poleward Ekman drift of the sea ice

(Ogi et al. 2008). The recent decrease in summer sea ice over the Western Arctic may also be attributed to anomalous anticyclonic flow, which is conducive to ice advection toward the Fram Strait (Ogi and Rigor 2013). Low-level pressure and wind anomalies that enhance southward flow through the Fram Strait are associated with increased sea ice export and explain a large fraction of the variability in Arctic sea ice cover (Ogi et al. 2010). Fram Strait sea ice export is correlated with the second EOF of Arctic SLP, referred to as the Dipole Anomaly (Wu et al. 2006; Wang et al. 2009) and similar patterns (Tsukernik et al. 2010) that depict an east-west pressure gradient over the Fram Strait. On a seasonal basis, the positive phase of the AO is associated with enhanced ice export through the Fram Strait and thinner ice over the eastern Arctic (Rigor et al. 2002; Zhang et al. 2003). Watanabe and Hasumi (2005) found that shifting the wind stress pattern from the negative phase of the AO to the positive phase increased Arctic sea ice export and decreased sea ice volume, while switching from the positive phase of the AO to the negative phase produced the opposite scenario. The positive phase of the North Atlantic Oscillation [NAO; Hurrell et al. (2003)] is also associated with enhanced Fram Strait sea ice flux in winter (e.g., Kwok and Rothrock 1999; Kwok et al. 2004), although the correlation is only statistically significant after 1977 due to the eastward shift in the NAO centers of action (Hilmer and Jung 2000).

The NAO also influences winter sea ice variability over the Labrador and Nordic seas, where positive sea ice anomalies over the Labrador Sea and negative sea ice anomalies over the Greenland and Barents Seas are associated with the positive phase

of the NAO (Deser et al. 2000; Vinje 2001). Several boundary forcing experiments with ice removal over the Barents Sea have also produced atmospheric patterns reminiscent of the NAO (Magnusdottir et al. 2004; Alexander et al. 2004; Seierstad and Bader 2009; Liptak and Strong 2014). Magnusdottir et al. (2004) showed that the feedback between North Atlantic ice cover and the NAO was negative; that is, the positive NAO reduces sea ice cover in the Barents Sea, which, in turn, is conducive to the negative NAO. In addition, decomposition of the sea ice forcing revealed that the NAO-like response primarily resulted from sea ice concentration anomalies over the Barents Sea. The negative feedback was subsequently detected via statistical analysis of observations (Strong et al. 2009) and hybrid statistical-dynamical modeling (Strong and Magnusdottir 2010). In contrast, Ou (2013) proposed that the large-scale sea ice atmosphere feedback over the Arctic was positive where, for example, negative SLP anomalies resulting from ice removal from the Barents Sea would strengthen the cyclonic circulation over the eastern Arctic, leading to further ice loss through the Fram Strait.

Prior studies focused on the response of the atmosphere to monthly sea ice anomalies (Alexander et al. 2004; Deser et al. 2004; Magnusdottir et al. 2004; Koenigk et al. 2009; Seierstad and Bader 2009) or the effects of large-scale atmospheric forcing on sea ice on interannual and longer time scales (Koenigk et al. 2009; Ogi et al. 2010; Zhang et al. 2010). Here, we examine the feedback of the atmosphere onto sea ice over the Barents Sea as it is the focal point of the large-scale sea ice-atmosphere feedback in the North Atlantic (Magnusdottir et al. 2004).

We focus on daily-to-monthly time scales during winter and decompose the feedback into two sequential boundary-forcing experiments: an atmosphere model perturbed by imposed sea ice anomalies (Liptak and Strong 2014) and a sea ice-slab ocean model responding to the perturbed atmospheric fields. Although decomposition of the feedback into two sequential boundary forcing experiments may alter aspects of the interactions present in a coupled framework (e.g., Chen et al. 2013), this decomposition allows us to fully control the sea ice conditions that initiate the anomalous atmosphere-ocean exchanges. Specifically, we use atmospheric fields that developed in response to anomalously high and low sea ice, where the sea ice anomalies were restricted to the Barents Sea, were of uniform sign, and decayed realistically over the winter.

3.3 Data and Methods

3.3.1 Model Description

Version 4 of the standalone CAM (Neale et al. 2010) and CICE with a slab ocean (Hunke and Lipscomb 2008) were used to produce continuous control runs and winter experimental runs. The CAM and CICE are the atmosphere component and sea ice component of the Community Climate System Model/Community Earth System Model (CCSM/CESM; Gent et al. 2011). The CAM has 26 vertical levels and was run on a $1.9^\circ \times 2.5^\circ$ grid with a finite volume core (Lin 2004). CICE was run using 5 discrete ice thickness categories on a 1° displaced-pole grid with the pole centered over Greenland. We use grid box-specific changes in sea ice concentration (SIC) due

to thermodynamics (ΔTHM) and due to dynamics (ΔDYN) as diagnostics, and these fields are available as output from CICE. ΔTHM is computed by aggregating the changes in SIC (fraction/day) that result from fluxes of radiation, sensible, and latent heat. ΔDYN is the total change in SIC from wind and sea surface stress-induced ice deformation, transport, and ridging.

3.3.2 Experimental Design

Table 3.1 summarizes nine simulations used in this study, and the associated notation, boundary conditions, and initial conditions for each are detailed in this section. Simulations denoted by I were CICE with a slab ocean and data atmosphere, and simulations denoted by A were CAM with data sea ice and sea surface temperatures (SSTs). A_{100} is a continuous 100-year control run forced with monthly climatological sea ice and SSTs from the merged Hadley Centre sea ice and SST (HadISST1) dataset and version 2 of the NOAA weekly optimum interpolation (OI) SST data (Hurrell et al. 2008). Output from A_{100} was used to produce a 100-year continuous CICE control run (I_{100}).

To develop boundary conditions for the CAM experiments, climatological sea ice boundary conditions (BC_{CLIM}) were calculated from the long-term means of the daily winter (December–February) SIC in I_{100}. Then, an index of daily area-weighted SIC anomalies averaged over the region spanning 70°–82°N and 20°–65°E (black box in Fig. 3.1a) was calculated for each winter in I_{100}. The winter containing the most days with index values more than 1 standard deviation (1σ) above the I_{100} long-term

winter mean was identified (55 days $> 1\sigma$), and the SIC from each winter day of the anomalous year was subtracted from corresponding daily values of the long-term winter mean to create anomalies. The SIC anomalies over the Barents Sea were superimposed onto $\mathrm{BC_{CLIM}}$, yielding high-SIC boundary conditions ($\mathrm{BC_{HIGH\text{-}SIC}}$); low-SIC boundary conditions ($\mathrm{BC_{LOW\text{-}SIC}}$) were prepared analogously from the winter containing the most days with index values more than 1σ below the $\mathrm{I_{100}}$ long-term winter mean (50 days $< -1\sigma$). The experiments $\mathrm{A_{HIGH\text{-}SIC}}$ and $\mathrm{A_{LOW\text{-}SIC}}$ were forced by $\mathrm{BC_{HIGH\text{-}SIC}}$ and $\mathrm{BC_{LOW\text{-}SIC}}$, respectively. The control run ($\mathrm{A_{CLIM}}$) was forced with $\mathrm{BC_{CLIM}}$ so that the daily sea ice boundary forcing was identical at all grid points in $\mathrm{A_{HIGH\text{-}SIC}}$, $\mathrm{A_{LOW\text{-}SIC}}$, and $\mathrm{A_{CLIM}}$ except over the Barents Sea. Figure 3.1 shows the monthly mean values of the daily SIC anomalies for the $\mathrm{A_{HIGH\text{-}SIC}}$ and $\mathrm{A_{LOW\text{-}SIC}}$ experiments. The $\mathrm{A_{HIGH\text{-}SIC}}$, $\mathrm{A_{LOW\text{-}SIC}}$, and $\mathrm{A_{CLIM}}$ sea ice boundary conditions were regridded to the $1.9^\circ \times 2.5^\circ$ CAM grid, and CAM was run for 100 winters initialized with 1 December conditions taken from each year of $\mathrm{A_{100}}$. In Section 3, we present atmospheric anomalies from $\mathrm{A_{HIGH\text{-}SIC}}$ and $\mathrm{A_{LOW\text{-}SIC}}$ that are of direct relevance to the sea ice responses investigated in this study, and additional details on larger-scale patterns in these atmospheric experiments are given in Liptak and Strong (2014).

To investigate how $\mathrm{A_{HIGH\text{-}SIC}}$ feeds back onto the sea ice, we forced CICE with $\mathrm{A_{HIGH\text{-}SIC}}$ using 1 December fields from $\mathrm{BC_{HIGH\text{-}SIC}}$ as initial conditions for the experiment $\mathrm{I_{HIGH\text{-}SIC}}$. The associated control run was the same, but forced by $\mathrm{A_{CLIM}}$, and is denoted $\mathrm{I_{CLIM\text{-}H}}$. Likewise, the feedback of $\mathrm{A_{LOW\text{-}SIC}}$ onto the sea ice was studied by forcing CICE with $\mathrm{A_{LOW\text{-}SIC}}$ for the experiment $\mathrm{I_{LOW\text{-}SIC}}$, and with $\mathrm{A_{CLIM}}$

for the corresponding control run $I_{CLIM\text{-}L}$ using 1 December fields from $BC_{LOW\text{-}SIC}$ as initial conditions.

The CAM and CICE experiments were each run for 100 winters, and their output was averaged over their respective ensemble members to form daily means. The responses of the CAM runs were defined as the anomalies produced by subtracting the ensemble mean A_{CLIM} atmospheric fields for each day of winter: $A_{HIGH\text{-}SIC} - A_{CLIM}$ and $A_{LOW\text{-}SIC} - A_{CLIM}$. For the CICE runs, the responses were analogously defined as $I_{HIGH\text{-}SIC} - I_{CLIM\text{-}H}$ and $I_{LOW\text{-}SIC} - I_{CLIM\text{-}L}$. $I_{HIGH\text{-}SIC} - I_{CLIM\text{-}H}$ is referred to as the high-SIC response, and $I_{LOW\text{-}SIC} - I_{CLIM\text{-}L}$ is referred to as the low-SIC response in the remaining text. Daily response values were averaged to monthly values for most of the presented results, and statistical significance of the responses was determined at the 95% confidence level by bootstrapping the distributions of each response 1000 times (e.g., Efron 1979).

3.4 Results

3.4.1 Response of High-SIC Initial Conditions to the High-SIC Atmosphere

Figure 3.2a–c shows the monthly mean responses of SIC over the Barents Sea for high-SIC initial conditions and boundary forcing by $A_{HIGH\text{-}SIC}$. In all three months, the sign of the SIC response is positive, indicating a positive sea ice-atmosphere feedback over the Barents Sea; that is, for the same high-SIC initial conditions, $A_{HIGH\text{-}SIC}$ atmospheric conditions produce more sea ice over the Barents Sea than

A_{CLIM} conditions. The magnitudes and extents of the SIC responses follow the evolution of the SIC anomalies used to force $A_{HIGH\text{-}SIC}$ (Fig. 3.1a–c), decreasing from December to February. Statistically significant SIC responses are confined to the Barents Sea in all months except February, when small positive and negative responses are present over the Bering Sea (not shown), indicating that the positive sea ice-atmosphere feedback is a local feature despite the presence of NAO-like large-scale circulation differences in the boundary forcing atmospheres of the experiment and the control (Liptak and Strong 2014).

In December, the response of the rate of change in SIC due to thermodynamics (ΔTHM, Fig. 3.3a) is positive over most of the corresponding SIC response (Fig. 3.2a), indicating that thermodynamic processes contribute to the positive feedback except over the western Barents Sea where the ΔTHM response is negative. In contrast, the subsequent ΔTHM response patterns (Fig. 3.3b, c) are weaker, being positive over the center of the SIC response region and negative elsewhere. As detailed later in this subsection, these ΔTHM effects stem principally from downwelling longwave forcing associated with anomalously low air temperatures in the $A_{HIGH\text{-}SIC}$ boundary conditions. Figure 3.3d–f (shading) shows that the responses of the rate of change in SIC from dynamics (ΔDYN) are similar for each month, with negative anomalies over the center of the SIC response region where the wind stress response is divergent (arrows, Fig. 3.3d–f), and positive anomalies over the western edge where the wind stress response is convergent.

Illustrating the temporal evolution of the response, Fig. 3.4a shows that daily

mean Barents Sea SIC is greater in $I_{HIGH\text{-}SIC}$ than $I_{CLIM\text{-}H}$ for most of the winter, with both values converging in February as the SIC anomaly used to force $A_{HIGH\text{-}SIC}$ weakens (Fig. 3.1a–c) and the ice cover increases. As a result, the daily mean SIC response over the Barents Sea (Fig. 3.4b) maximizes in mid-December, then steadily declines in January and February, remaining positive throughout the winter. The daily ΔTHM response (Fig. 3.4c) starts out positive, peaks in December, then oscillates around zero for the remainder of winter. The daily ΔDYN response (Fig. 3.4c) is weaker and predominantly negative. Thus, the daily and monthly mean ΔTHM and ΔDYN responses indicate that the positive SIC response over the Barents Sea is thermodynamically driven and that dynamical processes (i.e, deformation and transport) tend to oppose the feedback.

Monthly mean differences in the atmospheric boundary conditions provided by $A_{HIGH\text{-}SIC}$ and A_{CLIM} show that negative downwelling surface longwave radiation anomalies (Fig. 3.5a–c) align with positive ΔTHM anomalies (Fig. 3.3a–c) over the centers of the corresponding positive SIC responses. The responses in temperature advection, calculated by applying $-\mathbf{V}\cdot\nabla T$ to the lowest model level temperature and wind components, show opposite-signed anomalies over the eastern and western sides of the ice anomaly region (Fig. 3.5d–f). These dipole patterns match the expected response given a packet of anomalously cold air over the added sea ice and act to somewhat weaken the cold anomaly. More specifically, positive temperature advection anomalies in the high-SIC atmosphere over the eastern SIC response region are consistent with large-scale flow from the relatively warm continent over positive

SIC anomalies shown in Fig. 3.1a–c, and negative temperature advection anomalies near the western edge of the SIC response region result from flow over the positive SIC anomalies toward the exposed ocean. The surface shortwave radiation response (not shown) is small and limited to the end of February when polar night ends over the southern half of the Barents Sea.

The alignment of the negative downwelling longwave radiation anomalies with the SIC responses and negative low-level temperature anomalies (not shown) throughout the winter indicates that surface longwave forcing drives the positive sea ice-atmosphere feedback by providing a persistent source of anomalously cold air over the Barents Sea. Effects more directly related to wind, including wind stress divergence and temperature advection, only partially offset the longwave radiative-driven increase in ice.

3.4.2 Response of Low-SIC Initial Conditions to the Low-SIC Atmosphere

The monthly mean SIC responses for the low-SIC experiment (Fig. 3.2d–f) show a localized positive sea ice-atmosphere feedback over the Barents Sea throughout the winter, with statistically significant SIC responses limited to the Barents Sea until February when smaller negative SIC anomalies are also present in the Labrador Sea and Sea of Okhotsk (not shown). The monthly ΔTHM (Fig. 3.6a–c) and ΔDYN (Fig. 3.6d–f) responses depict patterns that are analogous to the corresponding high-SIC responses but opposite in sign and indicate that thermodynamic processes

outweigh dynamics to reduce SIC over the Barents Sea in the low-SIC response.

Temporally, daily mean Barents Sea SIC (Fig. 3.4a) increases in $I_{\text{LOW-SIC}}$ and $I_{\text{CLIM-L}}$ throughout the winter, converging in February as the SIC anomaly used to force $A_{\text{LOW-SIC}}$ weakens (Fig. 3.1d–f) and producing a negative daily SIC response that peaks in December (Fig. 3.4b). The strong negative ΔTHM response in December (Fig. 3.4c) outweighs the positive response in January and the weak positive ΔDYN response (Fig. 3.4d), resulting in the negative monthly mean SIC responses shown in Fig. 3.2d–f. Initially, the thermodynamic forcing is stronger in the low-SIC experiment than in the high-SIC experiment (Fig. 3.4c), reflecting the differences in the strength of the SIC anomalies used to force $A_{\text{LOW-SIC}}$ and $A_{\text{HIGH-SIC}}$ (Fig. 3.1). As a result, the SIC response in the low-SIC experiment becomes negative a few hours following initialization (not shown), producing a negative daily average 1 December SIC response (Fig. 3.4b), whereas the high-SIC response visibly differs from zero after approximately 2 days.

The difference in atmospheric boundary conditions ($A_{\text{LOW-SIC}} - A_{\text{CLIM}}$) shows positive downwelling longwave radiation anomalies over the SIC response region (Fig. 3.7a–c) that result from increased longwave radiation at the surface in $A_{\text{LOW-SIC}}$. As in the high-SIC experiment, positive low-level temperature anomalies (not shown) that are collocated with the positive SIC responses indicate that longwave forcing produces anomalously warm air that drives the positive sea ice-atmosphere feedback. Dipole patterns in the temperature advection response (Fig. 3.7d–f) are again consistent with, and somewhat weaken, the positive temperature anomalies over

the area where ice cover is reduced. Negative temperature advection anomalies over the eastern SIC response region result from increased cold advection in $A_{LOW\text{-}SIC}$ as offshore flow moves over the negative SIC anomalies. Surface wind stress convergence (arrows, 3.6d–f) aligns with the positive ΔDYN response (shading, 3.6d–f) and opposes the positive sea ice-atmosphere feedback over the center of the SIC response, while divergence supports the feedback over the western edge where the ΔDYN response is negative.

3.5 Discussion and Conclusions

The winter responses of Barents Sea ice to atmospheric boundary conditions generated by daily positive and negative SIC anomalies indicate a sea ice-atmosphere feedback that is local and positive despite the presence of large-scale NAO-like changes in the atmospheric circulation. The positive feedback was thermodynamically driven, where negative surface downwelling longwave radiation anomalies increased SIC in the high-SIC experiment, and positive downwelling longwave radiation anomalies decreased SIC in the low-SIC experiment. In both experiments, temperature advection opposed the positive feedback by weakening ice-induced air temperature anomalies. Dynamical forcing countered the positive feedback due to surface wind stress divergence over the Barents Sea in the high-SIC experiment and wind stress convergence in the low-SIC experiment. The magnitude of the positive feedback peaked in December and decreased during the remaining winter months as the strength of the atmospheric forcing declined and the ice filled in.

Our results contrast the large-scale NAO-driven negative sea ice-atmosphere feedback over the Barents Sea implied by and investigated in prior work (Magnusdottir et al. 2004; Strong et al. 2009; Strong and Magnusdottir 2010) and highlight how local processes may influence the sign of the overall feedback. Importantly, results here are based on decomposing the feedback into sequential boundary forcing experiments using standalone sea ice and atmosphere components. The uncoupled atmosphere provided sources of sustained anomalously cold and warm air over the Barents Sea so that the thermodynamic forcing from downwelling longwave flux anomalies outweighed advection and dynamic forcing and determined the net sea ice responses. Had the sea ice been coupled to the atmosphere, dynamic forcing would have likely played a larger role in determining the sign and magnitude of the feedback as demonstrated by Koenigk et al. (2009), who found that ice transport between the Barents Sea and Central Arctic was the main driver of the interannual variability of sea ice volume over the Barents Sea in the coupled sea ice-ocean-atmosphere model. Using May–September 1990 boundary conditions, Maslanik et al. (2000) showed that sea ice loss in the eastern Arctic in a standalone dynamic-thermodynamic ice model primarily resulted from melting, while both melting and ice divergence contributed to sea ice loss in a coupled sea ice-atmosphere-SOM model. Local differences in the variance of the atmospheric responses in coupled and uncoupled models forced with identical boundary conditions are related to variations in the interference of SST-forced responses with weather-related "noise" (Chen et al. 2013), and Bretherton and Battisti (2000) provide additional insights into the dynamics

and interpretation of boundary-forcing experiments. Work is underway to further examine the sea ice-atmosphere feedback by allowing and suppressing it in a coupled modeling framework.

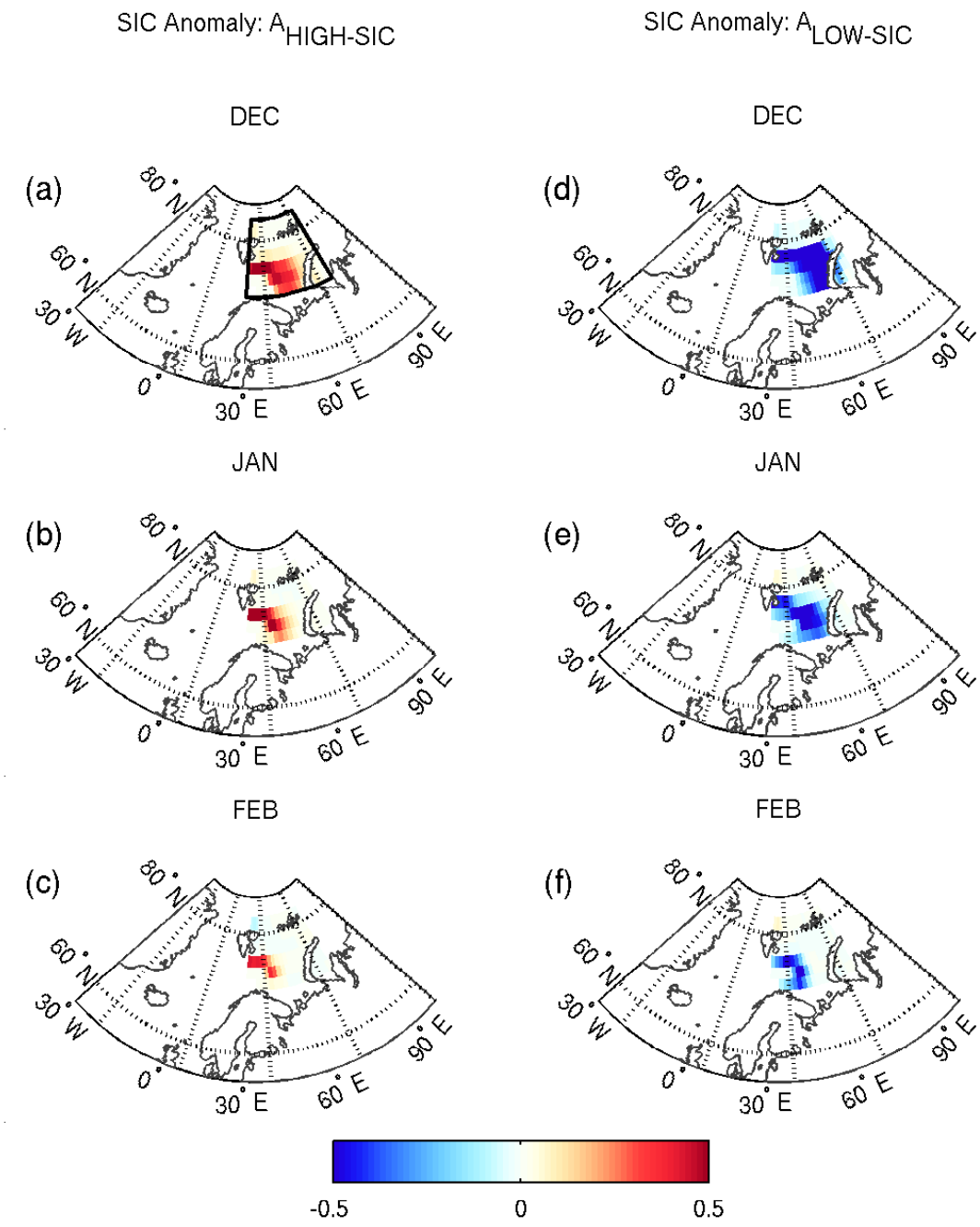

Fig. 3.1. Monthly means (December, January, and February) of the daily SIC anomalies (fraction) used to force CAM in the (a)–(c) high-SIC and (d)–(f) low-SIC experiments. The black box in (a) outlines the area used to define the Barents Sea.

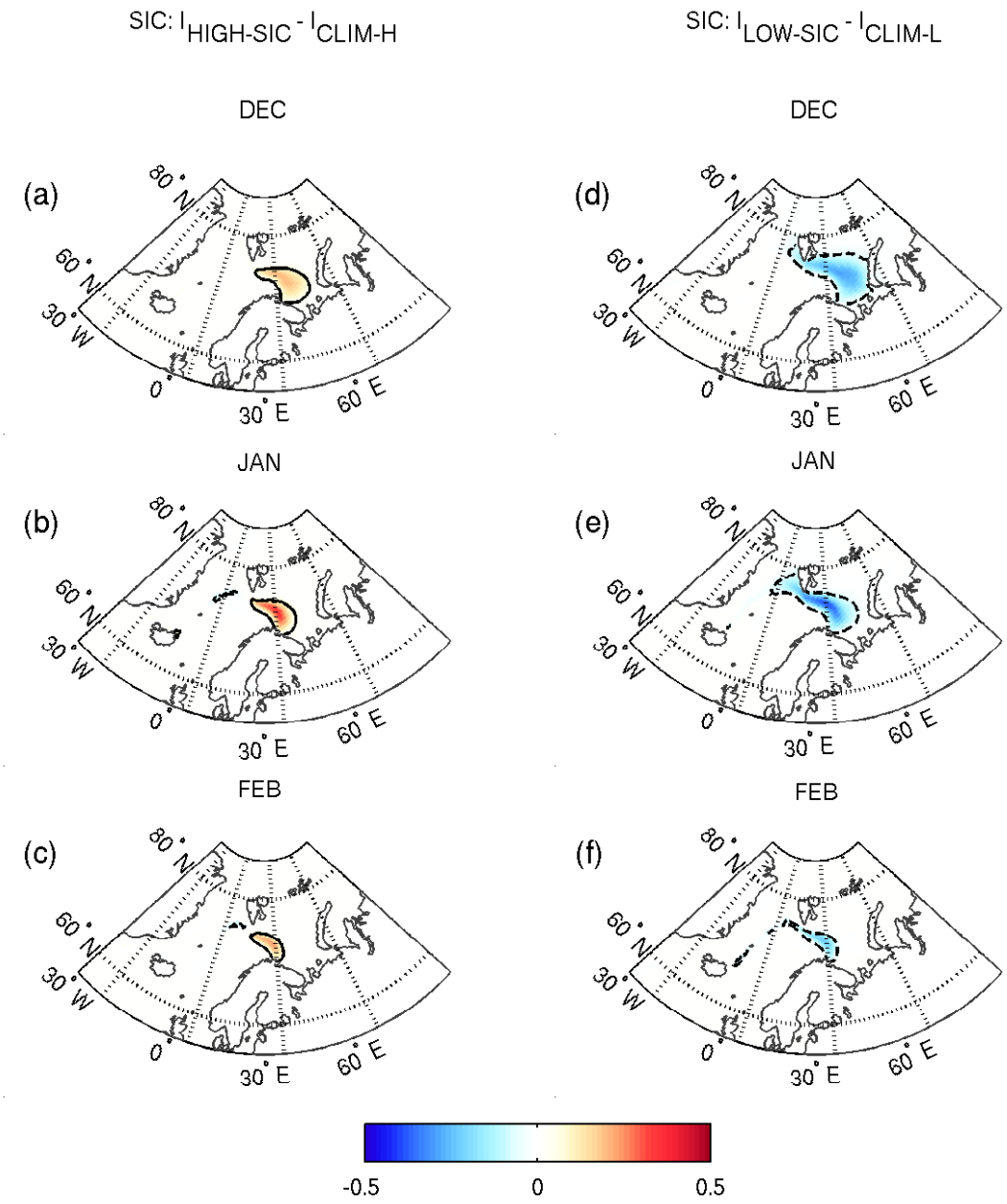

Fig. 3.2. Monthly mean responses of SIC (fraction) over the Barents Sea for the (a)–(c) high-SIC and (d)–(f) low-SIC CICE experiments. Values that are statistically significant at the 95% confidence level are shaded. Solid and dashed curves indicate the 0.05 and -0.05 contours.

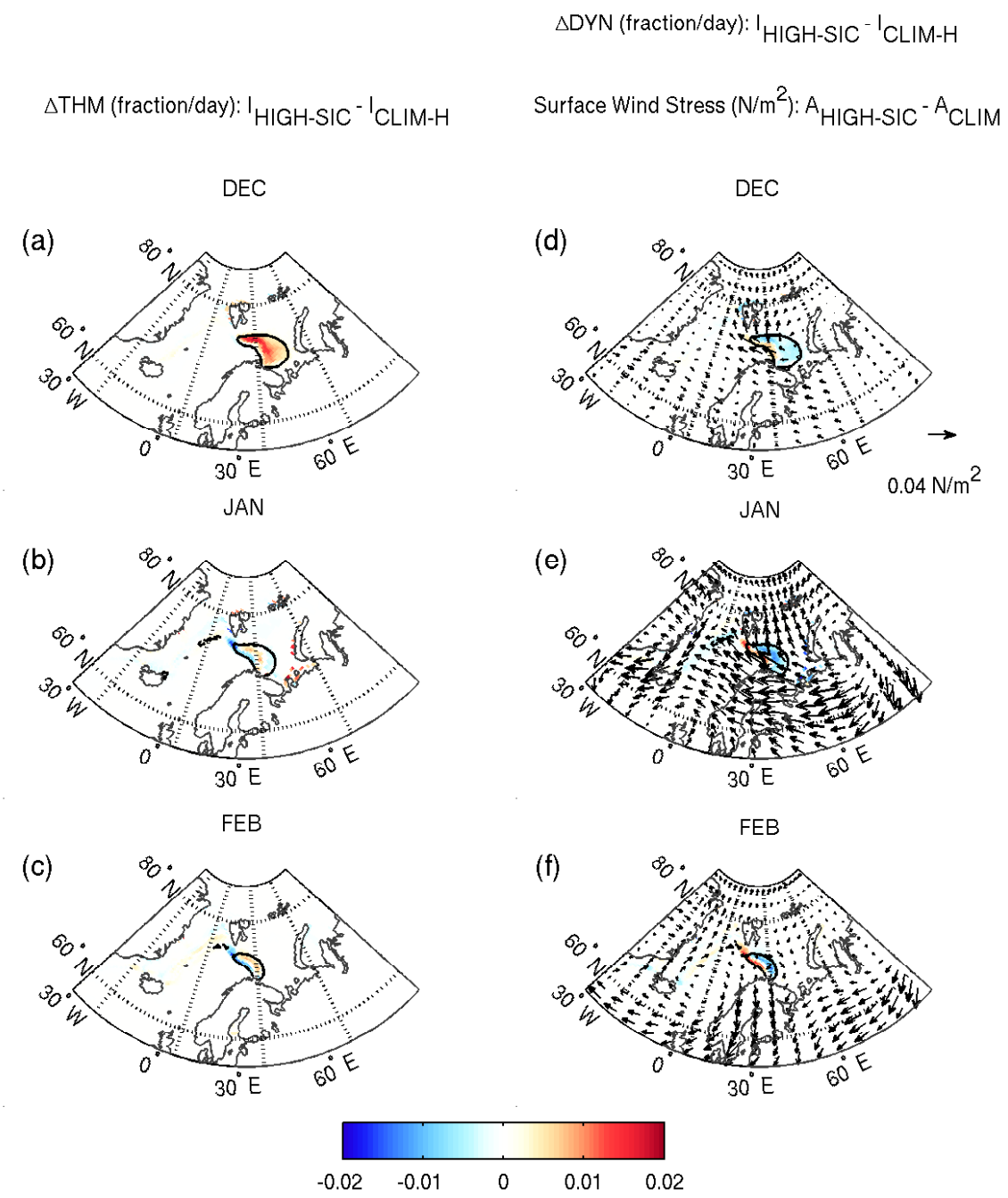

Fig. 3.3. For the high-SIC experiments: monthly mean responses of the change in SIC due to thermodynamics (a)–(c) and (d)–(f) the change in SIC due to dynamics (shading). Units are fraction/day. Arrows show the wind stress anomaly (N/m2) for $A_{\text{HIGH-SIC}} - A_{\text{CLIM}}$. Black solid and dashed curves are copied from Fig. 3.2. Values are shaded where the ΔTHM responses in (a)–(c) and ΔDYN responses in (d)–(f) are statistically significant at the 95% confidence level.

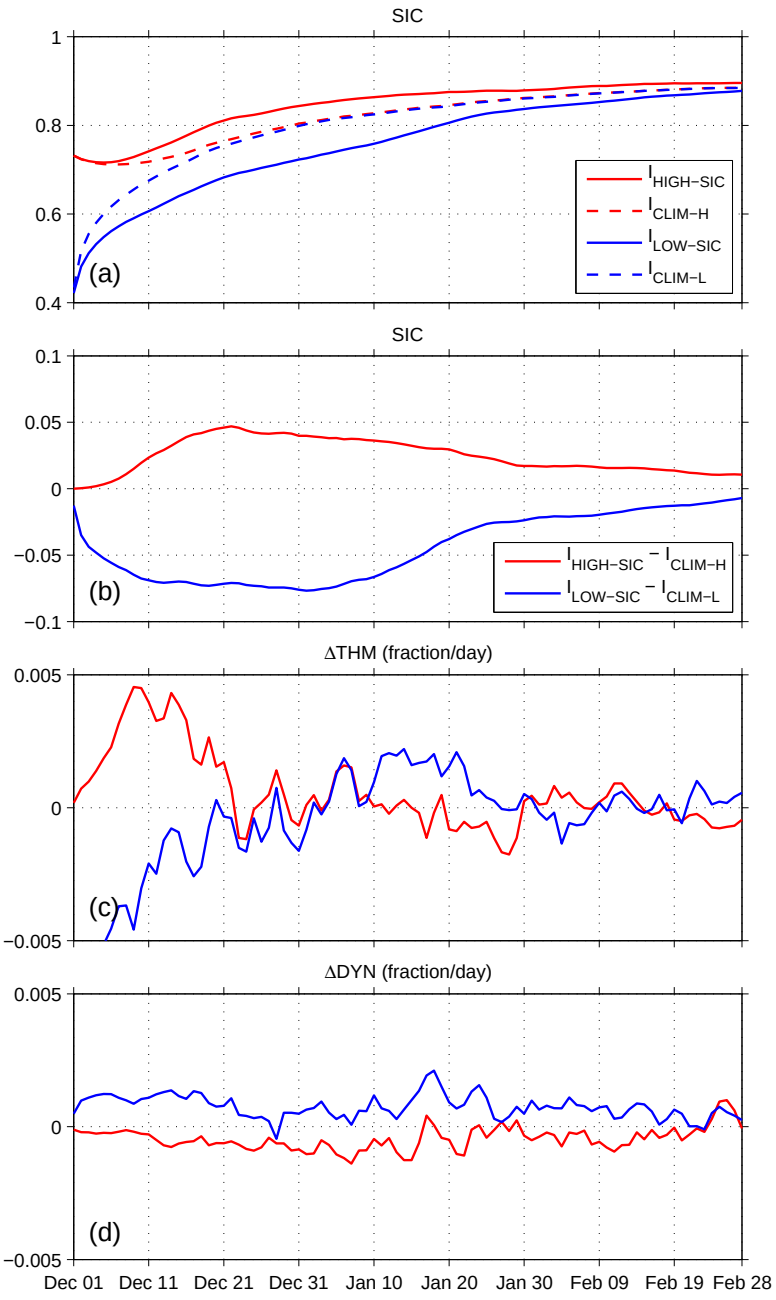

Fig. 3.4. Daily means of SIC and the responses of the changes in SIC for the high-SIC (red lines) and low-SIC (blue lines) experiments. (a) Daily mean SIC (fraction) over the Barents Sea for the high-SIC experiment (solid red line) and control run (dashed red line) and the low-SIC experiment (solid blue line) and control run (dashed blue line). Responses of the daily means in (b) SIC (fraction), (c) the change in SIC due to thermodynamics, and (d) the change in SIC due to dynamics for the high-SIC (solid red lines) and low-SIC (solid blue lines) conditions. The blue curve in (c) begins off the scale at -0.03 on 1 December.

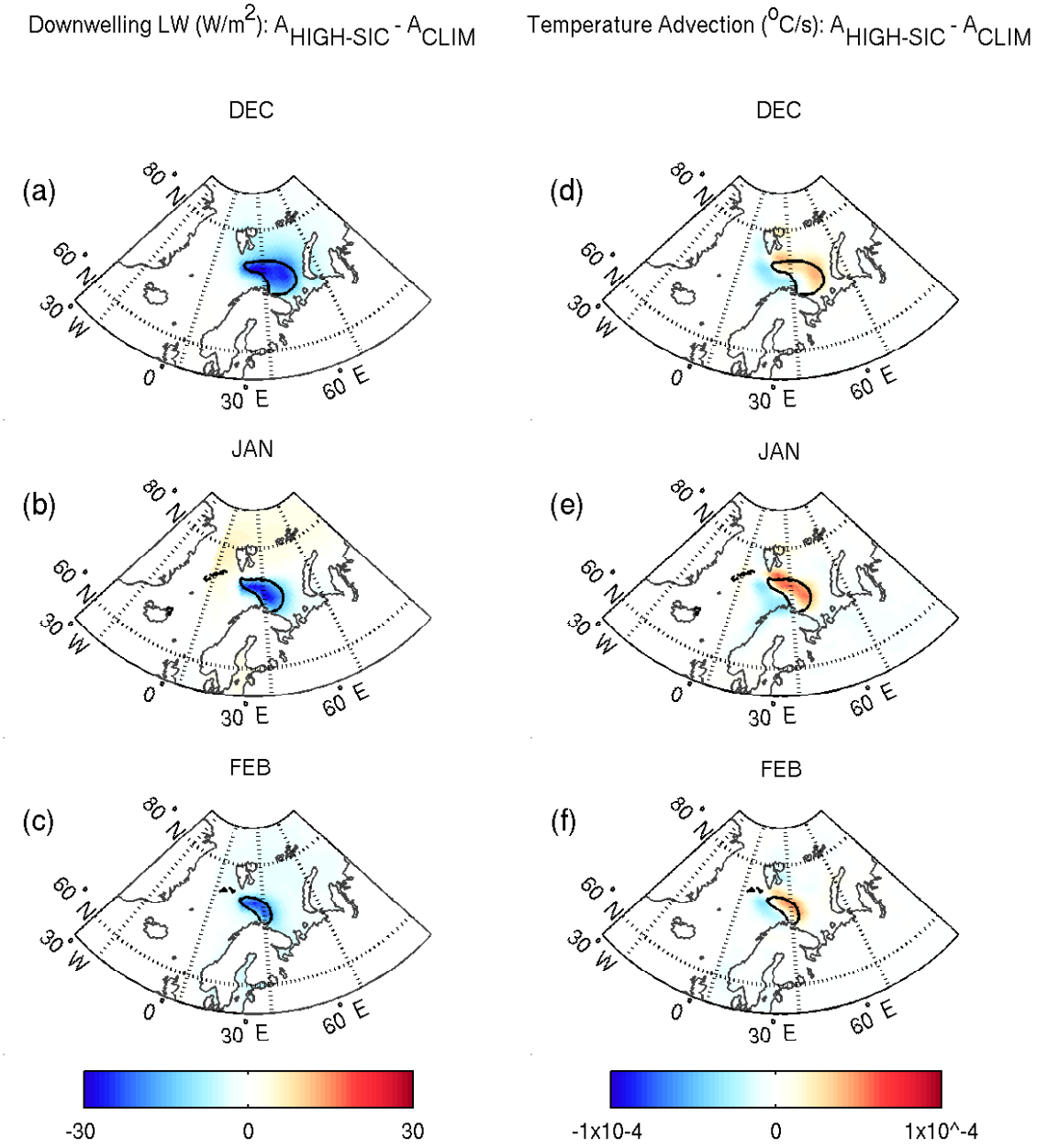

Fig. 3.5. Difference in atmospheric boundary conditions calculated as $A_{\text{HIGH-SIC}} - A_{\text{CLIM}}$: (a)–(c) downwelling longwave radiation flux at the surface (W/m^2) and (d)–(f) temperature advection (°C/s) at the lowest model level. Black solid and dashed curves are copied from Fig. 3.2. The responses have been linearly interpolated from the regular CAM grid to the displaced pole CICE grid for display only.

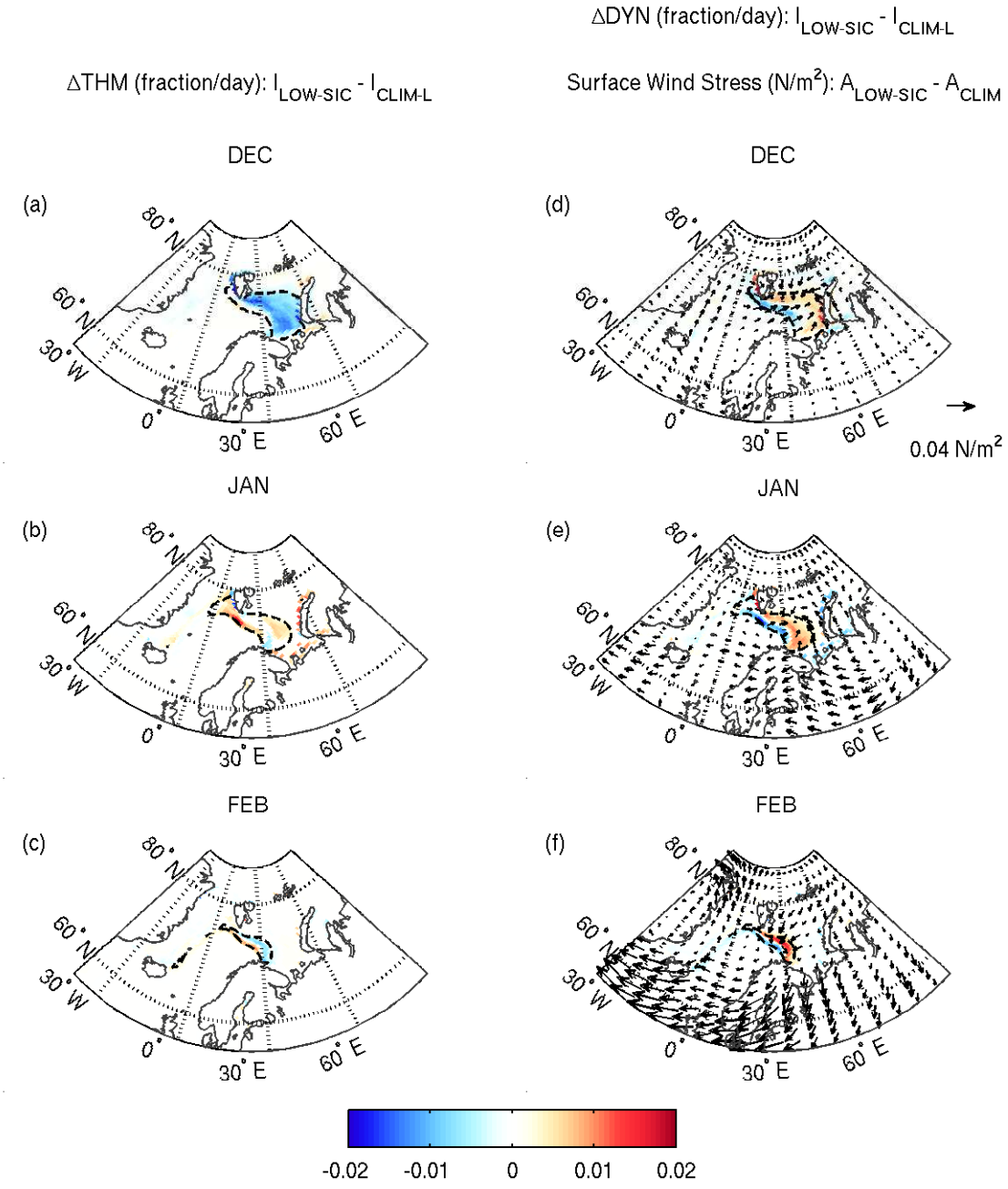

Fig. 3.6. As in Fig. 3.3, but for the low-SIC experiment.

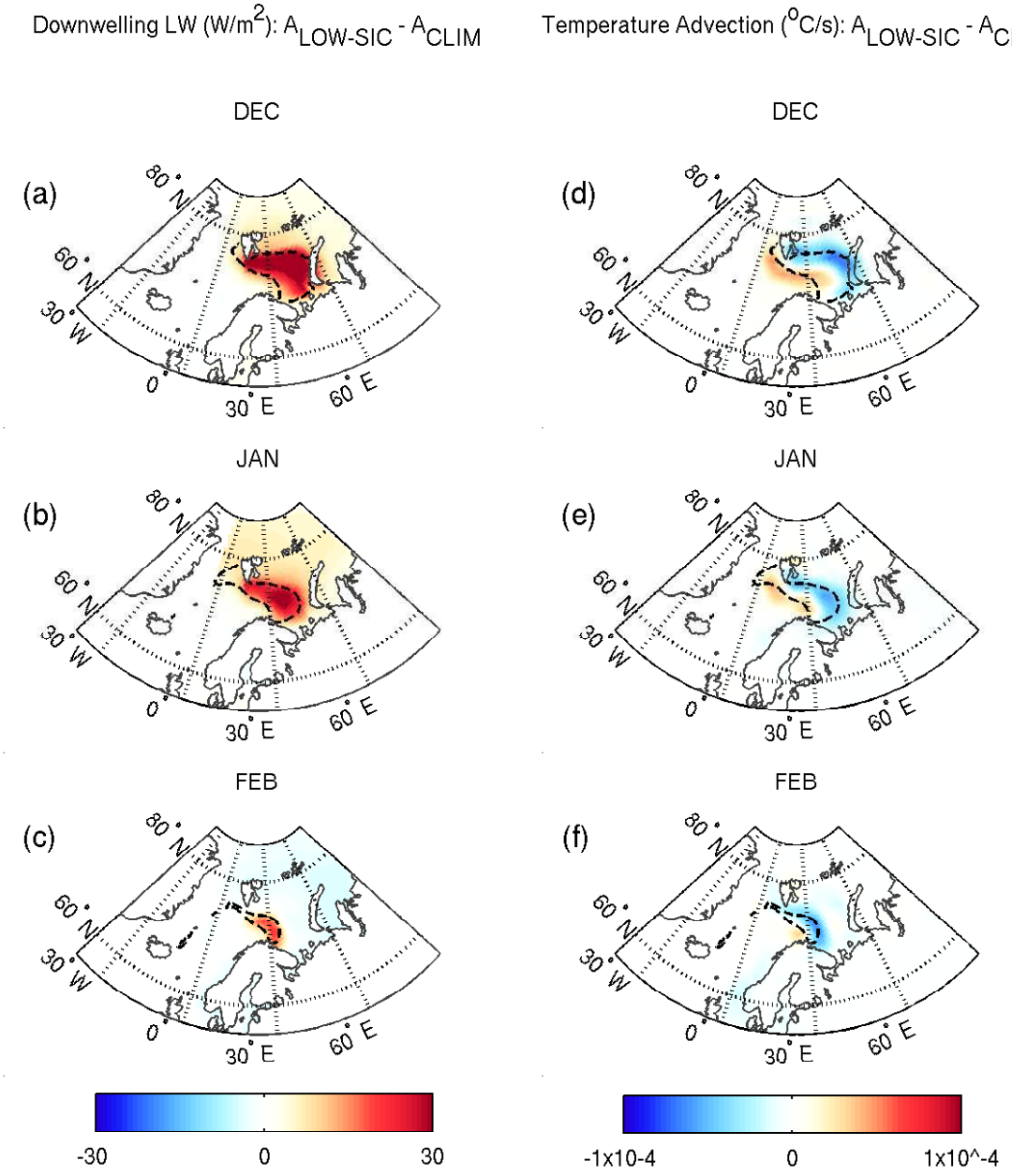

Fig. 3.7. As in Fig 3.5, but for the low-SIC experiment.

Table 3.1. The simulation name is given, along with the associated model and a summary of the boundary and initial conditions used.

Name	Model	Initial Conditions	Boundary Conditions	Role
A_{100}	CAM	default	HadOIBl	control
I_{100}	CICE	default	A_{100}	control
$A_{\text{HIGH-SIC}}$	CAM	1 December from each year of A_{100}	$BC_{\text{HIGH-SIC}}$	experiment
$A_{\text{LOW-SIC}}$	CAM	1 December from each year of A_{100}	$BC_{\text{LOW-SIC}}$	experiment
A_{CLIM}	CAM	1 December from each year of A_{100}	BC_{CLIM}	control
$I_{\text{HIGH-SIC}}$	CICE	1 December from each year of $BC_{\text{HIGH-SIC}}$	$A_{\text{HIGH-SIC}}$	experiment
$I_{\text{CLIM-H}}$	CICE	1 December from each year of $BC_{\text{HIGH-SIC}}$	A_{CLIM}	control
$I_{\text{LOW-SIC}}$	CICE	1 December from each year of $BC_{\text{LOW-SIC}}$	$A_{\text{LOW-SIC}}$	experiment
$I_{\text{CLIM-L}}$	CICE	1 December from each year of $BC_{\text{LOW-SIC}}$	A_{CLIM}	control

3.6 References

Alexander, M. A., U. S. Bhatt, J. E. Walsh, M. S. Timlin, J. S. Miller, and J. D. Scott, 2004: The atmospheric response to realistic Arctic sea ice anomalies in an AGCM during winter. *J. Climate*, **17**, 890–905.

Bretherton, C. S., and D. S. Battisti, 2000: An interpretation of the results from atmospheric general circulation models forced by the time history of the observed sea surface temperature distribution. *Geophy. Res. Lett.*, **27** (6), 767–770, doi:10.1029/1999GL010910.

Chen, H., E. K. Shneider, B. P. Kirtman, and I. Colfescu, 2013: Evaluation of weather noise and its role in climate model simulations. *J. Climate*, **26** (11), 3766–3784, doi:10.1175/JCLI-D-12-00292.1.

Deser, C., G. Magnusdottir, R. Saravanan, and A. S. Phillips, 2004: The effects of North Atlantic SST and sea-ice anomalies on the winter circulation in CCM3. Part II: Direct and indirect components of the response. *J. Climate*, **17**, 877–889, doi:10.1175/1520-0442(2004)017$⟨$0877:TEONAS$⟩$2.0.CO;2.

Deser, C., J. E. Walsh, and M. S. Timlin, 2000: Arctic sea ice variability in the context of recent atmospheric circulation trends. *J. Climate*, **13**, 617–633.

Efron, B., 1979: Bootstrap methods: Another look at the jackknife. *Ann. Stat.*, **7**, 1–26.

Gent, P. R. et al., 2011: The Community Climate System Model version 4. *J. Climate*, **24**, 4973–4991, doi:10.1175/2011JCLI4083.1.

Hilmer, M., and T. Jung, 2000: Evidence for a recent change in the link between the North Atlantic Oscillation and Arctic sea ice export. *Geophys. Res. Lett.*, **27** (7), 989–992, doi:10.1029/1999GL010944.

Hunke, E. C., and W. H. Lipscomb, 2008: CICE: The Los Alamos sea ice model user's manual, version 4. Tech. Rep. LA-CC-06-012, Los Alamos National Laboratory.

Hurrell, J. W., J. J. Hack, D. Shea, J. M. Caron, and J. Rosinski, 2008: A new sea surface temperature and sea ice boundary dataset for the Community Atmosphere Model. *J. Climate*, **21** (19), 5145–5153, doi:10.1175/2008JCLI2292.1.

Hurrell, J. W., Y. Kushnir, G. Ottersen, and M. Visbeck, 2003: *The North Atlantic Oscillation: Climate Significance and Environmental Impact*. Amer. Geophys. Union, 27 pp.

Koenigk, T., U. Mikolajewicz, J. H. Jungclaus, and A. Kroll, 2009: Sea ice in the Barents Sea: Seasonal to interannual variability and climate feedbacks in a global coupled model. *Climate Dyn.*, **32**, 1119–1138.

Kwok, R., G. F. Cunningham, and S. S. Pang, 2004: Fram Strait sea ice outflow. *J. Geophys. Res.*, **109** (C1), C01 009, doi:10.1029/2003JC001785.

Kwok, R., and D. A. Rothrock, 1999: Variability of Fram Strait ice flux and North Atlantic Oscillation. *J. Geophys. Res*, **104**, 5177–5189, doi:10.1029/1998JC900103.

Lin, S.-J., 2004: A "vertically Lagrangian" finite-volume dynamical core for global models. *Mon. Wea. Rev.*, **132**, 2293–2307, doi:10.1175/1520-0493(2004)132$\langle$$2293:AVLFDC$\rangle$$2.0.CO;2.

Liptak, J., and C. Strong, 2014: The winter atmospheric response to sea ice anomalies in the Barents Sea. *J. Climate*, **27**, 914–924, doi:10.1175/JCLI-D-13-00186.1.

Magnusdottir, G., C. Deser, and R. Saravanan, 2004: The effects of North Atlantic SST and sea ice anomalies on the winter circulation in CCM3. Part I: Main features and storm track characteristics of the response. *J. Climate*, **17**, 857–876, doi:10.1175/1520-0442(2004)017$\langle$$0857:TEONAS$\rangle$$2.0.CO;2.

Maslanik, J. A., A. H. Lynch, M. C. Serreze, and W. Wu, 2000: A case study of regional climate anomalies in the Arctic: Performance requirements for a coupled model. *J. Climate*, **13** (2), 383–401, doi:10.1175/1520-0442(2000)013$\langle$$0383:ACSORC$\rangle$$2.0.CO;2.

Nansen, F., 1902: *The Oceanography of the North Polar Basin*. Longmans, Green, and Company, http://books.google.com/books?id=M4ZaHAAACAAJ.

Neale, R. B. et al., 2010: Description of the NCAR Community Atmosphere Model (CAM 4.0). Tech. Rep. NCAR/TN-485+STR, National Center For Atmospheric Research, Boulder, CO, USA.

Ogi, M., and I. G. Rigor, 2013: Trends in Arctic sea ice and the role of atmospheric circulation. *Atmos. Sci. Lett.*, **14** (2), 97–101, doi:10.1002/asl2.423.

Ogi, M., I. G. Rigor, M. G. McPhee, and J. M. Wallace, 2008: Summer retreat of Arctic sea ice: Role of summer winds. *Geophys. Res. Lett.*, **35**, L24 701, doi:10.1029/2007GL029897.

Ogi, M., and J. M. Wallace, 2007: Summer minimum Arctic sea ice extent and the associated summer atmospheric circulation. *Geophys. Res. Lett.*, **34** (12), L12 705, doi:10.1029/2007GL029897.

Ogi, M., K. Yamazaki, and J. M. Wallace, 2010: Influence of winter and summer surface wind anomalies on summer Arctic sea ice extent. *Geophys. Res. Lett.*, **37** (7), L07 701, doi:10.1029/2009GL042356.

Ou, H.-W., 2013: A box model of the Arctic natural variability. *Climate Dyn.*, **40** (7-8), 1687–1706, doi:10.1007/s00382-012-1453-6.

Rigor, I. G., J. M. Wallace, and R. L. Colony, 2002: Response of sea ice to the Arctic Oscillation. *J. Climate*, **15**, 2648–2663, doi:10.1175/1520-0442(2002)015⟨2648:ROSITT⟩2.0.CO;2.

Seierstad, I., and J. Bader, 2009: Impact of a projected future Arctic sea ice reduction on extratropical storminess and the NAO. *Climate Dyn.*, **33** (7), 937–943, doi:10.1007/s00382-008-0463-x.

Strong, C., and G. Magnusdottir, 2010: Dependence of NAO variability on coupling with sea ice. *Climate Dyn.*, **36**, 1681–1689, doi:10.1007/s00382-010-0752-z.

Strong, C., G. Magnusdottir, and H. Stern, 2009: Observed feedback between winter sea ice and the North Atlantic Oscillation. *J. Climate*, **22**, 6021–6032.

Thorndike, A. S., and R. Colony, 1982: Sea ice motion in response to geostrophic winds. *J. Geophys. Res.*, **87** (C8), 5845–5852.

Tsukernik, M., C. Deser, M. Alexander, and R. Tomas, 2010: Atmospheric forcing of Fram Strait sea ice export: A closer look. *Climate Dyn.*, **35**, 1349–1360.

Vinje, T., 2001: Anomalies and trends in sea-ice extent and atmospheric circulation in the Nordic Seas during the period 1864–1998. *J. Climate*, **14**, 3503–3517.

Wang, J., J. Zhang, E. Watanabe, M. Ikeda, K. Mizobata, J. E. Walsh, X. Bai, and B. Wu, 2009: Is the Dipole Anomaly a major driver to record lows in Arctic summer sea ice extent? *Geophys. Res. Lett.*, **36**, L05 706, doi:10.1029/2008GL036706.

Watanabe, E., and H. Hasumi, 2005: Arctic sea ice response to wind stress variations. *J. Geophys. Res.*, **110** (C11), C11 007, doi:10.1029/2004JC002678.

Wu, B., J. Wang, and J. E. Walsh, 2006: Dipole anomaly in the winter Arctic atmosphere and its association with sea ice motion. *J. Climate*, **19** (2), 210–225, doi:10.1175/JCLI3619.1.

Zhang, J., R. Woodgate, and R. Moritz, 2010: Sea ice response to atmospheric and oceanic forcing in the Bering Sea. *J. Phys. Oceanogr.*, **40** (8), 1729–1747, doi:10.1175/2010JPO4323.1.

Zhang, X., M. Ikeda, and J. E. Walsh, 2003: Arctic sea ice and freshwater changes driven by the atmospheric leading mode in a coupled sea ice-ocean model. *J. Climate*, **16**, 2159–2177, doi:10.1175/2758.1.

Zubov, N. N., 1943: *Arctic Ice*. San Diego, Calif.,U.S. Navy Electronics Laboratory, 506 pp., http://www.biodiversitylibrary.org/bibliography/39101.

CHAPTER 4

A MODELING INVESTIGATION OF THE ARCTIC SEA ICE-ATMOSPHERE FEEDBACK

4.1 Abstract

We examine the effects of suppressing the sea ice-atmosphere feedback over the Barents Sea by turning it on and off in a coupled climate model. We define a local sea ice-atmosphere feedback as the interaction among changes in sea ice cover, the exchange of turbulent and longwave heat fluxes between the surface and the atmosphere, and near-surface air temperature and wind stress responses. This feedback is "turned off" by forcing the atmosphere with surface turbulent and longwave heat fluxes and temperature that reflect cliamtological sea ice cover over the Barents Sea, while allowing the sea ice and sea surface temperature (SST) to freely evolve. Suppressing the feedback reduces the variability of bottom-level atmospheric temperature, sea ice cover, and SST averaged over the Barents Sea, confirming the existence of a positive thermodynamically driven sea ice-atmosphere feedback found in prior uncoupled modeling studies. Decreased interannual variability drives the total change in variability, and the largest reductions in variability occur during the

winter sea ice growth and spring melt seasons.

4.2 Introduction

Sea ice acts as a barrier between the ocean and atmosphere, reflecting incoming solar radiation and controlling heat exchanged through surface turbulent heat and longwave fluxes. Changes in energy exchange between the surface and atmosphere caused by sea ice drift, melting, and freezing induce local and remote atmospheric responses that further enhance or oppose the original sea ice configuration in a relationship known as a feedback. The decline in Arctic sea ice over the past few decades is linked to several feedback processes (Serreze et al. 2007), most notably the ice albedo feedback (Curry et al. 1995a). The ice albedo feedback is primarily responsible for overall Arctic warming (Pithan and Mauritsen 2014) and has hastened ice loss by lengthening the melt season (Stroeve et al. 2014) and thinning the Arctic ice pack (Maslanik et al. 2007b; Kwok et al. 2009).

Changes in surface wind act in tandem with the ice albedo feedback to reduce sea ice volume by increasing the export of sea ice from the Arctic (Nghiem et al. 2007; Smedsrud et al. 2011), most of which exits through the Fram Strait (Kwok et al. 2004). Sea ice export is largely driven by basin-scale circulation anomalies associated with the Arctic Oscillation (AO; Rigor and Wallace 2004; Perovich and Richter-Menge 2009), where the positive AO phase enhances sea ice export and regional atmospheric variability that affects the east-west pressure gradient over the Fram Strait (Vinje 2001; Wu et al. 2006; Maslanik et al. 2007a; Tsukernik et al. 2010).

In contrast, the relationship between the North Atlantic Oscillation (NAO) and Fram Strait sea ice export is weak due to variability in the location of the Icelandic Low (Jung and Hilmer 2001).

The NAO does affect the interannual and seasonal variability of North Atlantic sea ice cover (e.g., Deser et al. 2000; Ukita et al. 2007; Parkinson and Cavalieri 2008), and several studies suggest that a negative feedback exists between the NAO and sea ice east of Greenland in the winter (Alexander et al. 2004; Magnusdottir et al. 2004; Yamamoto et al. 2006; Strong et al. 2009; Strong and Magnusdottir 2010; Frankignoul et al. 2014), where anomalously low sea ice triggers atmospheric circulation features resembling the negative phase of the NAO with negative pressure anomalies over the North Atlantic, resulting in surface wind stress anomalies that advect sea ice back to the location of initial ice removal.

While the ice albedo feedback is the main source of Arctic warming, Pithan and Mauritsen (2014) found that the lapse rate feedback contributes the most to Arctic amplification because it increases Arctic warming and decreases tropical warming. The sign of the lapse rate feedback depends on the amount of coupling between the lower and upper atmosphere and is positive in the Arctic because the persistent inversion confines temperature changes to the lower atmosphere.

Pithan and Mauritsen (2014) also highlight the role of the Planck feedback in Arctic amplification of global warming, where the surface temperature must increase more in polar regions than the tropics to compensate for a given negative top-of-atmosphere (TOA) radiation balance (i.e., there is more outgoing longwave

radiation than incoming shortwave radiation). The Planck feedback describes the relationship between terrestrial temperature (T_e) and longwave radiation emitted by the surface (F_s), expressed as

$$F_s = \epsilon \sigma T_e^4 \tag{4.1}$$

where σ is the Stephan-Boltzmann constant, and ϵ is the surface emissivity, which is approximately 1; thus, a cold surface like sea ice emits less longwave radiation than a warm surface such as the open ocean. It follows that a reduction in sea ice would enhance warming induced by the Planck feedback by permitting additional absorption and re-emission of radiation at the surface.

Reduced ice cover increases evaporation and atmospheric relative humidity, which warms the surface and leads to more ice loss through the water vapor feedback (Curry et al. 1995b). Variations in the surface moisture flux also affect cloud feedbacks, which may be positive or negative depending on their cloud phase, thickness, and season. Optically thick convective clouds that form over exposed ocean and melt ponds warm the Arctic relative to clear sky conditions during most of the year by increasing the downwelling longwave radiation flux and reflecting solar radiation, while high albedo causes Arctic clouds to have a net cooling effect on the surface in the summer (Intrieri et al. 2002). Thus, changing the variability in cold season sea ice or cloud fraction ought to induce a positive feedback as shown by Abbot et al. (2009) who found that Arctic sea ice decreased and the fractional coverage of low

clouds increased in response to quadrupled CO_2. In addition, Liu and Key (2014) attributed the increase in September Arctic sea ice cover between 2012 and 2013 to below-average winter cloud cover.

Typically, surface-atmosphere feedbacks are defined based on changes in the TOA radiation balance (e.g., Bony et al. 2006; Boé et al. 2009; Pithan and Mauritsen 2014). Here, we define a general sea ice-atmosphere feedback (SAF) with respect to sea ice depicted in Fig. 4.1 in which an initial change in sea ice cover (S) exposes or covers part of the ocean surface, leading to vertical exchanges of sensible, latent, and longwave heat (Q) between the surface and atmosphere. The surface fluxes increase or decrease the near-surface atmospheric temperature (T), resulting in a hydrostatic pressure adjustment and surface wind stress convergence or divergence (τ). The combined thermodynamic and dynamic effects of the temperature and wind stress responses create a new sea ice configuration that enhances (positive feedback) or opposes (negative feedback) the effects of S.

In two prior studies, we examined the SAF over the Barents Sea where the interaction between the atmosphere and leading pattern of sea ice variability during the winter is strongest (Magnusdottir et al. 2004). First, we evaluated the atmospheric responses to opposite-signed, daily varying sea ice concentration (SIC) anomalies (the part of the feedback represented by the purple arrow from S to Q and the red arrow from Q to T and τ in Fig. 4.1) by boundary forcing the standalone Community Atmosphere Model (CAM) with prescribed SIC superimposed with positive and negative anomalies over the Barents Sea during the winter (Liptak and Strong 2014b).

Next, we determined the feedback of the atmosphere onto the sea ice (the blue arrow from T and τ to S in Fig. 4.1) using atmospheric boundary conditions from the experiments in Liptak and Strong (2014b) to force the standalone Community Ice CoDE (CICE) model (Liptak and Strong 2014a). We found that the uncoupled SAF was positive and thermodynamically driven, where positive SIC anomalies locally cooled the atmosphere, leading to less downwelling longwave radiation and increased sea ice cover over the Barents Sea, while negative sea ice concentration anomalies warmed the atmosphere, increasing downwelling longwave radiation and reducing sea ice cover.

Here, we determine the sign and magnitude of the SAF in coupled modeling framework by assessing changes in the variability of the near-surface atmospheric temperature, sea ice, and sea surface temperature caused by "turning off" the SAF. Sensible, latent, and longwave heat fluxes and surface temperature sent from the surface to the atmosphere are replaced with values that reflect climatological sea ice cover over the Barents Sea—effectively eliminating the sea ice-to-atmosphere branch of the SAF (red arrow in Fig. 4.1). In addition, we discuss the implications for designing boundary-forcing experiments in uncoupled and coupled models.

4.3 Methods

4.3.1 Experimental Design

We ran a 120-year experiment (FLUX) and control (CTL) with version 4 of the NCAR Community Climate System Model (CCSM4; Gent et al. 2011). The

atmosphere component (CAM; Neale et al. 2010) has 26 vertical levels and was configured on a $1.9^\circ \times 2.5^\circ$ finite volume grid. The sea ice component (CICE; Hunke and Lipscomb 2008) was run on a 1° displaced-pole grid with the pole centered over Greenland and 5 thickness categories. The CAM and CICE model were coupled to a slab-ocean model (SOM), which computes ocean mixed layer temperatures from a prescribed seasonal cycle of heat transport values (Q-fluxes) as described by Bitz et al. (2012). We calculated the Q-fluxes from average 1985–2005 monthly mean output from ensemble member 1 of the CCSM4 20th-century CMIP5 run b40.20th.track1.1deg.005 following the procedure in Bailey et al. (2013). CTL and FLUX were initialized on 1 January using default initial conditions and were run with atmospheric chemistry prescribed at year 2000 values.

CICE, CAM, and the SOM send turbulent heat fluxes and other quantities to one another via a flux coupler (Kauffman et al. 2004). Before exporting surface variables to CAM, the flux coupler multiplies the variables imported from the land, ocean, and sea ice components (regridded to the CAM grid) by their respective area fractions of each grid cell, then sums the weighted values. In other words, the CAM "sees" the total amount of each surface variable weighted by the fractional coverage of each surface type.

For FLUX, we modified one of the flux coupler subroutines to adjust fractional ice cover from CICE to match climatological values over the Barents Sea (67°N–82°N, 20°E–65°E, black box in Fig. 4.2). Climatological fractional sea ice cover (or sea ice concentration) was calculated from long-term daily mean sea ice fraction taken from

the last 100 years of CTL. The ocean fraction was adjusted accordingly so that the total fractional coverage of land, sea ice, and ocean summed to 1 over each grid cell (the land fraction was constant and thus unaffected by changing the sea ice fraction). Surface sensible, latent, and longwave heat fluxes, and the surface temperature were weighted by the climatological sea ice and/or ocean fractions, then summed (along with any land values) before sending them to CAM. All other variables were weighted by the real sea ice and ocean fractions. Thus, we sent the CAM heat fluxes and surface temperatures representative of climatological sea ice cover while allowing the CICE model to evolve as usual, and we refer to this process as feedback suppression throughout the text.

4.3.2 Analysis

We analyzed daily average values of sea ice concentration (I) and sea surface temperature (SST) output from CICE and bottom-level atmospheric temperature (T) output from CAM, discarding the first 20 years to account for model spin-up. All data were detrended and their annual cycles were removed by subtracting the first harmonic (365-day period). We then decomposed the total variability of each I, T, and SST into between-season and within-season components. For a variable X, the temporal variance is defined as

$$\mathrm{var}(X) \equiv \frac{\sum_{n=1}^{N}(X_n - \bar{X})^2}{N-1}, \tag{4.2}$$

where N is the number of observations, $\bar{X}$ is the grand mean, and $N-1$ is the degrees of freedom. Total variance over the 100-year period is comprised of the variance between each season (i.e., interannual variability) and variance within each season. The between-season and within-season variances do not sum to the total variance, but their numerators sum to the numerator of (4.2), or total sum of squares (SS); thus, SS = SSB + SSW, where SSB is the between-season sum of squares

$$\mathrm{SSB} = D \sum_{y=1}^{Y} (\bar{X}_y - \bar{X})^2, \tag{4.3}$$

SSW is the within-season sum of squares

$$\mathrm{SSW} = \sum_{y=1}^{Y} \sum_{d=1}^{D} (X_{dy} - \bar{X}_y)^2, \tag{4.4}$$

where D is the number of days in each season, Y is the number of seasons (or years) in N, and $\bar{X}_y$ is the mean of season Y. The between-season and within-season variances may be calculated by dividing SSB by $Y-1$ and SSW by $Y(D-1)$ or $N-Y$.

We compared ratios of the FLUX and CTL variances ($\mathrm{var}(X_{\mathrm{FLUX}})/\mathrm{var}(X_{\mathrm{CTL}})$) to ratios of variances calculated with bootstrapped data to determine the statistical significance of the differences in FLUX and CTL variability. Unlike the traditional F-test (Wilks 2006), which only assesses changes in total variance, we can apply bootstrapping to the total, between-season, and within-season variances without

making assumptions about the shape of the data. Random data were generated using a bootstrapping algorithm that resampled the FLUX and CTL data 1000 times with replacement (Efron 1979). The changes in I, SST, and T variances were significant at $p = 0.05$ if the 95% confidence interval of the variance ratios calculated from the bootstrapped distributions excluded 1.

4.4 Results

4.4.1 Relationship Between the SAF and the Seasonal Cycle

Comparing the annual cycles of I, T, and SST averaged over the Barents Sea in CTL and FLUX reveals the effects of feedback suppression on interannual surface and atmospheric variability. The annual cycles of daily mean I clearly deviate more from the mean in CTL (Fig. 4.3a) than in FLUX (Fig. 4.3b), and the change in the total FLUX variance with respect to CTL is statistically significant. Changes in the interannual variance of I (Fig. 4.3c) are not significant because large differences in the FLUX and CTL variances only occur in November–January and April–June, which correspond to the onset of sea ice melting and freezing.

T is highly variable in CTL and FLUX from October through May (Fig. 4.3d, e), reflecting the seasonal increase synoptic-scale wave activity associated with the intensified North Atlantic storm track. T varies less in the summer when the Barents Sea is mostly ice-free and SSTs moderate the lower atmosphere. The change in the total variance of T is statistically significant, but the interannual variance of T is not statistically different in FLUX and CTL (Fig. 4.3f). However, variance is generally

lower in FLUX during the cold season when most of the Barents Sea is covered by ice, indicating that feedback suppression dampens the atmospheric variability.

SST also varies less in FLUX (Fig. 4.3h) than in CTL (Fig. 4.3g), and the total and interannual variances differs significantly. The greatest differences in the variance occur from July to September when most of the Barents Sea is coupled to the atmosphere (Fig. 4.3i). Since the ocean response lags atmospheric forcing by several months, and the SAF is only suppressed over grid boxes with nonzero ice cover, the lower SST variability in FLUX mainly reflects oceanic memory of the atmospheric forcing during the early winter when the Barents Sea is partially covered by ice.

4.4.2 Effects of Feedback Suppression on Total Variability

The annual cycle of I shown in Fig. 4.3a–c consists of two low-variance periods centered around the March maximum and September minimum I interspersed with two high-variance transitional periods of ice growth and melt. We identified the two high-variance and two low-variance seasons by calculating the variances of I (detrended, annual cycle removed as described in section 4.3) for CTL and FLUX over 90-day periods centered on every day of the year. We then selected the center days with the two largest and two smallest (nonconsecutive) differences in the FLUX and CTL seasonal variances. The first transition season spans mid-November–mid-February (NDJF) and is centered on the day with the largest difference in FLUX and CTL variance (Fig. 4.3c). NDJF is followed by the low-variance season cen-

tered around the time of maximum sea ice cover (mid-February–mid-May; FMAM), the second transition season (mid-May–mid-August; MJJA), and the second low-variance season centered around the time of minimum sea ice cover (mid-August–mid-November; ASON).

Figure 4.4 shows SS, SSB, and SSW for I, T, and SST in FLUX (green and pink stacked bars) and CTL (blue and yellow stacked bars) in each season. For I, SS is smaller in FLUX than in CTL in every season (Fig. 4.4a), and the greatest decreases occur during the NDJF and MJJA transition periods. Differences in CTL and FLUX SSB (blue and green) are larger than corresponding differences in SSW (yellow and pink), indicating that decreased between-season variability drives the reduction in total variability. Except for SSW in ASON, all differences in FLUX and CTL I variability are statistically significant.

Total SST variability is significantly lower in FLUX than in CTL in all seasons but FMAM (Fig. 4.4b) when, on average, extensive sea ice cover decouples the ocean from the atmosphere, and SSTs remain at or near freezing. Decreased between-season variability constitutes most of the change in total FLUX variability, while the within-season variability is only slightly reduced in NDJF and ASON and marginally increased in FMAM and MJJA due to the long memory of SST (note that increases in FMAM between- and within-season SST variability are marginally significant, but that SS values are not significant).

Except during MJJA, T variability decreases significantly in FLUX (Fig. 4.4c). As in I and SST, the change in between-season variability drives the change in total

variability, though significant reductions in SSB only occur in NDJF.

4.4.3 Effects of Feedback Suppression on Within-Season Variability

Assuming the behavior of I, T, and SST approximates a first-order autoregressive process, lagged correlations may be used to assess changes in within-season variability (memory of individual variables) and covariability (relationships between variables) (Box and Jenkins 1976). Feedback suppression tends to reduce the magnitude of the within-season I autocorrelation (Fig. 4.5). The autocorrelation also decays more rapidly in FLUX than in CTL, especially in NDJF. The contrast in the FLUX and CTL T autocorrelations is more pronounced (Fig. 4.6), with zero autocorrelation in FLUX after about 15 days in NDJF and FMAM when Barents Sea ice cover, and thus the climatological surface forcing, is greatest. Despite the large decay in the FLUX T autocorrelation, the I autocorrelation remains well above zero in FLUX throughout the year because of the stabilizing effect of the ocean evident in the nonzero SST autocorrelations (Fig. 4.7). Shutting off the sea ice-atmosphere feedback only affects the within-season SSTs in NDJF (Fig. 4.7a) when ice covers enough of the Barents Sea to induce strong climatological surface forcing but does not completely isolate the ocean from the atmosphere.

Lagged correlations between T and I (Fig. 4.8) are weaker and decay more quickly in FLUX than CTL. In addition, the peak magnitude of the correlation at lag of -2 days (T leads I) and faster decay rate of the FLUX correlation over positive lags (I leads T) compared to negative lags confirm that the atmosphere responds

to the climatological surface forcing rather than the real ice cover. In NDJF and FMAM (Fig. 4.8a, b), the FLUX correlation is nearly zero after about 10 days (I leads T), indicating that T is almost completely driven by climatological fluxes. FLUX correlations are above zero at all lags in MJJA and ASON (Fig. 4.8c, d) due to the combined effects of seasonally low ice cover and interaction between the atmosphere and ocean.

The lagged relationship between SST and T (Fig. 4.9) mirrors that of T and I, with lower and faster-decaying correlations in FLUX. As with I, T eventually decouples from SST in NDJF and FMAM (Fig. 4.9a, b), while SST depends on T throughout the year. SST and T are maximally correlated in ASON (Fig. 4.9d) beginning around lag 5 (T leads SST) when Barents Sea ice cover reaches a minimum.

I and SST are negatively correlated throughout the year at all lags as shown in Fig. 4.10. Pronounced reductions in the magnitudes of the FLUX correlations occur in NDJF (Fig. 4.10a), while the magnitudes are slightly greater in FLUX than CTL in FMAM and ASON (Fig. 4.10b, d). The increased correlation between SST and I in FMAM reflects the oceanic memory of the relatively strong climatological atmospheric forcing in NDJF, and the fact that sea ice cover reaches a maximum so that more ice is available to "feel" the stabilizing effects of the atmosphere and the sea ice; in other words, anomalously high sea ice fraction is forced toward climatology by atmosphere and the ocean, increasing the statistical relationship between I and SST. In ASON, the increased correlation between SST and I in FLUX mainly reflects oceanic memory of the atmospheric forcing in MJJA since only the northernmost

portion of the Barents Sea is covered by ice, and climatological atmospheric forcing is minimized.

4.5 Discussion and Conclusions

Suppressing the sea ice-atmosphere feedback in a coupled climate model by forcing the atmosphere with surface turbulent and longwave heat fluxes and temperatures weighted by climatological sea ice fraction dampens the surface and atmospheric variability. Reductions in the between-season variability of I, T, and SST averaged over the Barents Sea constitute most of the change in total variability, while oceanic effects moderate changes in the within-season variability. The decrease in the variability of I in response to the climatologically forced atmosphere suggests that the local sea ice-atmosphere feedback is positive, in agreement with the results in previous work that showed the sea ice-atmosphere feedback over the Barents Sea in an uncoupled model was positive and thermodynamically driven (Liptak and Strong 2014a).

The localized positive sea ice-atmosphere feedback contrasts the dynamically driven negative sea ice-atmosphere feedback proposed in other modeling studies. Magnusdottir et al. (2004), Alexander et al. (2004), Yamamoto et al. (2006), and Liptak and Strong (2014b) forced a global climate model with prescribed sea ice anomalies during the cold season and found very different atmospheric responses. Magnusdottir et al. (2004) found that forcing the atmosphere with large negative sea ice concentration anomalies generated a strong response resembling the negative phase of the NAO. Yamamoto et al. (2006) used positive and negative phases of

the leading pattern of variability in sea ice concentration as boundary conditions and showed that the differences in 500-mb height responses resembled the NAO. Alexander et al. (2004) forced the atmosphere with sea ice extent and concentration conditions derived from observations during years with high and low sea ice cover over the Arctic that also produced negative NAO-like patterns when sea ice cover was reduced in the Barents Sea region. Given the spatial heterogeneity in the signs of the sea ice anomalies, the atmospheric patterns were weaker than in Magnusdottir et al. (2004) and Yamamoto et al. (2006). Liptak and Strong (2014b) showed that the large-scale atmospheric responses to positive and negative sea ice concentration anomalies over the Barents Sea both resembled the negative phase of the NAO. However, the responses of the surface turbulent heat fluxes and wind stress were opposite-signed and confined to the Barents Sea. Overall, the aforementioned studies illustrate that the magnitude and duration of the atmospheric response to sea ice anomalies in uncoupled boundary forcing experiments partly depends on the size of the forcing, in agreement with Deser et al. (2004),

We took the additional step of forcing the sea ice over the Barents Sea with atmospheric conditions produced by the positive and negative sea ice anomalies in Liptak and Strong (2014b) and found that that downwelling radiation anomalies produced a positive feedback of the atmosphere onto the sea ice. In summary, forcing the atmosphere with anomalously high and low sea ice cover in an uncoupled model produced opposite-signed surface turbulent heat flux anomalies that continually warmed or cooled the near-surface atmosphere. Since SSTs were held constant, the

portion of the atmospheric heating anomaly that was not removed by advection went directly into the sea ice via longwave fluxes so that a cold atmosphere produced by anomalously high sea ice cover favored additional ice growth and a warm atmosphere produced by anomalously low sea ice cover enhanced sea ice melt.

While our results demonstrate that experimental design can greatly constrain the atmospheric responses to surface boundary forcing and that one cannot assume the sign of the sea ice-atmosphere feedback by examining only one part of the feedback loop, they do not suggest that uncoupled experiments are invaluable for studying feedback processes. Rather, coupled modeling experiments help verify the behavior of feedbacks isolated in uncoupled models. Thus, we confirm the existence of a local positive sea ice-atmosphere feedback over the Barents Sea in a more realistic coupled modeling framework and conclude that the ocean acts to moderate the feedback.

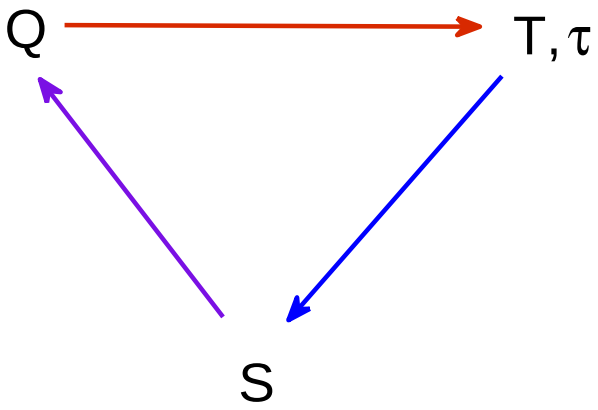

Fig. 4.1. Conceptual model of a sea ice-atmosphere feedback (SAF) in which a sea ice anomaly (S) leads to vertical sensible, latent, and longwave heat fluxes (Q), resulting in near-surface air temperature (T) and wind stress (τ) anomalies that create a new sea ice configuration.

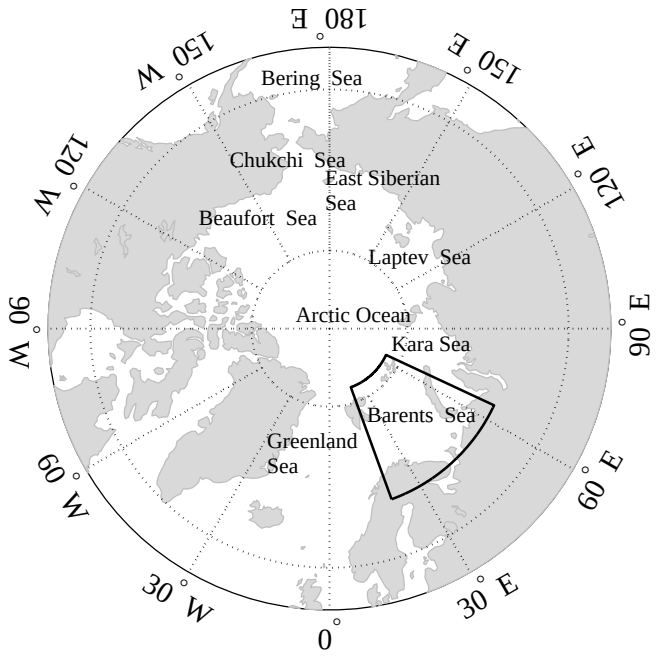

Fig. 4.2. Map of the Arctic. Black contour outlines the analysis domain.

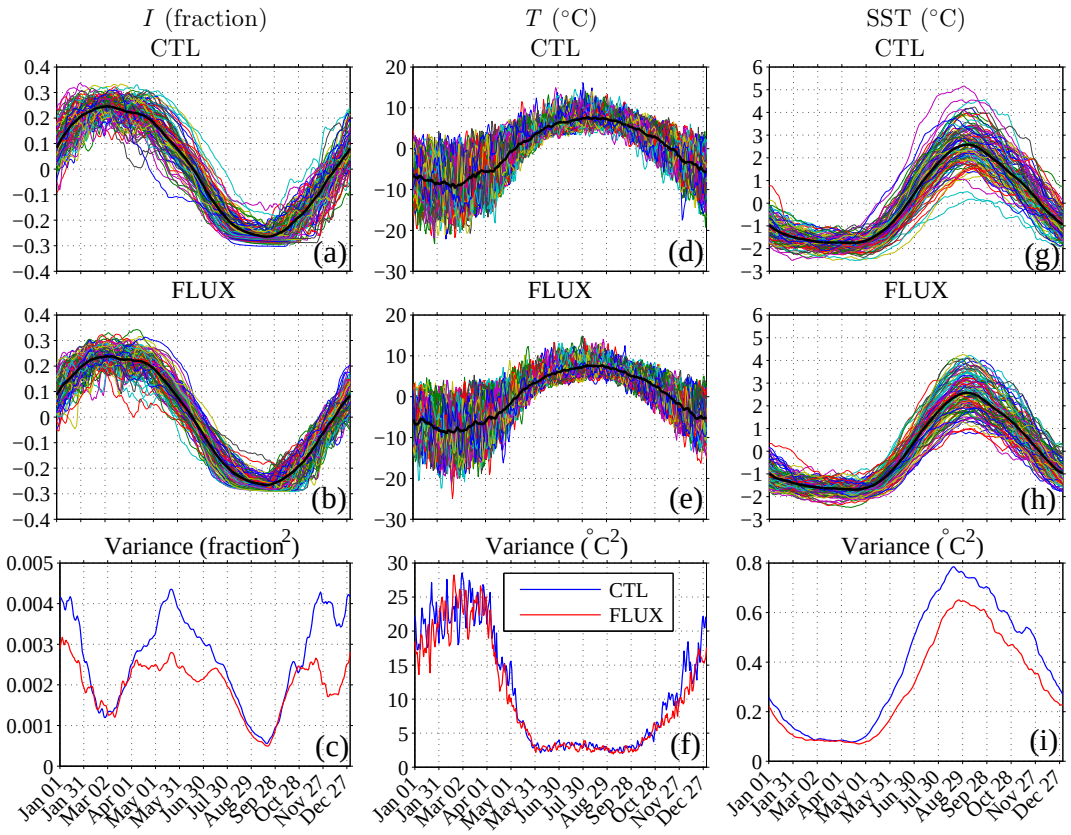

Fig. 4.3. Annual cycles and between-season variance of daily CTL and FLUX variables. Annual cycles of I for (a) CTL and (b) FLUX. Annual cycles of T for (d) CTL and (e) FLUX. Annual cycles of SST for (g) CTL and (h) FLUX. Thick black contours are the long-term daily means. Between-season variance of (c) I, (f) T, and (i) SST in CTL (blue contours) and FLUX (red contours).

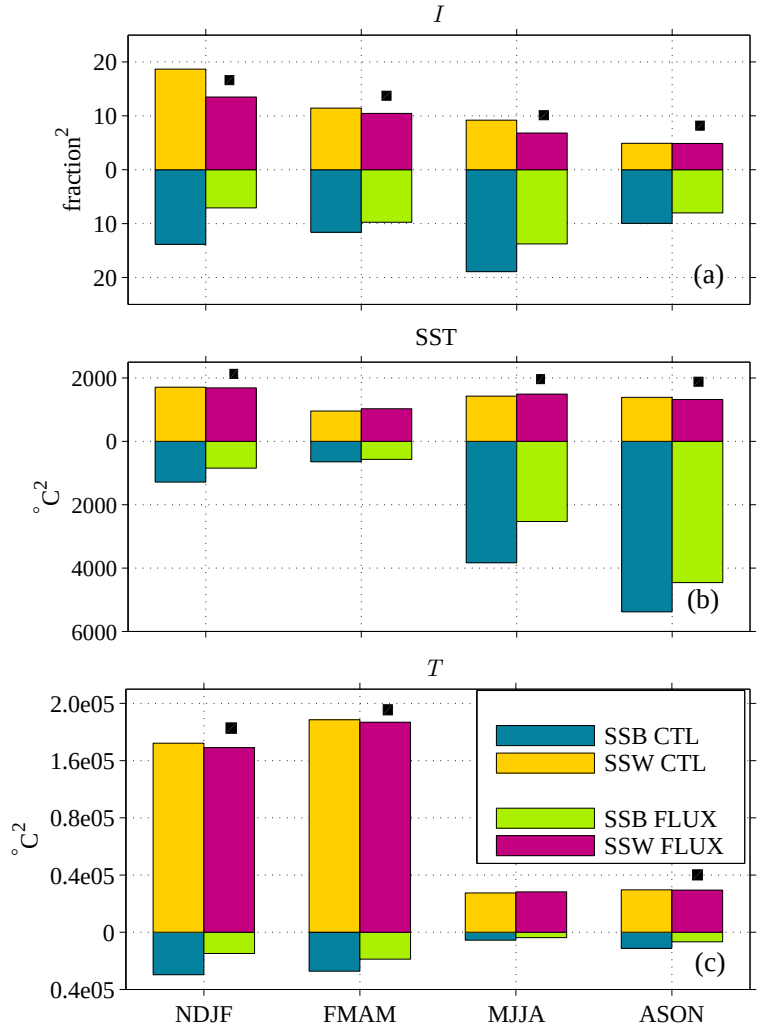

Fig. 4.4. CTL and FLUX between-season (SSB, blue and green segments) and within-season (SSW, yellow and pink segments) sum of squares for (a) I, (c), SST, and (c) T. Note that the y-axis is positive in both directions, and the full length of each bar (SSB+SSW) is the total sum of squares (SS). Black squares above the pink and green bars indicate statistically significant changes in SS at $p = 0.05$.

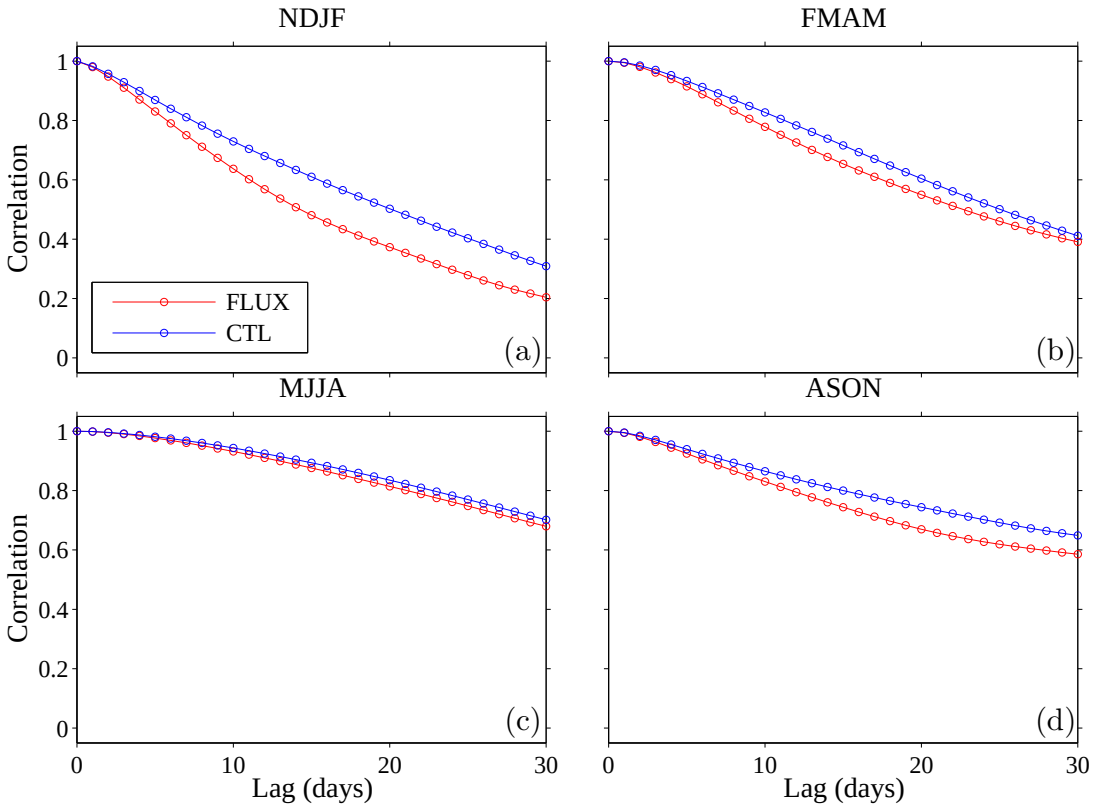

Fig. 4.5. Within-season autocorrelations for FLUX (red circles) and CTL (blue circles) I for (a) NDJF, (b) FMAM, (c) MJJA, and (d) ASON.

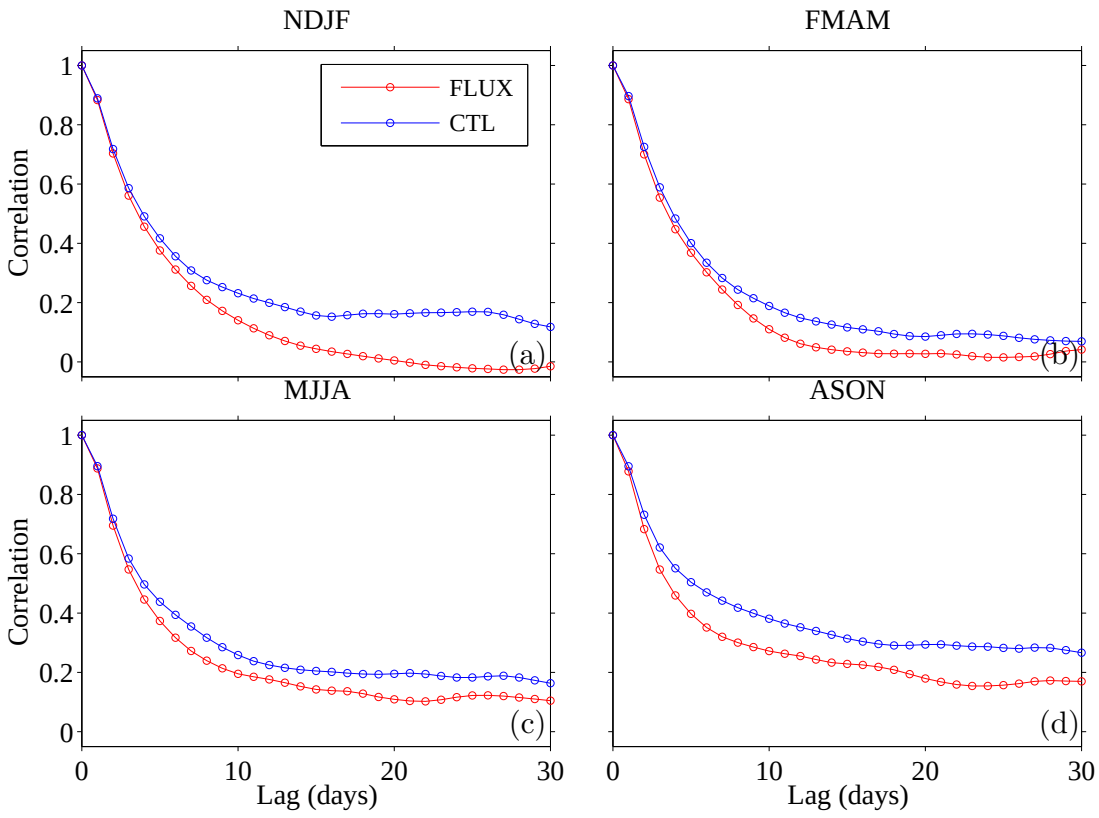

Fig. 4.6. As in Fig. 4.5 but for T.

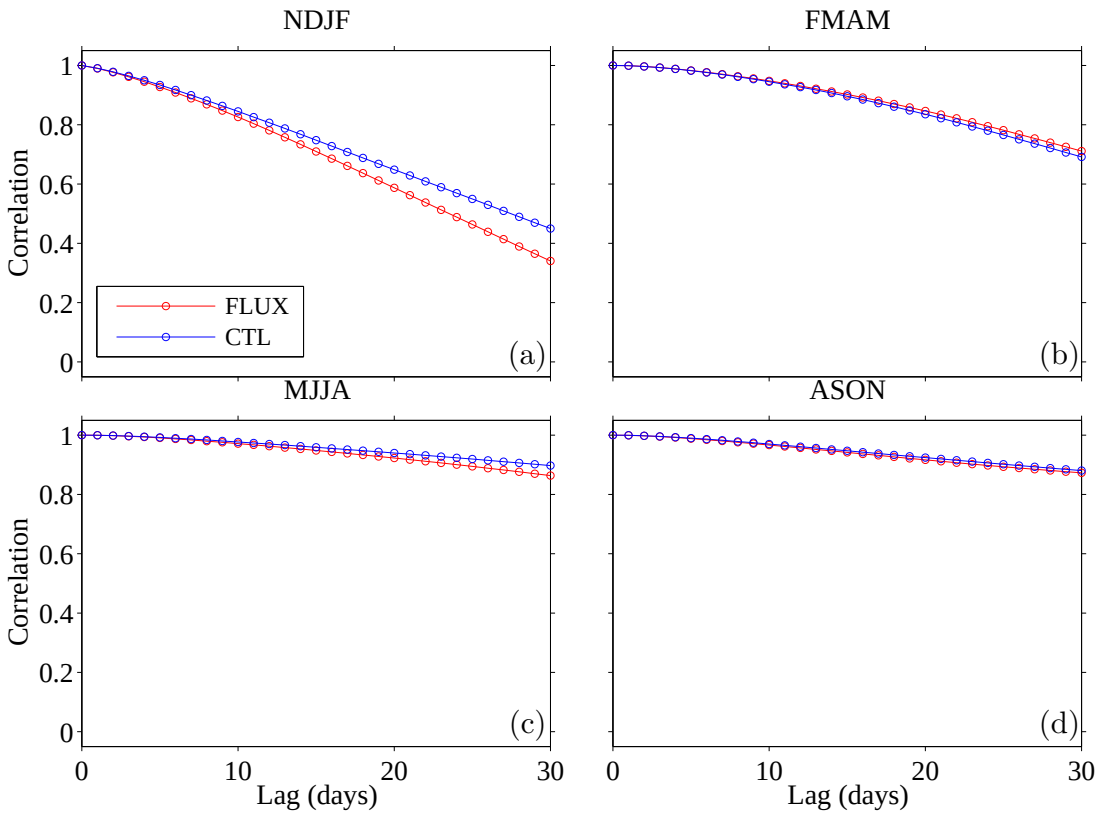

Fig. 4.7. As in Fig. 4.5 but for SST.

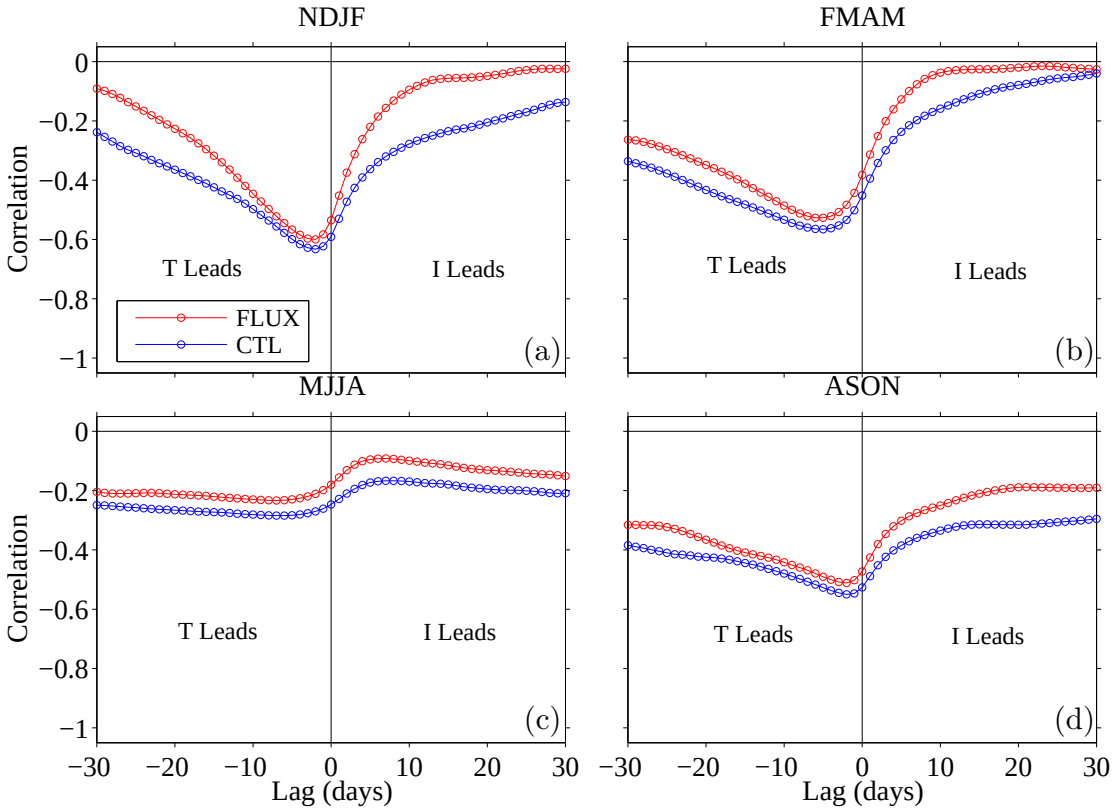

Fig. 4.8. Within-season I and T lagged correlations for FLUX (red circles) and CTL (blue circles) for (a) NDJF, (b) FMAM, (c) MJJA, and (d) ASON

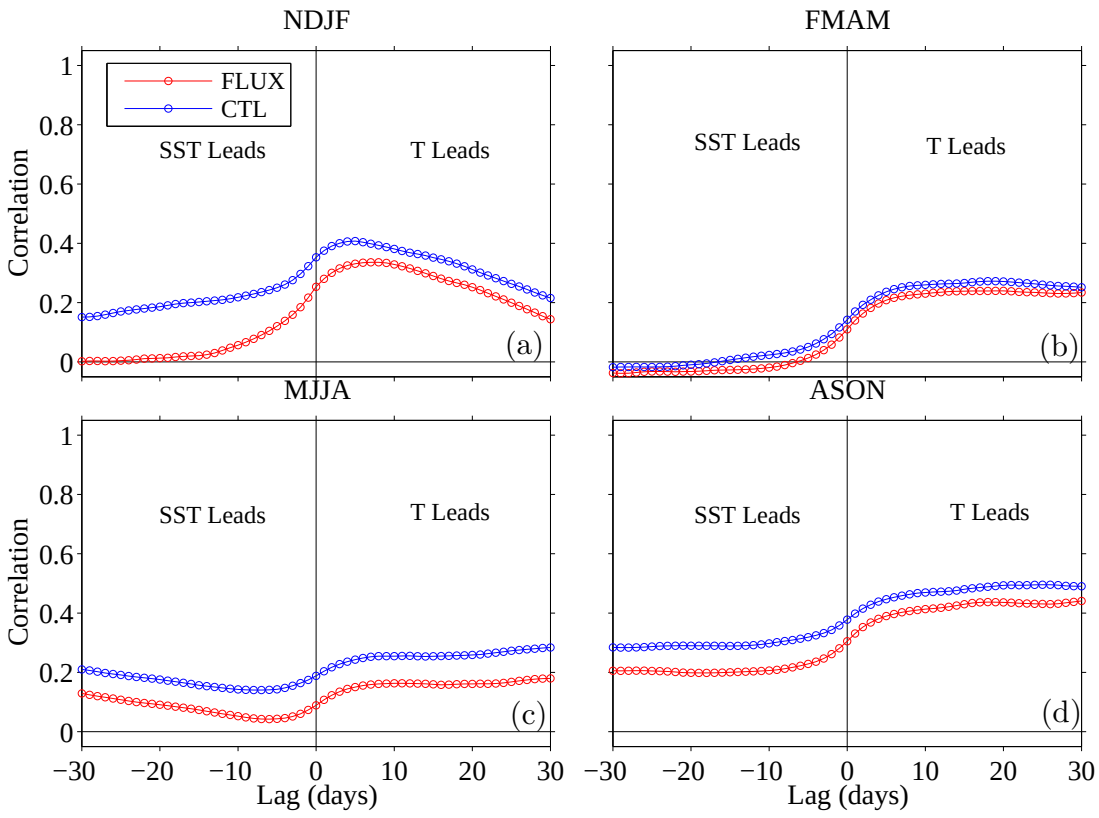

Fig. 4.9. As in Fig. 4.8 but for SST and T.

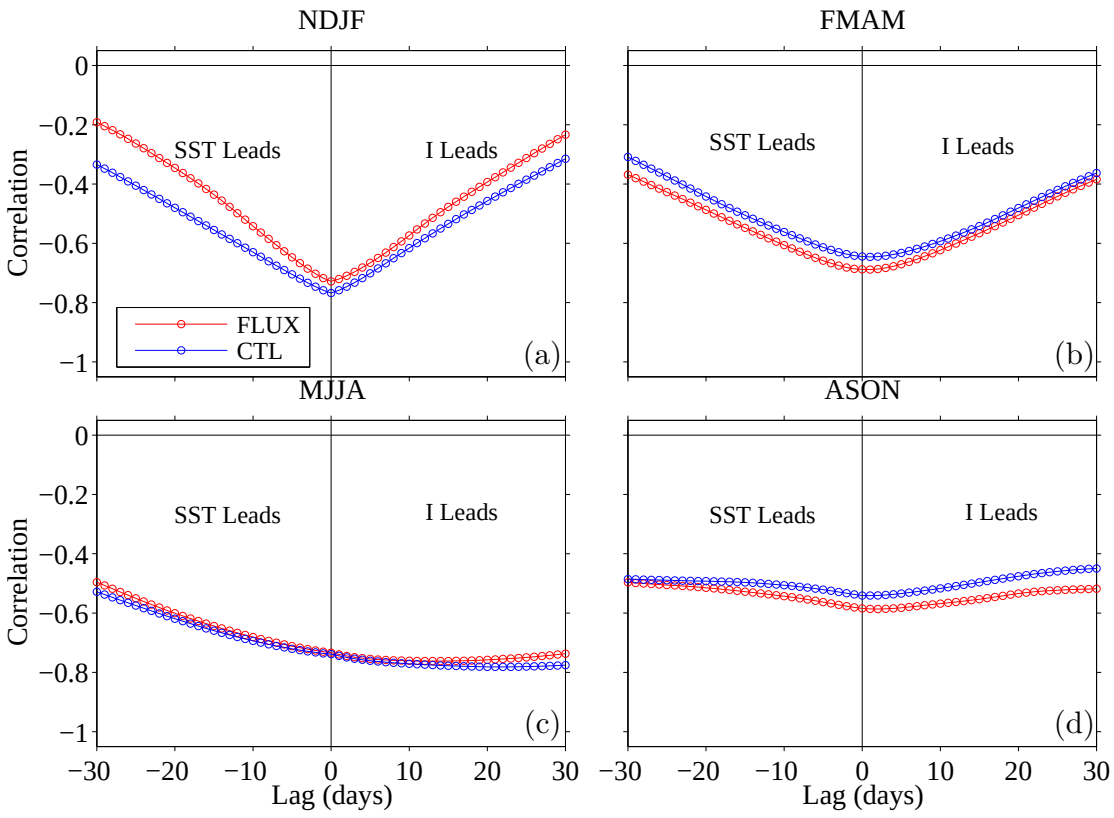

Fig. 4.10. As in Fig. 4.8 but for I and SST.

4.6 References

Abbot, D. S., C. C. Walker, and E. Tziperman, 2009: Can a convective cloud feedback help to eliminate winter sea ice at high CO2 concentrations? *J. Climate*, **22** (21), 5719–5731, doi:10.1175/2009JCLI2854.1.

Alexander, M. A., U. S. Bhatt, J. E. Walsh, M. S. Timlin, J. S. Miller, and J. D. Scott, 2004: The atmospheric response to realistic Arctic sea ice anomalies in an AGCM during winter. *J. Climate*, **17**, 890–905.

Bailey, D., C. Hannay, M. Holland, and R. Neale, 2013: Slab ocean model forcing. National Center for Atmospheric Research, Boulder, CO. http://www.cesm.ucar.edu/models/cesm1.1/data8/doc/som.pdf, 2 pp.

Bitz, C. M., K. M. Shell, P. R. Gent, D. Bailey, G. Danabasoglu, K. C. Armour, M. M. Holland, and J. T. Kiehl, 2012: Climate sensitivity of the Community Climate System Model Version 4. *J. Climate*, **25**, 3053–3070, doi:10.1175/JCLI-D-11-00290.1.

Boé, J., A. Hall, and X. Qu, 2009: Current GCMs' unrealistic negative feedback in the Arctic. *J. Climate*, **22**, 4682–4695, doi:10.1175/2009JCLI2885.1.

Bony, S. et al., 2006: How well do we understand and evaluate climate change feedback processes? *J. Climate*, **19**, 3445–3482.

Box, G., and G. Jenkins, 1976: *Time Series Analysis: Forecasting and Control*. Holden-Day, 575 pp.

Curry, J. A., J. L. Schramm, and E. E. Ebert, 1995a: Sea ice-albedo climate feedback mechanism. *J. Climate*, **8**, 240–247.

Curry, J. A., J. L. Schramm, M. C. Serreze, and E. E. Ebert, 1995b: Water vapor feedback over the Arctic Ocean. *J. Geophys. Res.*, **100**, 14 223–14 229, doi:10.1029/95JD00824.

Deser, C., G. Magnusdottir, R. Saravanan, and A. S. Phillips, 2004: The effects of North Atlantic SST and sea-ice anomalies on the winter circulation in CCM3. Part II: Direct and indirect components of the response. *J. Climate*, **17**, 877–889, doi:10.1175/1520-0442(2004)017$\langle$\$0877:TEONAS\$$\rangle$\$2.0.CO;2.

Deser, C., J. E. Walsh, and M. S. Timlin, 2000: Arctic sea ice variability in the context of recent atmospheric circulation trends. *J. Climate*, **13**, 617–633.

Efron, B., 1979: Bootstrap methods: Another look at the jackknife. *Ann. Stat.*, **7**, 1–26.

Frankignoul, C., N. Sennéchael, and P. Cauchy, 2014: Observed atmospheric response to cold season sea ice variability in the Arctic. *J. Climate*, **27**, 1243–1254, doi:10.1175/JCLI-D-13-00189.1.

Gent, P. R. et al., 2011: The Community Climate System Model version 4. *J. Climate*, **24**, 4973–4991, doi:10.1175/2011JCLI4083.1.

Hunke, E. C., and W. H. Lipscomb, 2008: CICE: The Los Alamos sea ice model user's manual, version 4. Tech. Rep. LA-CC-06-012, Los Alamos National Laboratory.

Intrieri, J. M., C. W. Fairall, M. D. Shupe, P. O. G. Persson, E. L. Andreas, P. S. Guest, and R. E. Moritz, 2002: An annual cycle of Arctic surface cloud forcing at SHEBA. *J. Geophys. Res.*, **107**, 8039, doi:10.1029/2000JC000439.

Jung, T., and M. Hilmer, 2001: The link between the North Atlantic Oscillation and Arctic sea ice export through Fram Strait. *J. Climate*, **14**, 3932–3943.

Kauffman, B. G., R. Jacob, T. Craig., and W. G. Large, 2004: The CCSM coupler Version 6.0 User's guide, source code reference, and scientific description. 62 pp.

Kwok, R., G. F. Cunningham, and S. S. Pang, 2004: Fram Strait sea ice outflow. *J. Geophys. Res.*, **109** (C1), C01 009, doi:10.1029/2003JC001785.

Kwok, R., G. F. Cunningham, M. Wensnahan, I. Rigor, H. J. Zwally, and D. Yi, 2009: Thinning and volume loss of the Arctic Ocean sea ice cover. *J. Geophys. Res*, **114**, doi:10.1029/2009JC005312.

Liptak, J., and C. Strong, 2014a: A model-based decomposition of the sea ice-atmosphere feedback over the Barents Sea during winter. *J. Climate*, **27**, 2533–2544, doi:10.1175/JCLI-D-13-00371.1.

Liptak, J., and C. Strong, 2014b: The winter atmospheric response to sea ice anomalies in the Barents Sea. *J. Climate*, **27**, 914–924, doi:10.1175/JCLI-D-13-00186.1.

Liu, Y., and J. R. Key, 2014: Less winter cloud aids summer 2013 Arctic sea ice return from 2012 minimum. *Environ. Res. Lett*, **9**, 044 002, doi:10.1088/1748-9326/9/4/044002.

Magnusdottir, G., C. Deser, and R. Saravanan, 2004: The effects of North Atlantic SST and sea ice anomalies on the winter circulation in CCM3. Part I: Main features and storm track characteristics of the response. *J. Climate*, **17**, 857–876, doi:10.1175/1520-0442(2004)017$⟨$0857:TEONAS$⟩$2.0.CO;2.

Maslanik, J., S. Drobot, C. Fowler, W. Emery, and R. Barry, 2007a: On the Arctic climate paradox and the continuing role of atmospheric circulation in affecting sea ice conditions. *Geophys. Res. Lett.*, **34**, doi:10.1029/2006GL028269.

Maslanik, J., S. Drobot, C. Fowler, W. Emery, and R. Barry, 2007b: A younger, thinner Arctic ice cover: Increased potential for rapid, extensive sea-ice loss. *Geophys. Res. Lett.*, **34**, doi:10.1029/2007GL032043.

Neale, R. B. et al., 2010: Description of the NCAR Community Atmosphere Model (CAM 4.0). Tech. Rep. NCAR/TN-485+STR, National Center For Atmospheric Research, Boulder, CO, USA.

Nghiem, S. V., I. G. Rigor, D. K. Perovich, P. Clemente-Colón, J. W. Weatherly, and G. Neumann, 2007: Rapid reduction of Arctic perennial sea ice. *Geophys. Res. Lett.*, **34** (19), doi:10.1029/2007GL031138.

Parkinson, C. L., and D. J. Cavalieri, 2008: Arctic sea ice variability and trends, 1979–2006. *J. Geophys. Res.*, **113**, C07 003, doi:10.1029/2007JC004558.

Perovich, D. K., and J. A. Richter-Menge, 2009: Loss of sea ice in the Arctic. *Annu. Rev. Marine. Sci.*, **1**, 417–441, doi:10.1146/annurev.marine.010908.163805.

Pithan, F., and T. Mauritsen, 2014: Arctic amplification dominated by temperature feedbacks in contemporary climate models. *Nature Geosci.*, **advance online publication**, doi:10.1038/ngeo2071.

Rigor, I. G., and J. M. Wallace, 2004: Variations in the age of Arctic sea-ice and summer sea-ice extent. *Geophys. Res. Lett.*, **31**, L09 401, doi:10.1029/2004GL019492.

Serreze, M. C., M. M. Holland, and J. Stroeve, 2007: Perspectives on the Arctic's shrinking sea-ice cover. *Science*, **315**, 1533–1536.

Smedsrud, L. H., A. Sirevaag, K. Kloster, A. Sorteberg, and S. Sandven, 2011: Recent wind driven high sea ice export in the Fram Strait contributes to Arctic sea ice decline. *The Cryosphere Discuss.*, **5**, 1311–1334.

Stroeve, J. C., T. Markus, L. Boisvert, J. Miller, and A. Barrett, 2014: Changes in Arctic melt season and implications for sea ice loss. *Geophys. Res. Lett.*, **41**, 2013GL058 951, doi:10.1002/2013GL058951.

Strong, C., and G. Magnusdottir, 2010: Dependence of NAO variability on coupling with sea ice. *Climate Dyn.*, **36**, 1681–1689, doi:10.1007/s00382-010-0752-z.

Strong, C., G. Magnusdottir, and H. Stern, 2009: Observed feedback between winter sea ice and the North Atlantic Oscillation. *J. Climate*, **22**, 6021–6032.

Tsukernik, M., C. Deser, M. Alexander, and R. Tomas, 2010: Atmospheric forcing of Fram Strait sea ice export: A closer look. *Climate Dyn.*, **35**, 1349–1360.

Ukita, J., M. Honda, H. Nakamura, Y. Tachibana, D. J. Cavlieri, C. L. Parkinson, H. Koide, and K. Yamamoto, 2007: Northern Hemisphere sea ice variability: Lag structure and its implications. *Tellus, Ser. A*, **59**, 261–272, doi:10.111/j.1600-0870.2006.0223.x.

Vinje, T., 2001: Anomalies and trends in sea-ice extent and atmospheric circulation in the Nordic Seas during the period 1864–1998. *J. Climate*, **14**, 3503–3517.

Wilks, D. S., 2006: *Statistical methods in the atmospheric sciences*. 2d ed., Elsevier Inc., California, 627 pp.

Wu, B., J. Wang, and J. E. Walsh, 2006: Dipole anomaly in the winter Arctic atmosphere and its association with sea ice motion. *J. Climate*, **19** (2), 210–225, doi:10.1175/JCLI3619.1.

Yamamoto, K., Y. Tachibana, M. Honda, and J. Ukita, 2006: Intra-seasonal relationship between the Northern Hemisphere sea ice variability and the North Atlantic Oscillation. *Geophys. Res. Lett.*, **33**, L14 711, doi:10.1029/2006GL026286.

CHAPTER 5

PROPAGATING ATMOSPHERIC PATTERNS ASSOCIATED WITH SEA ICE MOTION THROUGH THE FRAM STRAIT[1]

5.1 Abstract

A novel analysis method involving phase-shifted complex Hilbert empirical orthogonal function (HEOFs) was used to examine how variations in predominant propagating patterns of Arctic surface wind influence daily Fram Strait sea ice export (F) during extended winter (October–April) – a primary control on Arctic sea ice volume. Northwesterly winds favorable to F were provided by poleward-moving anticyclones upstream over the Canadian Arctic associated with the leading HEOF of wind and also by eastward-moving cyclones downstream over the Barents Sea associated with the second HEOF of wind. A suite of spatial and statistical analyses indicated that the aggregate of the two propagating patterns largely explains a sea level pressure pattern analyzed in several prior studies as a standing wave oriented

[1]Liptak, Jessica, Courtenay Strong, 2013: Propagating Atmospheric Patterns Associated with Sea Ice Motion through the Fram Strait, *J. Climate*, **26**, 2992–2997, 10.1175/JCLI-D-12-00599.1. ©American Meteorological Society. Used with permission.

east-west across the Strait.

5.2 Introduction

The Fram Strait is the primary conduit of sea ice export in the Arctic. Ice motion associated with Arctic ice export depends largely on atmospheric forcing, which is often measured in terms of storm tracks and standing-wave teleconnections such as the North Atlantic Oscillation (NAO). The NAO is typically defined as the first empirical orthogonal function (EOF) of sea level pressure (SLP) over the north Atlantic (Hurrell et al. 2003). The positive phase of the NAO, characterized by an anomalously strong Icelandic Low, is associated with enhanced ice export through the Fram Strait during the winter (Kwok and Rothrock 1999; Kwok et al. 2004; Kwok 2009). Hilmer and Jung (2000) found that the correlation between the NAO and sea ice motion was positive and stronger in decades following the late 1970s when the Icelandic Low shifted eastward relative to its mean position in 1958–1977, resulting in enhanced northerly winds over the Fram Strait. Similar inconsistencies in the temporal correlation between winter Fram Strait sea ice flux and the NAO were noted by Vinje (2001).

Other modes of atmospheric variability influence Fram Strait sea ice flux. The "Barents Oscillation" (Skeie 2000; Tremblay 2001) appeared as the second (Skeie 2000) or third EOF (Tremblay 2001) of winter (December–March) SLP north of 25°–30°N depending on the analysis period used and depicted northerly geostrophic flow through the Fram Strait in its positive polarity. Tsukernik et al. (2010) showed

that daily Fram Strait sea ice flux during the winter and summer was correlated with an index of the cross-strait pressure gradient based on a dipole in the SLP anomaly field that resembled the Barents Oscillation. Wu et al. (2006) and Wang et al. (2009) termed the pattern in the second EOF of SLP north of 70°N the Dipole Anomaly. The positive phase of the Dipole Anomaly depicted enhanced cyclonic circulation over the Barents Sea and was associated with southward Fram Strait sea ice flux.

The gradient associated with SLP anomalies determines surface wind stress, which acts with the Coriolis force, internal ice stress, and ocean stress to determine the motion of low-concentration ice present in the Fram Strait. A discussion of the importance and dynamical interpretation of Ekman drift of ice is given in Ogi et al. (2008). Provided that sea ice is sufficiently far from land, on average the ice moves approximately 30° to the right of the of the surface wind as observed by Nansen (1902) and Zubov (1943), implying that sea ice motion is roughly parallel to surface isobars. Model results from Koenigk et al. (2006) showed that annual ice export through the Fram Strait was primarily driven by the cross-strait SLP gradient. Vihma et al. (2012) found that a greater portion of the variance in annual mean Arctic ice drift speed was explained by the difference in SLP between 270°E and 90°E at 84°N than by the Dipole Anomaly in Wu et al. (2006). Furthermore, annual and fall (September–November) mean ice drift speeds in the Fram Strait were determined by the SLP difference at 82°N.

On time scales of 1 to 2 weeks, the passage of cyclones strongly influences Fram Strait sea ice export. Brümmer et al. (2003) observed an increase in the average

ice drift speed from approximately 0.2 m s^{-1} to 0.6 m s^{-1} during the passage of a cyclone. In addition, the location of a cyclone relative to the Fram Strait played a major role in determining the direction of ice motion and amount of convergence. Rogers et al. (2005) found that decreased Fram Strait sea ice export was associated with increased winter cyclone frequency in the Fram Strait and decreased cyclone frequency over the Norwegian and Barents seas.

Here, a novel analysis method involving phase-shifted complex Hilbert empirical orthogonal functions was used to examine how variations in predominant propagating patterns of Arctic surface wind during extended winter (October–April) influence daily Fram Strait sea ice export. By using circulation patterns that are both propagating and of leading statistical importance, this analysis method incorporates strengths of storm track and EOF analyses.

5.3 Data and Methods

Following Tsukernik et al. (2010), sea ice motion vectors obtained from the National Snow and Ice Data Center (Fowler 2003) were used to compute an index (F) of daily sea ice motion through the Fram Strait during winter (defined as 15 October–14 April) over the period 1979–2006. F was the meridional component of sea ice motion averaged over the region 20°W–15°E, 79°N–81°N (Fig. 5.1, red box), with positive F indicating southward sea ice motion (export).

Complex Hilbert empirical orthogonal function (HEOF) analysis (e.g., Hannachi et al. 2007) was performed on the combined field of the zonal and meridional compo-

nents of daily surface wind ($\vec{v}$) from 60°N–90°N obtained from the NCEP-NCAR Reanalysis (Kalnay et al. 1996). The phase of each HEOF was shifted by the angle ϕ that maximized the temporal correlation between F and the real part of the principal component (i.e., time series) associated with each HEOF. As shown in Strong and Liptak (2012), the desired phase shift ϕ is the argument of the complex correlation between F and the HEOF time series, and application of the phase shift facilitates presentation of the HEOF pattern by consolidating the statistically relevant information entirely in the real domain; thus, the HEOF is set in the phase most relevant to the geographically fixed variations of interest (F in this case).

Here, we present the first two phase-shifted HEOFs of $\vec{v}$ ($H_{\vec{v}1}$ and $H_{\vec{v}2}$). We refer to their eigenvectors as $H_{\vec{v}1}$ and $H_{\vec{v}2}$ "patterns" and their principal components as $H_{\vec{v}1}$ and $H_{\vec{v}2}$ "time series" where needed for clarity. Further details on the rationale, derivation, and utility of the phase shift are given in Strong and Liptak (2012).

To interpret the results of the HEOF analysis in the context of prior work on SLP standing waves, traditional EOF analysis was performed on daily winter SLP data from the NCEP-NCAR Reanalysis over the north Atlantic region, defined as 90°W–90°E, 45°N–90°N. The first EOF (E_{p1}) represented the NAO (Hurrell et al. 2003), and accounted for 29% of the SLP variance. Attention here focused on the second EOF (E_{p2}), which accounted for 13% of the variance and was also well-separated according to the criterion of North et al. (1982).

To estimate the power spectrum of a principal component, power spectra were calculated for each winter using Hanning windows, and then the spectra were averaged

(Welch 1967). Red noise spectra and associated 95% confidence limits were calculated according to the method outlined by Gilman et al. (1963). Reported correlations were tested for statistical significance at the 95% confidence level by bootstrapping the distribution of the Pearson correlation coefficient (r) by resampling with replacement 1,000 times (e.g., Efron 1979).

5.4 Results

The vector correlation between the surface wind velocity and F (Fig. 5.1) shows that Fram Strait sea ice flux is associated with a cyclonic circulation over the Barents Sea and an anticyclonic circulation located off of northwestern Greenland. Assuming that the interaction of ocean stress, internal ice stress, and the Coriolis force produces sea ice motion that is oriented approximately 30° to the right of the surface flow (Nansen 1902; Zubov 1943), the northwesterly winds over the Fram Strait are conducive to sea ice export (defined by large positive values of F).

$H_{\vec{v}1}$ and $H_{\vec{v}2}$ together account for 25% of the variance in the surface wind field and were well-separated according to the criteria of North et al. (1982). The real part of the $H_{\vec{v}1}$ pattern (Fig. 5.2a) depicts northwesterly flow through the Fram Strait between an upstream anticyclonic circulation (filled blue circle) and downstream cyclonic circulation (filled red circle), and the correlation between the $H_{\vec{v}1}$ time series and F is $r = 0.27$. The median temporal rate of change of the angle of the $H_{\vec{v}1}$ time series is positive, meaning that the $H_{\vec{v}1}$ transients tende to propagate toward increasing phase along a transpolar trajectory from North America toward Asia (open

symbols, Fig. 5.2a). The imaginary part of the $H_{\vec{v}1}$ pattern (Fig. 5.2b) is the real part shifted by $\pi/2$, and the associated northeasterly flow over the Strait (arrows, Fig. 5.2b) is conducive to westward sea ice motion, yielding zero correlation with F.

The real part of the $H_{\vec{v}2}$ pattern (Fig. 5.2c) also depicts an upstream anticyclone (filled blue circle) and downstream cyclone (filled red circle), and the correlation between the $H_{\vec{v}2}$ time series and F is $r = 0.30$. The median temporal rate of change of the $H_{\vec{v}2}$ time series is positive, meaning that $H_{\vec{v}2}$ captures eastward-moving transients over the subpolar Atlantic seas and the Canadian Arctic (open symbols, Fig. 5.2c). As with $H_{\vec{v}1}$, the imaginary part of $H_{\vec{v}2}$ (Fig. 5.2d) advances the circulation features $\pi/2$ downstream to positions where they have zero correlation with F.

Mapped inspection and statistical analysis of $H_{\vec{v}1}$ and $H_{\vec{v}2}$ suggests that these two patterns combine to form the standing wave east-west SLP dipole pattern linked to F in several prior studies. The east-west dipole appears as the second EOF of SLP over the north Atlantic domain (E_{p2}, Section 5.3) and is nearly identical (Fig. 5.3) to the one presented in Fig. 2 of Tsukernik et al. (2010). The E_{p2} pattern is also similar to the Dipole Anomaly (Wu et al. 2006; Wang et al. 2009) and the Barents Oscillation (Skeie 2000; Tremblay 2001), although the latter two use different analysis domains and time periods. The correlation between F and E_{p2} is $r = 0.39$ and reflects southward ice motion driven by the northerly flow indicated by north-south orientation of the isobars over the Fram Strait. Notably, the anticyclonic circulation center in $H_{\vec{v}1}$ is collocated with the E_{p2} positive center of action, and the cyclonic circulation center in $H_{\vec{v}2}$ is collocated with the E_{p2} negative center of action. The E_{p2}

time series is correlated with the real parts of $H_{\vec{v}1}$ and $H_{\vec{v}2}$ at $r = 0.25$ and $r = 0.41$, respectively. E_{p1} (the NAO), by contrast, is correlated with $H_{\vec{v}1}$ at $r = 0.02$ (not significant) and $H_{\vec{v}2}$ at $r = 0.04$ (significant).

Providing further evidence of the strong linkage from $H_{\vec{v}1}$ and $H_{\vec{v}2}$ to E_{p2}, the temporal power spectra of these patterns are remarkably similar (Fig. 5.4). Each spectrum differs significantly from a null red noise spectrum for periods between 4 and 15 days (dashed vertical lines, Fig. 5.4). Peaks occurr at periods of 13 days for $H_{\vec{v}1}$ (Fig. 5.4a), 14 days for $H_{\vec{v}2}$ (Fig. 5.4b), and 13 days for E_{p2} (Fig. 5.4c).

5.5 Summary and Conclusions

Complex HEOF analysis was used to identify the leading two patterns of variability in the surface wind field poleward of 60°N during winter ($H_{\vec{v}1}$ and $H_{\vec{v}2}$). The HEOFs were then phase-shifted to optimize the real correlation between the associated principal component time series and an index of Fram Strait sea ice export F, revealing that each pattern supports northwesterly flow over the Fram Strait. $H_{\vec{v}1}$ depicts synoptic-scale cyclones and anticyclones that followed a transpolar track from the Canadian Arctic to Siberia, and the correlation with F is $r = 0.27$. The $H_{\vec{v}1}$ pattern is consistent with the tendency for Arctic cyclones to travel eastward or poleward from the Canadian Archipelago, Greenland Sea, Barents Sea, and Kara Sea over the eastern Arctic and, to a lesser extent, the Chukchi and East Siberian Seas in the western Arctic in the winter (Serreze et al. 1993; Brümmer et al. 2000; Sickmöller et al. 2000; Zhang et al. 2004; Sorteberg and Kvingedal 2006). Thus, $H_{\vec{v}1}$ captures

the variability associated with propagating synoptic-scale cyclones that cross into the high latitudes, not a transpolar storm track per se. $H_{\vec{v}2}$ resolves eastward-moving circulations over the subpolar Atlantic and Canadian Arctic consistent with patterns observed in several storm track analyses (e.g., Brümmer et al. 2000; Sickmöller et al. 2000; Sorteberg and Kvingedal 2006), and its correlation with F is $r = 0.30$.

Centers of action in the SLP standing wave dipole associated with F in prior work [i.e., the second EOF of north Atlantic SLP (E_{p2})] align remarkably well with the real parts of the $H_{\vec{v}1}$ and $H_{\vec{v}2}$ spatial patterns after phase shifting. Specifically, the positive center of action of E_{p2} is collocated with the $H_{\vec{v}1}$ anticyclonic circulation center, and the negative center of action of E_{p2} was collocated with the $H_{\vec{v}2}$ cyclonic circulation center. In addition, the real parts of the $H_{\vec{v}1}$ and $H_{\vec{v}2}$ together account for nearly the same amount of variance in F as E_{p2}. Considering how E_{p2} correlates with $H_{\vec{v}1}$ ($r = 0.25$) and $H_{\vec{v}2}$ ($r = 0.41$) and that the associated power spectra show significant variability for 4–15-day periods, this study supports the conclusion that the east-west SLP dipole linked to F variability in prior work represents the aggregation of poleward-propagating ($H_{\vec{v}1}$) and eastward-propagating ($H_{\vec{v}2}$) synoptic-scale cyclones and anticyclones.

$H_{\vec{v}1}$ and $H_{\vec{v}2}$ together account for a modest 16% of F, and wind-based indices could have easily been constructed to account for far more (e.g., one of the correlation vectors in Fig. 5.1 alone has a length of 0.57). The purpose here was not to optimally account for F, but rather to determine the two most important propagating patterns of daily Arctic surface wind variability, and to investigate how they influence F

and illuminate aspects of prior related work based on analyses of storm tracks and standing-wave SLP patterns.

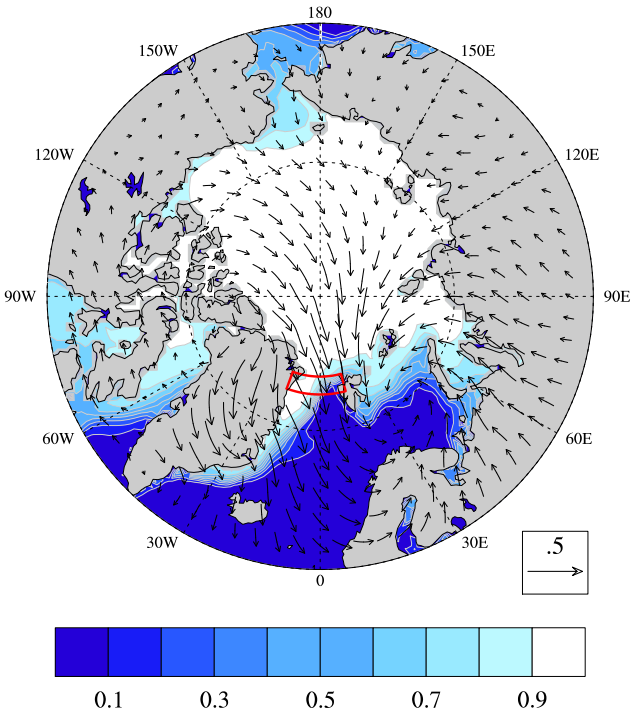

Fig. 5.1. Arrows indicate the vector correlation between F and the surface wind field. Arrow length indicates the magnitude of the correlation, and the direction corresponds to the sign of the correlation. The reference vector in lower right corner corresponds to a correlation of 0.5. The red box indicates the region used to define F. Shading corresponds to sea ice concentration.

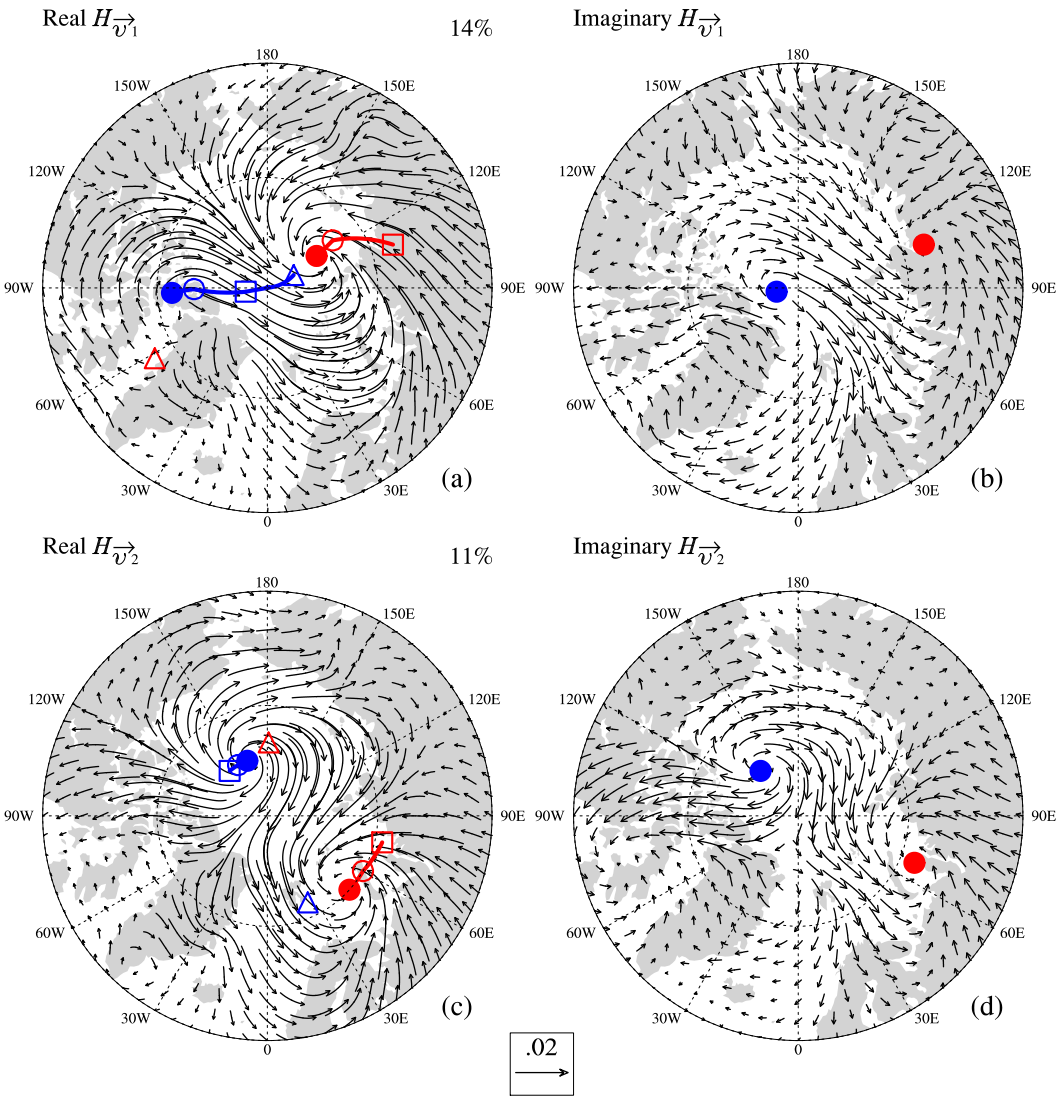

Fig. 5.2. Real and imaginary parts of the leading two HEOFs of surface wind. (a) The real part and (b) the imaginary part of the first phase-shifted HEOF of surface wind ($H_{\vec{v}1}$). (c) The real part and (d) the imaginary part of the second phase-shifted HEOF of surface wind ($H_{\vec{v}2}$). Red symbols mark the centers of cyclonic circulations and blue symbols mark the centers of anticyclonic circulations. Correspondingly colored open symbols show these circulation features advancing forward by $\pi/4$ (open circle), $\pi/2$ (open square), and $3\pi/4$ (open triangle). Curves connect locations where circulation centers follow a continuous path. Percent values in the upper right corners of (a) and (c) indicate the amount of variance in the surface wind field explained by each HEOF.

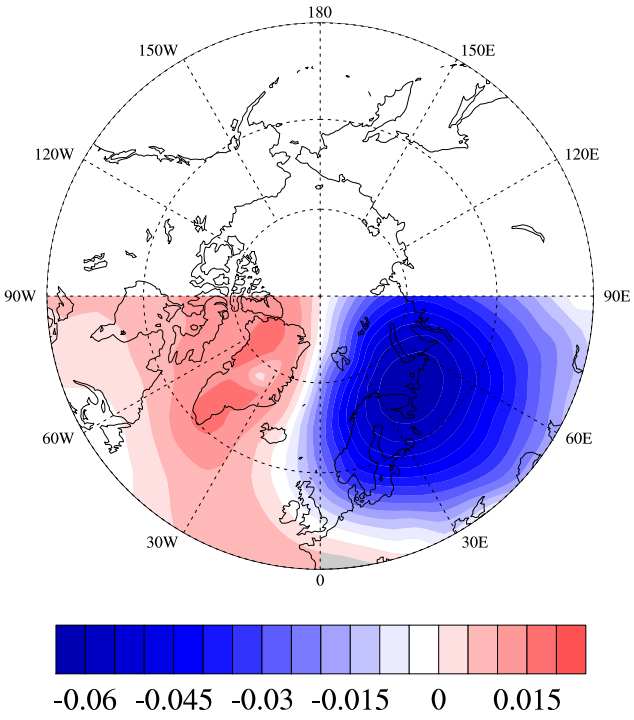

Fig. 5.3. The second EOF of SLP over the domain 90°W–90°E, 45°N–90°N. The contour interval is 0.005.

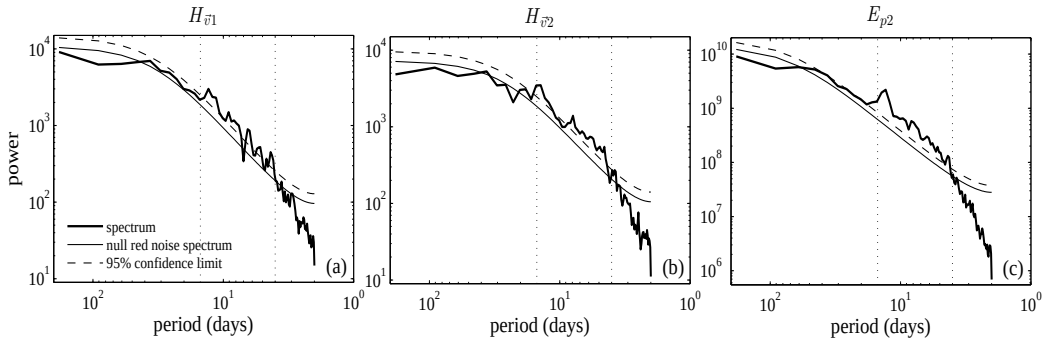

Fig. 5.4. Power spectra (bold black curves) for (a) $H_{\vec{v}1}$, (b) $H_{\vec{v}2}$, and (c) the second empirical orthogonal function of sea level pressure (E_{p2}). Thin solid lines indicate the null red noise spectrum, dashed lines show the 95% confidence limit for the null red noise spectrum, and dotted vertical lines indicate periods of 4 and 15 days.

5.6 References

Brümmer, B., G. Mller, and H. Hoeber, 2003: A Fram Strait cyclone: Properties and impact on ice drift as measured by aircraft and buoys. *J. Geophys. Res.*, **108** (D7), 4217, doi:10.1029/2002JD002638.

Brümmer, B., S. Thiemann, and A. Kirchgäßner, 2000: A cyclone statistics for the Arctic based on European Centre re-analysis data. *Meteorol. Atmos. Phys.*, **75** (3), 233–250, doi:10.1007/s007030070006.

Efron, B., 1979: Bootstrap methods: Another look at the jackknife. *Ann. Stat.*, **7**, 1–26.

Fowler, C., 2003: Polar Pathfinder daily 25 km EASE-grid sea ice motion vectors. National Snow and Ice Data Center, Boulder, CO, http://nsidc.org.

Gilman, D. L., F. J. Fuglister, and J. M. Mitchell, 1963: On the power spectrum of "red noise." *J. Atmos. Sci.*, **20**, 182–184.

Hannachi, A., I. T. Jolliffe, and D. B. Stephenson, 2007: Empirical orthogonal functions and related techniques in atmospheric science: A review. *Int. J. Climatol.*, **27**, doi:10.1002/joc.1499.

Hilmer, M., and T. Jung, 2000: Evidence for a recent change in the link between the North Atlantic Oscillation and Arctic sea ice export. *Geophys. Res. Lett.*, **27** (7), 989–992, doi:10.1029/1999GL010944.

Hurrell, J. W., Y. Kushnir, G. Ottersen, and M. Visbeck, 2003: *The North Atlantic Oscillation: Climate Significance and Environmental Impact*. Amer. Geophys. Union, 27 pp.

Kalnay, E. et al., 1996: The NCEP/NCAR 40-year reanalysis project. *Bull. Amer. Meteor. Soc.*, **77**, 437–470.

Koenigk, T., U. Mikolajewicz, H. Haak, and J. Jungclaus, 2006: Variability of Fram Strait sea ice export: causes, impacts and feedbacks in a coupled climate model. *Climate Dyn.*, **26** (1), 17–34.

Kwok, R., 2009: Outflow of Arctic Ocean sea ice into the Greenland and Barents Seas: 1979–2007. *J. Climate*, **22** (9), 2438–2457, doi:10.1175/2008JCLI2819.1.

Kwok, R., G. F. Cunningham, and S. S. Pang, 2004: Fram Strait sea ice outflow. *J. Geophys. Res.*, **109** (C1), C01 009, doi:10.1029/2003JC001785.

Kwok, R., and D. A. Rothrock, 1999: Variability of Fram Strait ice flux and North Atlantic Oscillation. *J. Geophys. Res*, **104**, 5177–5189, doi:10.1029/1998JC900103.

Nansen, F., 1902: *The Oceanography of the North Polar Basin*. Longmans, Green, and Company, http://books.google.com/books?id=M4ZaHAAACAAJ.

North, G. R., T. L. Bell, R. F. Cahlan, and F. J. Moeng, 1982: Sampling errors in the estimation of empirical orthogonal functions. *Mon. Wea. Rev.*, **110**, 699–706.

Ogi, M., I. G. Rigor, M. G. McPhee, and J. M. Wallace, 2008: Summer retreat of Arctic sea ice: Role of summer winds. *Geophys. Res. Lett.*, **35**, L24 701, doi: 10.1029/2007GL029897.

Rogers, J. C., L. Yang, and L. Li, 2005: The role of Fram Strait winter cyclones on sea ice flux and on Spitsbergen air temperatures. *Geophys. Res. Lett.*, **32** (6), L06 709, doi:10.1029/2004GL022262.

Serreze, M. C., J. E. Box, R. G. Barry, and J. E. Walsh, 1993: Characteristics of Arctic synoptic activity, 1952–1989. *Meteorol. Atmos. Phys.*, **51** (3), 147–164, doi:10.1007/BF01030491.

Sickmöller, M., R. Blender, and K. Fraedrich, 2000: Observed winter cyclone tracks in the Northen Hemisphere in re-analysed ECMWF data. *Q. J. Roy. Meteor. Soc.*, **126**, 591–620.

Skeie, P., 2000: Meridional flow variability over the Nordic Seas in the Arctic Oscillation framework. *Geophys. Res. Lett.*, **27** (16), 2569–2572, doi:10.1029/2000GL011529.

Sorteberg, A., and B. Kvingedal, 2006: Atmospheric forcing of the Barents Sea winter ice extent. *J. Climate*, **19**, 4772–4784.

Strong, C., and J. Liptak, 2012: Propagating atmospheric patterns associated with winter Midwest precipitation. *J. Hydrometeorol.*, **13**, 1371–1382, doi:10.1175/JHM-D-11-0111.1.

Tremblay, L. B., 2001: Can we consider the Arctic Oscillation independently from the Barents Oscillation? *Geophys. Res. Lett.*, **28** (22), 4227–4230, doi:10.1029/2001GL013740.

Tsukernik, M., C. Deser, M. Alexander, and R. Tomas, 2010: Atmospheric forcing of Fram Strait sea ice export: A closer look. *Climate Dyn.*, **35**, 1349–1360.

Vihma, T., P. Tisler, and P. Uotila, 2012: Atmospheric forcing on the drift of Arctic sea ice in 1989–2009. *Geophys. Res. Lett.*, **39** (2), L02 501, doi:10.1029/2011GL050118.

Vinje, T., 2001: Fram Strait ice fluxes and atmospheric circulation: 1950–2000. *J. Climate*, **14** (16), 3508–3517, doi:10.1175/1520-0442(2001)014$⟨$3508:FSIFAA$⟩$2.0.CO;2.

Wang, J., J. Zhang, E. Watanabe, M. Ikeda, K. Mizobata, J. E. Walsh, X. Bai, and B. Wu, 2009: Is the Dipole Anomaly a major driver to record lows in Arctic summer sea ice extent? *Geophys. Res. Lett.*, **36**, L05 706, doi:10.1029/2008GL036706.

Welch, P. D., 1967: The use of Fast Fourier transform for the estimation of power spectra: A method based on time averaging over short, modified periodograms. *IEEE Trans. Audio and Electrocaust.*, **15**, 70–73.

Wu, B., J. Wang, and J. E. Walsh, 2006: Dipole anomaly in the winter Arctic atmosphere and its association with sea ice motion. *J. Climate*, **19** (2), 210–225, doi:10.1175/JCLI3619.1.

Zhang, X., J. E. Walsh, J. Zhang, U. S. Bhatt, and M. Ikeda, 2004: Climatology and interannual variability of Arctic cyclone activity: 1948–2002. *J. Climate*, **17**, 2300–2317, doi:10.1175/1520-0442(2004)017$⟨$2300:CAIVOA$⟩$2.0.CO;2.

Zubov, N. N., 1943: *Arctic Ice*. San Diego, Calif.,U.S. Navy Electronics Laboratory, 506 pp., http://www.biodiversitylibrary.org/bibliography/39101.